Photophysical characterization and optimization of novel polymer based photosensitizer carrier systems for PDT

Dissertation
zur Erlangung des akademischen Grades
doctor rerum naturalium
(Dr. rer. nat.)
im Fach (Physik)
eingereicht an der

Mathematisch-Naturwissenschaftlichen Fakultät I
der Humboldt-Universität zu Berlin
von

M. Sc. Kuan Chen
geb. am 27.10.1979 in Beijing, China

Präsident der Humboldt Universität zu Berlin
Prof. Dr. Christoph Markschies

Dekan der Mathematisch-Naturwissenschaftlichen Fakultät I
Prof. Dr. Lutz-Helmut Schön

Gutachter/innen: 1. Prof. Dr. Beate Röder
2. Prof. Dr. Jürgen Rabe
3. Prof. Dr. Matthias Ballauf
4. Prof. Dr. Karsten Heyne

Tag der mündlichen Prüfung: 22.06.2010

Table of contents

List of symbols and abbreviations

CePC-HSA	Cetuximab modified *m*THPC-HSA nanoparticles
CNPL1, 2, 3	*m*THPC-PLGA nanoparticles with different loading ratios
CoPC-HSA	Covalently binding *m*THPC-HSA nanoparticles
D_2O	Deuterium oxide
f_{ET}	Energy transfer efficiency factor
FWHM	Full width at half maximum
HpD	Hematoporphyrin Derivates
HSA	Human Serum Albumin nanoparticles
HLPP-HSA	High loading ratio *m*THPP-HSA nanoparticles
IC	Internal Conversion
IgGPC-HSA	IgG modified *m*THPC-HSA nanoparticles
ISC	Inter-System Crossing
LLPP-HSA	Low loading ratio *m*THPP-HSA nanoparticles
Mol, M	Molar, Molar / Liter
*m*THPC	5, 10, 15, 20-Tetrakis (3-hydroxyphenyl)-chlorin
*m*THPC-PLGA	*m*THPC loaded PLGA nanoparticles
*m*THPP	5, 10, 15, 20-Tetrakis (3-hydroxyphenyl)-porphyrin
*m*THPP-COOH	5-(4-Carboxyphenyl)-10, 15, 20-tris (3-hydroxyphenyl)-porphyrin
*m*THPP-PLGA	*m*THPP loaded PLGA nanoparticles
NP	Nanoparticle
NPC	*m*THPC-HSA nanoparticles with different cross-linkages
NPL1, 2, 3, 4, 5	*m*THPC-HSA nanoparticles with different loading ratios
OD	Optical Density
OPO / OPA	Optical Parameter Oscillator / Optical Parameter Amplifier
PDT	Photodynamic Therapy
PEG	Polyethylene glycol

Pheo	Pheophorbide a
PHSA40	40% cross-linked Pheo-HSA nanoparticles
PHSA100	100% cross-linked Pheo-HSA nanoparticles
PLGA	Poly (D,L lactide-co-glycolide) nanoparticles
PNPL1, 2, 3	*m*THPP-PLGA nanoparticles with different loading ratios
PS	Photosensitizer
TCSPC	Time-Correlated Single Photon Counting
TPPS	5, 10, 15, 20-Tetraphenyl-21*H*, 23*H*-porphine-*p*, *p'*, *p"*, *p'"*-tetrasulfonic acid, tetrasodium salt hydrate
$^1\Delta_g^+$, $^1O_2$	Singlet oxygen
ε	Extinction coefficient
Φ_Δ	Singlet oxygen quantum yield
Φ_{FL}	Fluorescence quantum yield
τ_Δ	Singlet oxygen lifetime
τ_{Tair}	Triplet lifetime under normal air condition
τ_{TN2}	Triplet lifetime after 40 min N_2 bubbling

0. Introduction

Photodynamic Therapy (PDT) is an effective treatment for a number of malignant and non-malignant tumours [Röder 2000]. PDT treatment is based on the presence of a drug with photosensitizing properties combined with visible or far red light and oxygen. In darkness PDT drugs are no or low toxic. Absorption of light with suitable wavelength by the tumour-localized sensitizer molecules leads to the generation of singlet oxygen, which directly or indirectly destructs tumour tissue. Tumour destruction can be realized both by cell death and by photodestruction of the tumour vasculature resulting in local hypoxia and indirect cell death [Dougherty et al 1998, Henderson et al 1992]. Targeting to tumour vasculature can also starve tumour by cutting oxygen-carrying blood supply. Within a few hours after successful PDT tumour tissue exhibits extensive regions of necrosis and apoptosis. These cell death mechanisms as well as inflammatory and immune responses are all induced by PDT [Brown 2004].

It is necessary to increase the selectivity of photosensitizer to tumour tissue or cells [Jux and Röder 2009]. This selectivity provides enhancement of therapeutic effect meanwhile minimizes the side effects of PDT. Targeting drug carriers under investigation include proteins, peptides, antibodies, liposomes, micelles, and polymers. Among these carriers, nanoparticles are regarded as a potential PDT agent carrier because of their high stability; high carrier capacity; feasibility to carry both hydrophobic and hydrophilic agents [Gelperina 2005]; multiple administration methods (oral or injection). Besides these advantages, nanoparticles can be designed as controllable drug release carriers. Especially, nanoparticles with suitable size accumulate in tumour tissue because of the enhanced permeability and retention (EPR) effect (details see chapter 2). Moreover targeting antibody modified nanoparticles can identify tumour cells.

Due to their relatively small size about 3-5 nm, inorganic nanoparticles such as gold and silica nanoparticles exhibits weak EPR effect. At the same time, they are easily to form aggregates in aqueous solution. Until now no appropriate inorganic nanoparticles for PDT are found [Jux and Röder 2009]. For a long period many achievements in the field of biodegradable nanoparticles and their conjugations with photosensitizers have been published. In the relevant field, several works have been reported. For instance, meso-tetra (hydroxyphenylchlorine) (*m*THPC) were loaded on biodegradable nanoparticles using passive targeting strategy and tested in HT-29 cells [Bourdon 2000].

Among numerous biodegradable nanoparticles, two types of nanoparticles earn widely concern. HSA protein nanoparticles are prepared and studied since they are biodegradable, non-antigenic, and controllable size distribution [Langer 2000]. PLGA nanoparticles have long been studied as controlled release drug carrier because of their biodegradability and biocompatibility [Bozkir 2005].

This PhD work is a part of a scientific network “NanoCancer” project. The eventual objective of this project is to develop a series of novel nanoparticle-basing drug delivery systems, which attain targeting effects to cancer tissue actively or passively. The highlight of innovation of this project is the combination of large drug carrying capacity with enhanced tumour targeting effect.

Based on this idea, the goals of the work are set as:

a. The selective accumulation of photosensitizer in targeting tumour tissues should be increased;

b. The toxicity of photosensitizer-carrier system, especially singlet oxygen generation during drug administration should be minimized;

c. Controllable and rapid drug release from the carrier should be achieved;

d. Photosensitizer’s photo-activity won’t lose after drug release.

In order to achieve these goals, the main tasks consist of:

a. Photophysical characterizations of photosensitizer-nanoparticle carrier systems using absorption, steady-state fluorescence and TCSPC.

b. Singlet oxygen quantum yield of photosensitizer-loaded nanoparticle formulations are quantified via combination of singlet oxygen luminescence detection and laser flash photolysis.

Interactions between photosensitizer molecules and nanoparticles are investigated.

The influence of the antibody surface modification on singlet oxygen generation of photosensitizer-loaded nanoparticles is studied.

The structure of whole PhD thesis is as follow:

Chapter 0 is introduction. Brief history of PDT, basic principles of photosensitization and singlet oxygen as well as photosensitizer are given in Chapter 1. Principles of passive and active tumour targeting strategies are introduced in Chapter 2. The background knowledge of biodegradable nanoparticles is also provided in this chapter. All experiment techniques involved in this thesis can be found in Chapter 3. Chapter 4 contains knowledge of used materials: photosensitizers and nanoparticles. Pheo-HSA nanoparticles as starting carrier system are investigated also in Chapter 4. In chapter 5, the influences of drug loading ratio and preparation process on the efficiency of *m*THPP- and *m*THPC-HSA nanoparticle systems according to efficient release of drug molecules are evaluated. The photoinduced singlet oxygen generation in solution and in cell suspension are studied.

Chapter 6 focuses on the issue of PLGA nanoparticles as biodegradable carrier for PDT. The comparison of HSA and PLGA nanoparticles both in solution and in cell suspension is provided in Chapter 7.

As active tumour targeting strategy, the surface modification with antibodies and PEG shell to nanoparticles is evaluated by intracellular singlet oxygen determination in Chapter 8. Finally conclusions are drawn in the summary Chapter 9.

1. Brief history of Photodynamic Therapy and fundamentals of Photosensitization

1.1 Brief history of Photodynamic Therapy

Although practiced in ancient Egypt, India, and China thousands of years ago, using light and dyes under the presence of oxygen to produce cytotoxicity was pioneered by Oscar Raab, a student of Hermann von Tappeiner. Raab reported that paramecia could be killed by acridine after illumination. Based on Raab's work, von Tappeiner and Jesionek described the first clinical trial of photosensitizer eosin on several skin tumours in the presence of light [von Tappeiner and Jesionek 1903].

Studies on photodynamic therapy (PDT) have become popular again based on two developments. Advancements in laser light sources and optical fibers have provided broad prospects for clinical PDT, not only for skin diseases but also for diseases associated with the visceral cavity. Suitable photosensitizers were discovered due to the contribution of a series of investigations by T. J. Dougherty and his group since 1973. Their efforts have brought PDT from the laboratory into the clinic. Some of the basic principles have also been established to explain the mechanisms of PDT.

Since 1973, numerous clinical PDT treatments have been geared towards lung cancer [Kato 1998], cancer of the gastrointestinal tract [Puolakkainen 1992, Moesta 1995], tumours in the head and neck regions [Bellnier 2003, Prosst 2003, Dilkes 2003], bladder [Jichlinski 2001] and prostate cancer [Nathan 2002]. PDT provides a method with fewer side effects compared with radiotherapy and chemotherapy; therefore, it offers doctors a possible choice for pre-cancerous disorders. For example, aminolaevulinic acid (ALA) PDT treatment for cervical and vulvar intraepithelial neoplasias has been reported [Barnett 2003, Keefe 2002]. In advanced cancer treatment, PDT improves quality of life. For instance, patients suffering from obstructing endobronchial non-small-cell lung cancer have exhibited increased survival duration after PDT treatment [Barber 2002]. Aside from tumour treatment, PDT has also been introduced to treat non-malignant diseases such as choroidal neovascularization [Renno 2001].

1.2 Molecular mechanism of photosensitization

1.2.1 Photosensitization

Photosensitization or photosensitized reaction is defined as a process where a substance absorbs photons and transfers the energy to reactants. This substance is named a photosensitizer.

There are several photosensitization mechanisms. Two major processes are named Type I and Type II [Foote 1991]. Additionally, a broad definition of photosensitization that includes a Type III was also taken into account [Laustriat 1986]. In Type I reaction, the excited triplet state photosensitizer ($^3P^*$) reacts with the substrate molecule (S) and forms radical pairs or radical ions, as shown in Eqs. 1.1 and 1.2.

$$^{3}\mathrm{P}^{*} + \mathrm{S} \longrightarrow \mathrm{P}^{\cdot -} + \mathrm{S}^{\cdot +} \qquad (1.1)$$

$$^{3}\mathrm{P}^{*} + \mathrm{S} \longrightarrow \mathrm{P}^{\cdot +} + \mathrm{S}^{\cdot -}. \qquad (1.2)$$

This resulting radical species of Type I reaction can participate in many different reactions.

The main photosensitization involved in photodynamic therapy is Type II since most photosensitizers in triplet state transfer their energy to oxygen under normal physiological conditions [Dougherty 1998]. With oxygen participation, excited photosensitizer molecules transfer energy to molecular oxygen and cause singlet oxygen generation. Type II can be written as Eq. 1.3:

$$^{3}\mathrm{P}^{*} + \mathrm{O}_2 \longrightarrow \mathrm{P}^{\cdot -} + {}^{1}\Delta_{g}. \qquad (1.3)$$

The entire photochemical process of Type II photosensitization is shown in Fig. 1.1.

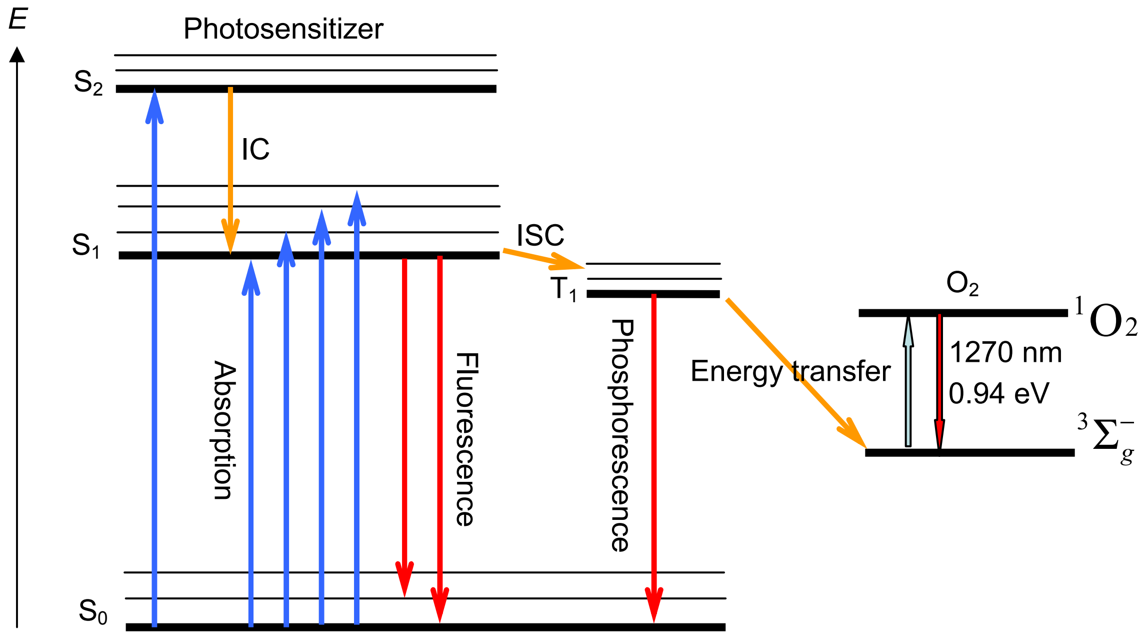

Fig. 1.1. Jablonski diagram of activation and deactivation processes in Type II reaction. S_0: photosensitizer ground state; S_1, S_2: photosensitizer excitation state; $^3\Sigma_g^-$: ground state of molecular oxygen; $^1O_2$: singlet oxygen. IC: internal conversion; and ISC: intersystem crossing

Photosensitization Type III also produces radicals similar to Type I. However, unlike Type I, Type III occurs in the absence of oxygen. The excited photosensitizer molecules in Type III directly interact with the substrate molecules. Radicals are produced via electron transfer from excited state photosensitizer molecules to substrate molecules, especially in the photoreaction center [Laustriat 1986].

1.2.2 Deactivation of singlet oxygen via radiative way

Singlet oxygen deactivation via radiative way includes singlet oxygen phosphorescence, chemiluminescence, and luminescence from the second excited vibrational level of the first excited singlet state. Here, singlet oxygen phosphorescence at 1270 nm is discussed.

The measurement of singlet oxygen phosphorescence at 1270 nm is an efficient method for detecting singlet oxygen. However, since the spin restriction forbids transition from singlet oxygen to ground state molecular oxygen, the intensity of singlet oxygen phosphorescence is usually extremely weak.

Singlet oxygen lifetime depends highly on solvents, ranging from 3.1–4.4 µs [Egorov 1989, Rodgers 1982] in water to approximately 1200 µs in C_2Cl_4 [Salokhiddinov 1981]. The value of singlet oxygen lifetime is influenced by the infrared absorption of CH, CC, and OH groups near 1270 nm, where $^1O_2$ transfers its electronic excitation energy to the vibrational energy level of solvent molecules. Aside from oxygen-solvent energy transfer, the oxidation-reduction reactions in the solutions also influence singlet oxygen lifetime. For example, compared with singlet oxygen lifetime of 3.1–4.4 µs in water, the singlet oxygen lifetime in D_2O induced by solvent isotope effect is approximately 60 µs. In theory, understanding the energy transfer process between singlet oxygen and solvent molecules is helpful to determine singlet oxygen quantum yield. On the practical side, it should be noted that photosensitizer molecules may be destroyed by extensive photobleaching in solvents where long singlet oxygen lifetime occurs [Ogilby 1983].

1.2.3 Singlet oxygen quantum yield

The value of singlet oxygen quantum yield (Φ_Δ) is essential to evaluate potential photosensitizer molecules. Singlet oxygen quantum yield is defined as the ratio of photosensitizer molecules involved in singlet oxygen generation to total photosensitizer molecules in all triplet deactivation processes.

The singlet oxygen quantum yield can be calculated using the equation given by [Bensasson et al. 1993]:

$$\Phi_\Delta = \Phi_T S_Q S_\Delta = \Phi_T \frac{k_{O_2}[O_2]}{k_p + k_{else} + k_{O_2}[O_2]} S_\Delta \,, \qquad (1.4)$$

where Φ_T is the triplet quantum yield; and S_Q represents all deactivation processes, where oxygen is involved; S_Δ is the percentage of S_Q, which results in singlet oxygen generation; k_{O2} is the total rate constant; k_p is the phosphorescence rate constant; and k_{else} is the rate constant of all non-radiative deactivation processes.

Equation (1.4) can be also written as [Oelckers et al. 1997]

$$\Phi_\Delta = \Phi_T \frac{\tau_{TN_2} - \tau_{Tair}}{\tau_{TN_2}} S_\Delta, \qquad (1.5)$$

where nearly every interaction of a tetrapyrrole molecule in the triplet state with oxygen results in singlet oxygen generation [Bensasson 1993]. Thus, S_Δ is nearly equal or equal to 1.

For the treatment of time-resolved singlet oxygen measurement data, Eq. (1.4) can be also written in terms of lifetimes.

$$\Phi_\Delta = A_0 \cdot \frac{1/\tau_{Tair} - 1/\tau_\Delta}{1/\tau_{Tair}}, \qquad (1.6)$$

where A_0 is the amplitude of steady-state singlet oxygen luminescence,

$$A_0 = \frac{n_T(0) \cdot k_{O_2}}{k_{O_2} + k_p - k_{else}}, \qquad (1.7)$$

τ_Δ is the singlet oxygen lifetime, and τ_{Tair} is the triplet state lifetime of the photosensitizer in oxygen-rich solution. The population of all photosensitizer molecules in triplet state is represented by $n_T(0)$.

1.2.4 Singlet oxygen detection in cells

Detection of singlet oxygen generation in living cells is the key to illustrate PDT molecular mechanisms on a cellular level, and will be helpful to novel photosensitizer-carrier system design. Singlet oxygen generation in cells can be indirectly detected, for instance, using laser flash photolysis [Paul 2003], or singlet oxygen quenchers such as beta-carotene [Trekli 2003], uric acid [Cavalcante 2009], or dichlorofluorescein diacetate [Tian, 2008].

Indirect singlet oxygen detection has an essential shortcoming in that it cannot distinguish the singlet oxygen intracellular localization because of the homogeneous singlet oxygen quencher distribution. Therefore, indirect singlet oxygen detection cannot offer detailed information regarding the interaction between singlet oxygen and cellular constituents.

Singlet oxygen luminescence can be detected directly both with steady-state and time-resolved methods. The steady-state method can provide an accurate determination of the singlet oxygen quantum yield. However, it needs a high photosensitizer dose and long measurement period, which lead to photosensitizer photobleaching or cell death. These disadvantages prevent the steady-state method from being used in intracellular measurement.

Although the time-resolved method requires a highly sensitive and rapid-response near-infrared photomultiplier and an elaborate design for signal collection and data processing equipment, it provides kinetic information of singlet oxygen generation and consumption. Furthermore, the singlet oxygen lifetime indicates its intracellular localization since this lifetime is decided by the distribution of singlet oxygen in micro heterogeneous environment.

The most difficult problem of intracellular singlet oxygen luminescence detection is the short lifetime in H_2O [Egorov 1989]. In previous studies, singlet oxygen luminescence was observed in D_2O cell suspension [Gorman 1992, Baker 1992, Bilski 1998]. D_2O cell suspension has two shortcomings: cells behave abnormally in physiological measurements in D_2O and, due to the solvent isotope effect, singlet lifetime in D_2O/H_2O cell suspension is difficult to estimate and unrepeatable [Skovsen 2005]. More recently, the detection of singlet oxygen generated inside cells has been reported. In this case, the singlet oxygen lifetime is less than 0.5 μs due to effective quenching by proteins [Baier 2005, Snyder 2006].

If the photosensitizer is distributed in a microenvironment consisting of phospholipids, the singlet oxygen lifetime will be longer since the quenching rate constant of phospholipids is less than that of proteins [Baker 1992, Ehrenberg 1998]. However, singlet oxygen luminescence generating from phospholipids is too weak to be obtained. Due to the development of new detectors in the last few decades, it has become possible to observe tiny singlet oxygen luminescence generated from erythrocyte ghost membranes [Oelckers 1997]. Improved efforts have been reported in the last few years. For example, Baier et al. successfully obtained singlet oxygen luminescence from HT-29 cells [Baier 2005]. Singlet oxygen luminescence generated from subcellular structures has also been observed [Jiménez-Banzo, 2008; Hatz, 2007]. However, the accurate determination of singlet oxygen lifetime is still hindered by the small amount of singlet oxygen luminescence photons gathered from cells. Recently, Schlothauer et al. obtained accurate singlet oxygen lifetime data generated by pheophorbide a (Pheo) in Jurkat cells under low-dose irradiation using a highly sensitive detector built into a well-designed high signal-to-noise ratio setup [Schlothauer 2008].

Moreover, unlike other studies, this study handles singlet oxygen luminescence results combined with laser flash photolysis results. The benefit of combining laser flash photolysis and luminescence detection in the photobiophysik (PBP) group is that only the combined use of these two methods allows an explicit determination of singlet oxygen lifetime in cells. Singlet oxygen is generated via energy transfer from triplet state photosensitizer to molecular oxygen. This process must compete with all other triplet state photosensitizer deactivation processes. For this reason, the curve of time-resolved singlet oxygen luminescence is determined by singlet oxygen decay and triplet decay together. Apart from other factors, singlet oxygen decay depends on oxygen and singlet oxygen quencher concentration. In contrast, the triplet lifetime usually maintains a nearly stable state. Thus, results will be more reliable when singlet oxygen data are analyzed combined with independent triplet lifetime measurement via laser flash photolysis [Hackbarth 2010].

The temporal shape of singlet oxygen luminescence in a homogeneous environment can be described using Eq. 1.8 [Oelckers 1999]. The obtained singlet oxygen luminescence decay curves are fitted with the two-exponential model function (Eq. 1.8).

$$I(t) = A \cdot \left[\exp\left(\frac{-t}{\tau_\Delta}\right) - \exp\left(\frac{-t}{\tau_{air}}\right) \right] \cdot \frac{\tau_\Delta}{\tau_\Delta - \tau_{air}}. \qquad (1.8)$$

The shape of singlet oxygen luminescence is determined by two competitive lifetimes: the triplet lifetime of photosensitizer, τ_T, and the singlet oxygen lifetime, τ_Δ. The rising of singlet oxygen luminescence is determined by the faster lifetime. The slower lifetime determines the signal decay.

The photosensitizer triplet lifetime in solution is usually shorter than singlet oxygen lifetime. Therefore, the rising signal presents triplet lifetime, τ_T. The decay signal is caused by singlet oxygen lifetime, τ_Δ.

In contrast to singlet oxygen in solution, intracellular singlet oxygen can be quenched by endogenous chemical quenchers in cells. As a result, the singlet oxygen lifetime is usually shorter than the photosensitizer triplet lifetime. In this case, the rising signal is caused by singlet oxygen decay and the decay of the curve is determined by the triplet lifetime.

In this Ph.D. thesis, further investigations that focus on the performance of singlet oxygen generated by photosensitizer-loaded nanoparticles in Jurkat and HT-29 cells are presented. With the aid of in vitro singlet oxygen results, the intracellular uptake mechanism, time-dependent photosensitizer distribution, nanoparticle decomposition, and photosensitizer release are analyzed (Chapters 4–8).

1.3 Electronic excited states of molecular oxygen

Ground state molecular oxygen, known as O_2, plays an important role in the life cycle of organisms. The lowest occupation molecular orbital of ground state oxygen is $(1\sigma_g)^2(1\sigma_u)^2(2\sigma_g)^2(2\sigma_u)^2(3\sigma_g)^2(1\pi_u)^4(1\pi_g)^2$. Many biochemical reactions need the participation of oxygen. The mechanism of oxygen-involved photochemical processes has been explained as early as the 1960s [Foote 1968]. Molecular oxygen in the ground state is non-reactive. However, some reactive oxygen species, such as singlet oxygen $^1\Delta_g^+$ and $^1\Sigma_g^+$, superoxide radical, hydroxyl radical, and peroxide radicals, are highly chemical active components.

However, the lowest electronically excited state of oxygen, $(2\sigma_g)^2(2\sigma_u)^2(3\sigma_g)^2(1\pi_u)^4(1\pi_g)^4$, has been studied in recent decades [Wilkinson 1993]. This active oxidant or “singlet oxygen” ($^1O_2$) has become the key to understand many types of photochemical reactions.

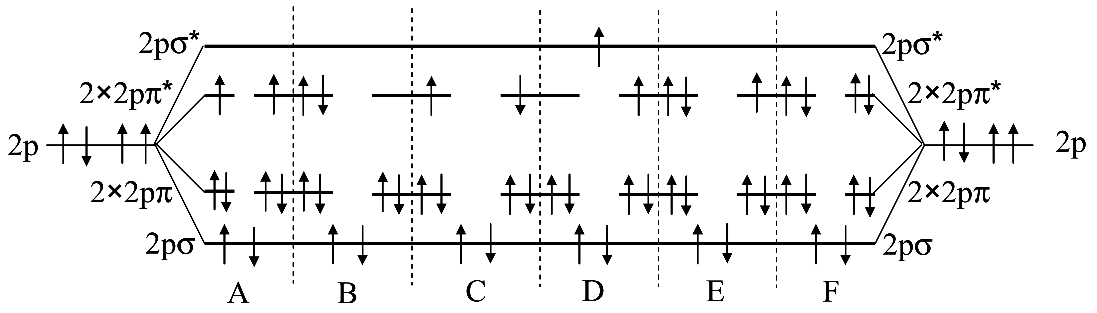

Fig. 1.2. Occupation of molecular orbitals in oxygen:
A. molecular oxygen; B. singlet oxygen$^1\Delta_g^+$; C. singlet oxygen $^1\Sigma_g^+$; D. triplet state molecular oxygen T_1; E. Superoxide radical; and F. peroxide ion [Hackbarth 2000]

Ground state molecular oxygen, or $^3\Sigma_g^-$, has two unpaired p electrons. When excited, it can generate two singlet state species: $^1\Delta_g^+$, with an energy of 94 kJ/mol, and $^1\Sigma_g^+$, with an energy of 157 kJ/mol higher than the ground state. The electronic transitions $^1\Delta_g^+ \leftarrow {}^3\Sigma_g^-$ and $^1\Sigma_g^+ \leftarrow {}^3\Sigma_g^-$ are strictly spin forbidden. Thus, the efficiency of direct excitation with near-infrared light is very low.

Singlet oxygen $^1O_2$ can be generated by different activation pathways, such as the photosensitized generation by energy transfer from triplet state molecules via energy transfer exchanges. In the photosensitization process, the involved singlet oxygen species is $^1O_2$.

1.4 Requirements of an efficient photosensitizer

PDT treatment efficiency depends on numerous factors, such as the choice of light source, light dose optimization, and delivery. However, a highly efficient photosensitizer with specific tumour targeting is always prioritized.

An efficient photosensitizer should achieve the following requirements [Röder 2000]:

1. Photophysical requirements

It can be summarized from Fig. 1.1 that a potential candidate of photosensitizers should have a high intersystem-crossing quantum yield (Φ_{ISC}) and a high triplet quantum yield (Φ_T). The triplet lifetime (τ_T) must also be long enough to induce singlet oxygen generation. The triplet state energy of photosensitizers must be very close to 0.98 eV or 94 kJ/mol, which is the activation energy of $^1O_2$. All of these requirements should be performed by a high singlet oxygen quantum yield (Φ_Δ).

Aside from a high singlet oxygen quantum, a good photosensitizer should have strong absorption in the red or near-infrared region. The long wavelength for excitation is prioritized when choosing excitation sources since the penetration depth in most tissues increases with illumination wavelength. Tissues contain mainly water and protein. The most important protein chromophore in the visible region is the heme group (hemoglobin or Hb) and its oxidized derivative oxyhemoglobin (HbO_2). Both Hb and HbO_2 absorb light between 500 and 600 nm. However, their absorption decreases sharply at wavelengths longer than 630 nm. At this wavelength, light penetration depth is limited by hemoglobin and scattering [Wilson 1989]. At the same region up to 900 nm, water has only weak absorption. Thus, light usage in PDT treatment has maximum penetration in this region, known as the “cure window". The absorption of hemoglobin and water in the visible region is shown in Fig. 1.3.

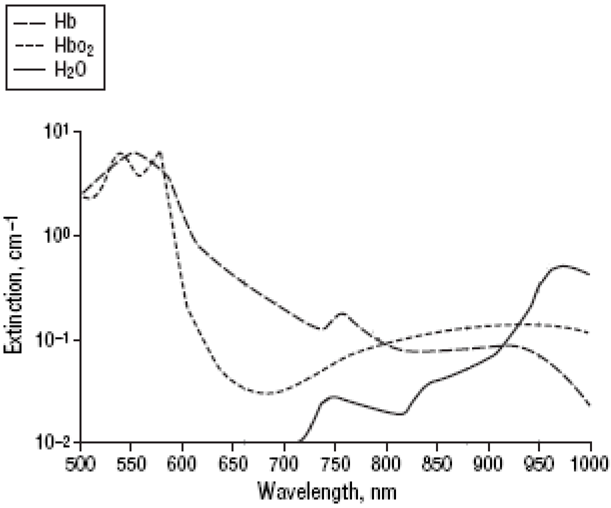

Fig. 1.3 Absorption spectra of hemoglobin (Hb), oxyhemoglobin (HbO_2), and water, from [Wüstenberg 2006]

2. Physicochemical/physiological requirements

First, photosensitizer dark cytotoxicity should be very weak to avoid harm before PDT treatment. Next, the photosensitizer should be preferentially accumulated in the target tumour tissue, which offers the photosensitizer selectivity. Finally, after PDT treatment, the photosensitizer should be rapidly cleaned from the body.

A photosensitizer with these three characteristics minimizes PDT drug dose and drug residue inside the patient's body. Unnecessary damage or side effects to surrounding healthy tissue can therefore be controlled within an acceptable level.

Photosensitizer hydrophobicity is also reported to correlate to PDT efficiency [Pandey 1996]. Hydrophobic photosensitizers are taken up and accumulated preferentially in a subcellular lipid environment. Conversely, these photosensitizers are water insoluble, which might induce a problem for photosensitizer delivery via plasma. One possible resolution to this contradiction is to couple hydrophobic photosensitizers with water-soluble carriers such as serum proteins [Sternberg 1998], sugars [Ono 1992], dendrimers [Röder patent 2001], polymers [Hasan 1989], and nanoparticles [Allemann 1997, Moreno 2003, Yan 2003, Gu 2005, Wang 2004].

For decades, hematoporphyrin derivative (HpD) has been investigated and utilized as the first generation of photosensitizers. However, many problems still prevent it from being successfully used as a PDT treatment worldwide. HpD is derived from mammalian blood [Labbe and Nishida 1957]. The commercial hematoporphyrin, Photofrin®, is a mixture of monomers, dimers, and oligomers. Identifying and evaluating the PDT effective substance of this mixture are very difficult. Maintaining reproducibility when Photofrin® is produced commercially is challenging. The excitation wavelength for HpD is 630 nm, which is not sufficiently long to achieve deeper penetration in tumour tissues thicker than 4 mm. It takes 4–6 weeks for HpD to be cleaned from the body. During this long period, patients must stay in darkness to avoid side effects from unwanted phototoxicity [Prasad 2003].

To overcome the shortcomings of first-generation photosensitizers, second-generation photosensitizers, including modified porphyrins, chlorins, bacteriochlorins, and phorbides, were designed and synthesized as early as the 1980s [Dougherty 1998].

The family of porphyrins is a representative photosensitizer with an 18 π electron conjugated system. The absorption behaviour of porphyrins can be explained by Gouterman's four orbital theory [Gouterman, 1961]. According to this theory, the absorption bands of metal-free porphyrins are caused by transitions among two highest occupied π orbitals, HOMO (a_u) and HOMO-1 (b_{1u}), and two lowest unoccupied π orbitals, LUMO (b_{2g}) and LUMO+1 (b_{3g}). The lower components of the Q bands are $a_u \rightarrow b_{3g}$ and $b_{1u} \rightarrow b_{2g}$ transitions. The upper components of the Q bands are $a_u \rightarrow b_{2g}$ and $b_{1u} \rightarrow b_{3g}$ transitions. The Q band absorption is relatively weak due to pseudoparity-forbidden state from alternancy symmetry [Hashimoto 1999]. The Soret band or B band consists of two transitions caused by the ground state to the second excited 2^1B_{3u} and 2^1B_{2u} states. The extinction coefficient at the Soret bands is strong since these transitions are highly allowed. Each of the two Q bands for free-base porphyrins splits into two vibrational bands. The position of the Soret bands is located in the blue region (c.a. 400 nm) and the Q bands between 500 and 700 nm. Although the absorption in Q band region is usually weaker than that in the Soret band, it is more important since longer excitation wavelength presents a benefit in PDT treatment, allowing for deeper penetration of the tumour tissue.

A general character of second-generation photosensitizers is the red shift of the Q band absorption maximum by extending the macrocycle π-conjugation [Ehrenberg 1990]. Stronger extinction coefficient at Q_y (0, 0) band can be achieved by tetrapyrrole ring double bond reduction. A reduction of a pyrrole double bond on the porphyrin periphery generates chlorin, while an additional reduction of second pyrrole double bond generates bacteriochlorin because of the change in symmetry. Both types of components exist widely in nature and can be synthesized. They all have large Q band absorption at wavelengths λ_{max} =650–670 nm for chlorin, and λ_{max} =730–800 nm for bacteriochlorin [Detty 2004].

In this Ph.D. thesis, the investigated photosensitizers are Pheo and *m*THPP derivatives. Pheo is a decomposition product of chlorophyll a. It has been studied as a photosensitizer both in vitro and in vivo for a long period [Röder 1984, 1986, 1990]. It is a very efficient photosensitizer generating singlet oxygen both in its monomeric form [Röder 1984, 1990] or coupled with DAB-dendrimers [Hackbarth 2005]. Its derivative pyropheophorbide-*a* was proven phototoxic in vitro when conjugated to dendrimers and fullerenes [Paul 2003, Rancan 2005]. Unlike other derivatives of chlorophyll a, the series of pheophorbide derivatives are more attractive because of their in vivo activities. These activities originate from the alkyl ether chain [Pandey

1996]. Pheo has a strong absorption in the red region (668 nm) and causes high phototoxicity. It can also be extracted from leaves and spirulina in great amounts. For these reasons, Pheo is used as the starting compound for investigating the photosensitizer-nanoparticle carrier system (Chapter 4).

5, 10, 15, 20-Tetrakis (3-hydroxyphenyl)-porphyrin (*m*THPP) and its derivatives are developed as second-generation photosensitizers [Berenbaum 1986, Hagan 1988]. One of these derivatives, 5, 10, 15, 20-Tetrakis (3-hydroxyphenyl)-chlorin (*m*THPC), was first recognized in 1946 [Ball 1946]. However, no further investigation was conducted due to synthesis difficulty. Whitlock developed a method using diimide to produce chlorins from porphyrins [Whitlock 1969]. However, the product is a mixture of porphyrin, chlorin, and bacteriochlorin, which presents a disadvantage. For this reason, *m*THPC was not used as a PDT drug for a long time owing to purification difficulty. From the 1980's, Berenbaum, Bonnett, and their co-workers began to investigate *m*THPC PDT activity in vivo [Berenbaum 1989, Bonnett 1986]. As the corresponding dihydroporphyrin of *m*THPP, the potential PDT drug *m*THPC possesses many desired properties, such as strong absorption at 652 nm, non-mutagenic quality, low dark toxicity, and stronger phototoxicity in vivo compared with *m*THPP [Berenbaum 1993]. Commercially produced *m*THPC (Foscan®) has already been approved by the European Medicines Evaluation Agency (EMEA) for the palliative treatment of advanced neck and head squamous cell carcinoma [Copper 2003, Hopper 2004]. For these benefits, *m*THPP derivatives, mainly *m*THPC, are used as PDT agents to load HSA and PLGA (Chapters 5 and 6).

2. Tumour targeting and nanoparticle drug carrier system

Most of current clinical antitumour drugs including photosensitizers are not selectively accumulated in cancer cells. Rapid elimination and widespread distribution of the drug in the patients' body lead to high drug dose and thus unwanted side effects. These side effects include long term skin photosensitization for 4 to 6 weeks [Balchum 1985] and pain during PDT was characteristic for 1st generation photosensitizers.

Selective drug delivery systems for tumour therapy have been studied for a long time. Detailed reviews to active and passive drug delivery systems were summarized by Jux and Röder [Jux and Röder 2009]. In general, two strategies can be utilized to increase the tumour selectivity of photosensitizer-loaded nanoparticles: the passive targeting of nanoparticles is designed according to the distinguishing physical properties between healthy tissues and tumour tissues; the active targeting can be achieved in active way by the attachment of a recognition unit to drug carriers such as e.g. special antibodies [Dressler 1992], peptides [Brokx 2002] and low-density lipoproteins (LDL) [Jori 1993].

2.1 Passive strategies of tumour targeting

Passive targeting strategies rely on the natural distribution pattern such as passive diffusion and phagocytosis processes to attain selective drug accumulation in target tumour tissue [Poste 1983]. The (enhanced permeability and retention) or EPR effect is the passive targeting mechanism that has been studied for a long time. It is to describe size-related drug accumulation in tumour tissue [Matsumura and Maeda 1986]. The EPR effect bases on two facts: for one thing, disorganized angiogenic tumour vasculature with leaky endothelium leads hyperpermeability to circulate macromolecules and nanoparticles; for another, large molecule weight drugs in the interstitium can be retained due to lack of intratumoural lymphatic drainage. These properties of leaky vasculature give a priority to tumour tissues get more nutrients than normal tissues [Konan 2002a]. Therefore they play an essential role in rapid growth of tumour. For this reason, large molecule weight drug with more than 40 kDa leads to significant tumour targeting (10-100 folds) in contrast to small molecule weight drug [Duncan 2005b]. The principle of EPR effect is shown in Fig. 2.1.

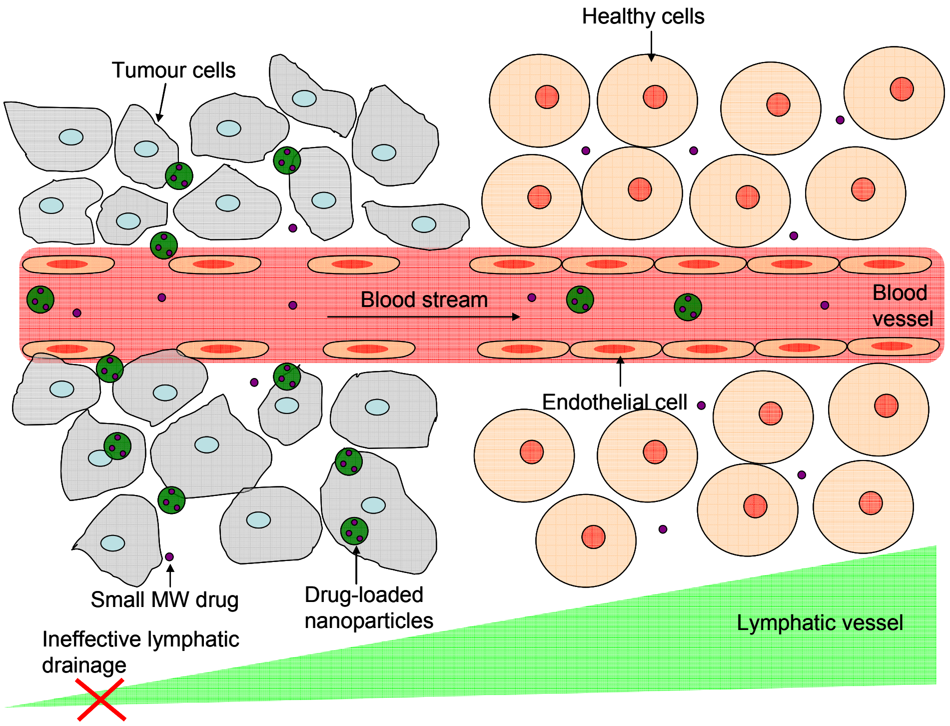

Fig. 2.1. In vivo transport and diffusion of small molecule weight drug and nanoparticle drug carrier system in healthy and tumour tissue and as well as in healthy and tumour vessel. After [Peer 2007]

In recent research, many colloidal carriers were utilized for antitumour drugs to achieve EPR effect, for example, micelles [Van Nostrum 2004], liposomes [Derycke 2004, Chen 2005], oil-based dispersions [Allemann 1997, Biolo 1996] and biodegradable nanoparticles [Konan 2003a, Stevens 2004] as well.

2.2 Active strategies of tumour targeting

Compared to passive strategy, the active strategy is more selective to tumour cells with special gene expressions. For instance, folinic acid-coupled poly ethylene glycol (PEG) nanoparticles have a ten-fold higher appearance in folate over expressed tumour cells than in normal cells [Stella et al., 2000]. It shows an increased uptake by K562 leukemia cells [Bellocq et al, 2003]. Antibody was also widely investigated to enhance intracellular uptake by tumour cells with over expressed receptors.

Trastuzumab for instance, was conjugated to HSA nanoparticles to target HER2 over expressing breast cancer cells [Anhorn 2008].

The benefits of passive tumour targeting strategy include ease-of-manufacturing and low-cost implementation. However, passive strategy has also deficits. It is less selective than active targeting strategy. Moreover, EPR effect is invalid if the size of tumour tissue is too small, which prevents its usage for early stage tumour or metastatic carcinoma.

Active strategy is usually more direct and specific than passive strategy, especially in tumour cells with over-expressed receptors. However, the manufacture process is more difficult and the cost is more expensive. Furthermore, the conjugation efficiency and loading ratio of cell-specific agents are difficult to estimate. In case of nanoparticles, this problem is even more complex.

2.3 Nanoparticle as drug carrier system

Two problems prevent photosensitizer from further development. For one thing, no or low cell-specific selectivity of photosensitizer, which leads to side effects in health tissues; for another, the hydrophobicity of photosensitizer, which hampers intravenous administration. Therefore, suitable delivery drug systems become necessary to overcome the problems [Konan 2002a].

A good drug carrier should achieve requirements as follow:

a. Well protection of the drug from degradation and leaky during pharmaceutical manufacture and clinical administration;

b. Controllable drug release and enhanced drug targeting to tumour or other abnormal tissues;

c. No or low toxic minimum to side effects;

d. Suitable for different kinds of drugs.

Nanoparticles can be defined as a colloidal particle system smaller than 1000 nm [Brigger 2002]. In the field of selective drug delivery, nanoparticles serve several roles: first of all, they can be used as carriers for drugs to achieve EPR effect [Wang 2004]. The suitable particle size for PDT is in the range of 40 to 200 nm [Liu et al.

2002]. Nanoparticles show no or only a weak EPR effect when their size is less than 40 nm. On the contrary, nanoparticles larger than 200 nm have an increasing possibility to be taken up by the mononuclear phagocytic system [Nagayasu et al., 1999].

Besides EPR effect, the benefit of nanoparticles as PDT drug carrier system includes the improved biocompatibility [Konan 2002a] and high drug loading capacity as well as controlled drug release [Pramod 1990, Labib 1991, Kreuter 1983]. Many tetrapyrrole photosensitizers are hydrophobic. This character increases the affinity of photosensitizer for neoplastic tissues. But at the same time, the poor water solubility of hydrophobic photosensitizers in physiological media prevents the drug injection administration [Lin 1991, Pandey et al. 1996, Henderson et al. 1997]. After conjugated to water soluble nanoparticles, the bioavailability of PDT drug in vessel can be improved [Sinha 2006]. For active tumour targeting, cell-specific nanoparticles can be used as carrier for antibodies, DNA and other targeting units to enhance drug selectivity after surface modification.

2.4 Biodegradable nanoparticles

The hydrophobic photosensititizers are appropriate for intracellular accumulation. However, they are difficult to be administrated via injection. Organic biodegradable nanoparticles can promote intravenous administration of hydrophobic photosensitizers as well as their biodistribution [Jux and Röder 2009]

In this PhD thesis, two types of biodegradable nanoparticles: human serum albumin (HSA) and poly (D, L lactide-co-glycolide) nanoparticles (PLGA) were used. Human serum albumin (HSA) is a common protein in blood plasma [Peters 1996, Carter 1994]. HSA can interact with many kinds of organic and inorganic molecules [He 1992, Peters 1985]. As a potential drug carrier, the benefits to use HSA nanoparticle include its biodegradability and non-antigenity [Rubino 1993]. The producing procedure of HSA nanoparticles is relatively easy and the size distribution can be controlled [MacAdam 1997]. Beside these, hydrophobic and hydrophilic drugs can be loaded to HSA nanoparticles via adsorption and covalent attachment [Weber 2000a].

Surface modification is possible since the primary structure of HSA has been defined.

The most convenience property of PLGA as drug delivery agent is its controllable degradation time and drug release kinetics. This can be achieved by adjusting the number and the ratio of lactide / glycolide [Lewis 1990]. The glycolide units are more hydrophilic than the lactide units [Cascone 2002]. So increasing glycolide unit ratio can lead to a quick drug release. On the contrary, higher lactide unit ratio strengthens the combination between hydrophilic drug and PLGA matrix.

PLGA can be produced with quite easy methods, for instance, emulsion-evaporation [Gurny 1981] and emulsion-diffusion [Choi 2002, Niwa 1993]. PLGA nanoparticles can be used widely for drug delivery [Schachter 2002] and gene delivery [Panyam 2003].

Similar to HSA nanoparticles, PLGA nanoparticles are also promising as drug carrier system for their biocompatibility and restorability [Lemoine 1996]. In general, the biodegradation rate of PLGA nanoparticles is proved to be faster than for other biodegradable polymer nanoparticles. However, this behaviour depends on the solvent and surfactant used during PLGA nanoparticles preparation [Jeong 2002]. Related to the size of PLGA nanoparticles, the drug release from the nanoparticles varies from several hours to couple of days [Allemann 1993, Landry 1997, Verracchia 1995].

Due to different preparation procedures, drug can only be loaded on the surface of HSA nanoparticles but incorporated into PLGA matrices. The intracellular nanoparticles decomposition and drug release of these two types of nanoparticles need detailed studies to be compared.

3. Methods

3.1 Ground state absorption (UV-vis spectra)

The ground state absorption spectra were recorded at room temperature using a commercial UV-vis Spectrometer UV-160 (Shimadzu). The measurement range of the absorption spectra is between 200 nm and 1100 nm. The absolute error at Optical Density (OD) =1 is 0.5% with reproducibility of 0.2%.

3.2 Steady-state fluorescence

The fluorescence spectra were taken at room temperature in optical quartz cells with 1 cm optical path length using a Xenon lamp (XBO 150, OSRAM) with a monochromator (LOT-Oriel) for excitation and a polychromator with a cooled CCD matrix for detection (LOT-Oriel, Instaspec IV) [Regehly 2007]. The excitation range of the Xenon lamp is from 350 nm to 800 nm. The determination of the fluorescence quantum yield of sample requires a fluorescence standard reference. The fluorescence quantum yield of sample can be calculated by:

$$\Phi_{sam} = \frac{\varepsilon_{ref} \cdot I_{sam}}{\varepsilon_{sam} \cdot I_{ref}} \cdot \Phi_{ref} \qquad (3.1)$$

Here Φ_{sam} and Φ_{ref} present the fluorescence quantum yields of sample and reference, respectively. ε_{sam} and ε_{ref} refers to the extinctions of the sample and reference at excitation wavelength. I_{sam} and I_{ref} are the integrated fluorescence emission intensities of sample and reference.

3.3 TCSPC

3.3.1 Fluorescence lifetime measurements

Time correlated single photon counting technique (TCSPC) was used to acquire fluorescence decay times. TCSPC technique is based on the detection of single photon of periodical light signal, the detection time measurement and the reconstruction of the measurement signal [O’Connor 1984, Becker 2005]. The TCSPC setup is shown in Fig. 3.1:

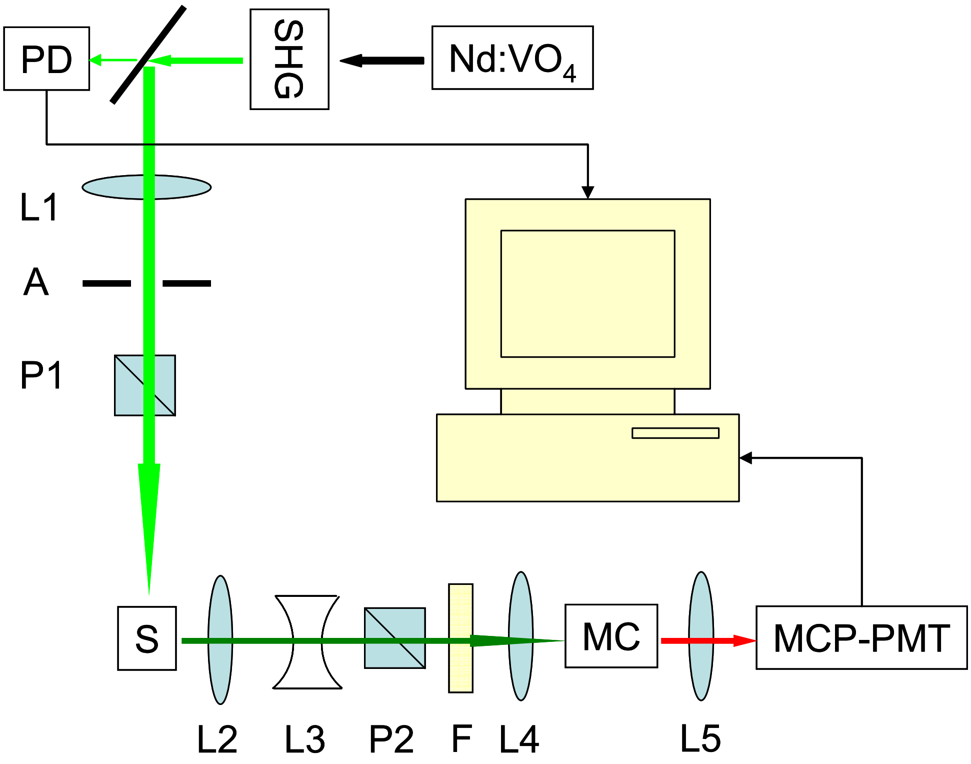

Fig. 3.1. TCSPC setup SHG: second harmonic generator; PD: photodiode; L1, 2, 3, 4, 5: lens; A: aperture; P1, 2: polarizer; S: sample holder; F: filter; MC: monochromator; MCP-PMT: micro-channel plate photomultiplier.

The excitation light emitted from a Nd: VO$_4$ laser (Cougar, Time Bandwidth Products) with a wavelength of 532 nm, pulse width 12 ps and a repetition rate of 60 MHz is separated into two beams: one is recorded by a photodiode and taken as a reference signal; the other beam is focused by lens and sent into sample chamber. The laser intensity is adjusted by tuning of the combination of polarizer P1 and P2.

Optical density (OD) of the samples was 0.2 at the lowest energy absorption band. Fluorescence was detected under a polarization angle of 54.7° (magic angle) with a thermoelectrical cooled microchannel plate (R3809-01, Hamamatsu). Detection wavelength was chosen by a computer controlled monochromator (77200, LOT-Oriel). Electrical signals were processed by a PCI TCSPC controller card (SPC630, Becker & Hickl).

Data were analyzed by a home made program using the least-square method and convoluted by the instrument response function (IRF) including a time shift. Detailed description of the TCSPC set-up is given in [Makarov 2006].

The fluorescence intensity is an exponential function shown as follow:

$$I(t)=\left(\sum_{i=l}^{l-n} a_i \cdot \exp\left(\frac{-t}{\tau_i}\right)\right)\otimes IRF(t-z) \qquad (3.2)$$

Where instrument response function (IRF) is a time-depended function decided by the laser pulse and the response of photomultiplier. IRF can be measured with scattering material at excitation wavelength.

The fitting quality is decided by χ^2 in the least-square method.

$$\chi^2=\sum_{k=l}^{n}\left[\frac{I_m(t_k)-I_f(t_k)}{I_m(t_k)}\right]^2 \qquad (3.3)$$

Where $I_m(t_k)$ is the measured data, $I_f(t_k)$ the fitting data.

3.3.2 Decay associated fluorescence spectra (DAFS)

Decay associated fluorescence spectra (DAFS) are global analysis applied to a multiple set of time-resolved fluorescence spectra [Davenport 1986, Willis 1990]. DAFS is the time-integrated fractional contribution to the total fluorescence spectrum. The calculation of DAFS is given with Equ. 3.4:

$$\mathrm{DAFS}_i(\lambda)=\frac{\alpha_i(\lambda)\tau_i}{\left[\sum_{i=1}^{n}\alpha_i(\lambda)\tau_i\right]\cdot \mathrm{Fluo}(\lambda)} \qquad (3.4)$$

Where $\alpha_i(\lambda)\tau_i$ is the fraction of fluorescence contributed by *i*th term fluorescence lifetime, Fluo(λ) the total steady-state fluorescence spectrum.

3.4 Time-resolved singlet oxygen luminescence

The intensity of singlet oxygen luminescence can be calculated using Eq. 3.5 [Oelckers 1999].

$$I(t)=A\cdot\left[\exp\left(\frac{-t}{\tau_\Delta}\right)-\exp\left(\frac{-t}{\tau_{air}}\right)\right]\cdot\frac{\tau_\Delta}{\tau_\Delta-\tau_{air}} \qquad (3.5)$$

Where *I* is the intensity of singlet oxygen luminescence, *A* is a constant that depends on various instrument parameters and on the solvent. *A* is decided by the light excitation intensity, the photosensitizer absorption at excitation wavelength and the photosensitizer concentration. $A \propto k_{\Delta}$, k_{Δ} is the singlet oxygen luminescence rate constant, which changes with the photosensitizer, and different other parameters like the quencher concentration, the oxygen concentration, the solvent. τ_{Δ} is the singlet oxygen lifetime and τ_{Tair} is triplet state lifetime of the photosensitizer.

The intensity of singlet oxygen luminescence changes in different solvents because the radiative lifetimes of singlet oxygen vary in different solvents [Gorman 1991].

3.4.1 Singlet oxygen luminescence detection in solution

Singlet oxygen luminescence at 1270 nm was detected with a liquid nitrogen-cooled Ge-diode detector Model EO-817P (North Coast, Inc., Santa Rosa, CA). All samples were excited with a Nd: YAG pumped OPO, NT 342/1 (Ekspla, Vilnius, Lithuania). The time-resolved singlet oxygen setup is shown in Fig. 3.2:

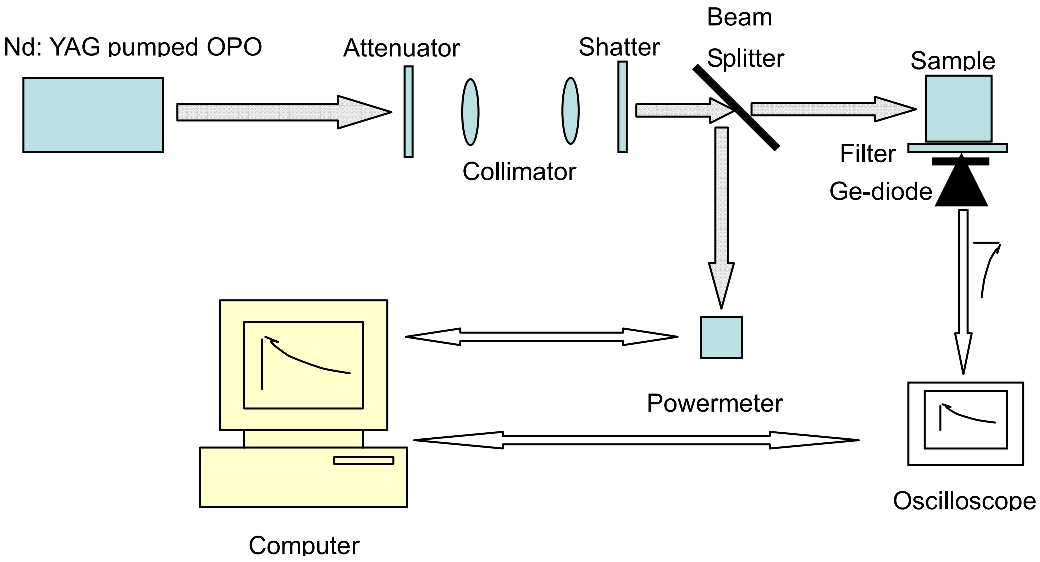

Fig. 3.2. Experiment setup for time-resolved singlet oxygen luminescence measurement.

The excitation light is attenuated by a gray filter and broadened by a collimator. A shatter controlled by computer served as time gate. Then excitation light is split by a beam splitter into two beams. One beam served as excitation to sample. The other is recorded by a powermeter. The detector signal is recorded by an oscilloscope [HP 54542A, Hewlett Packard, USA] and then transmitted to computer [Oelckers 1997].

3.4.2 Singlet oxygen luminescence detection in living cells

The singlet oxygen luminescence of photosensitizers located inside Jurkat cells was observed with the equipment described in [Schlothauer 2008]. This setup is exhibited in Fig. 3.3.

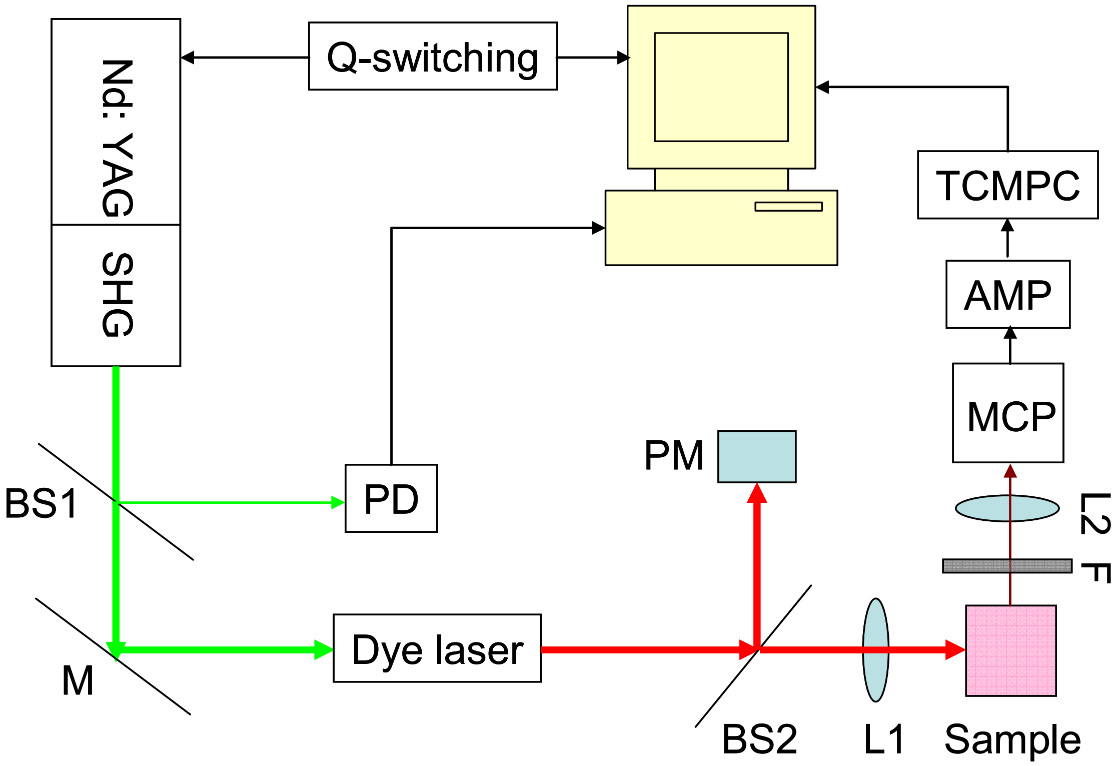

Fig. 3.3. Setup for singlet oxygen luminescence meaurements in cell suspensions, BS1, 2: beam splitter; M: mirror; L1, 2: lens; PD: photodiode; PM; powermeter; F: interference filter; MCP: multi-channel plate; AMP: pre-amplifier; TCMPC: home made TCMPC card.

In this setup, a custom dye laser (DCM, 20 ns FWHM) is pumped by a frequency doubled Q-switching Nd: YAG laser (Serie 600, B.M. Industries). The power of beam is monitored by a powermeter (FieldMaster GS, COHERENT). The fluorescence and scattering light under 1270 nm are blocked by an interference filter (bk-1270-70-B, bk-interferenzoptik, Germany). The luminescence was focused on multi-channel plate photomultiplier (H-10330-45, HAMAMATSU) after gathered and collimated by optical system. The signal is sent to a computer equipped with a custom-made time-correlated multi-photon counting (TCMPC) card.

3.5 Laser flash photolysis

Laser flash photolysis (LFP) is a time-resolved "pump-probe" technique for studying the dynamics of triplet state photosensitizer. The earliest flash photolysis setup was developed by Norris and Porter [Norris 1924, Porter 1957]. The principle of "pump-probe" technique is shown in Fig. 3.4.

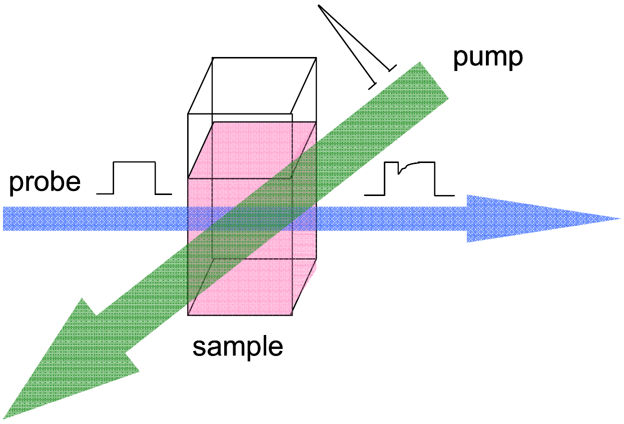

Fig. 3.4. Principle of "pump-probe" method.

In the laser flash photolysis setup, an LED is taken as the probe pulse source. The short intense light pulse generated by a nanosecond pulsed laser Nd: YAG pumped OPO, NT 342/1 (Ekspla, Vilnius, Lithuania) is taken as excitation pulse. This intense light pulse excites ground state photosensitizer into excited singlet state. Then the photosensitizer molecules undergo inter-system crossing (ISC) to excited triplet state. This photo-induced absorption change is recorded by a Si-Diode with integrated fast pre-amplifier (Elektronik Manufaktur Mahlsdorf, Germany). The signal from Si-Diode is digitalized with a fast digital oscilloscope (HP5415). The triplet decay time of photosensitizer can be calculated by analysing the transient absorption curve. The triplet decay time in air-saturated and in oxygen-depleted samples reflects the interaction between photosensitizer and oxygen. The laser flash photolysis setup is shown in Fig. 3.5.

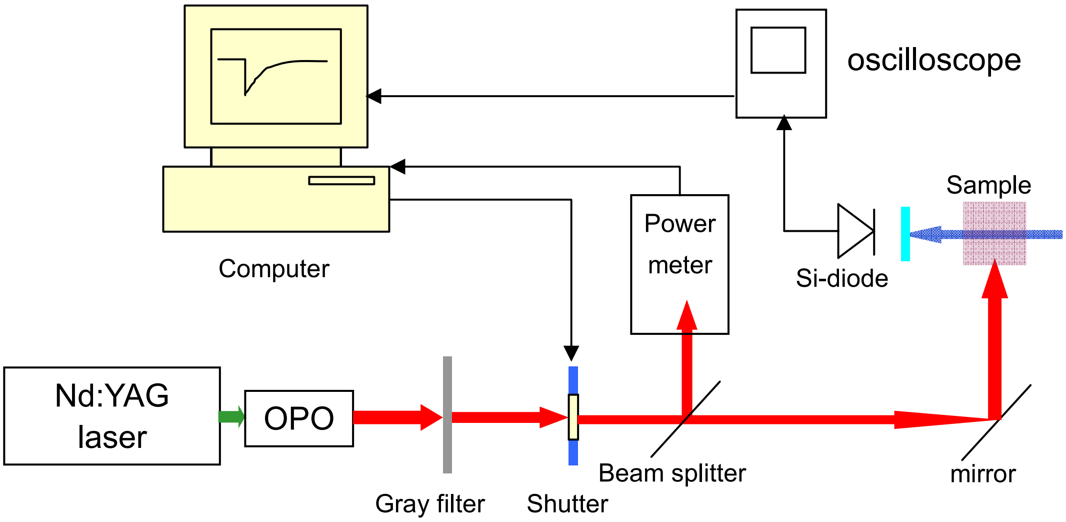

Fig. 3.5. Experimental setup for laser flash photolysis.

According to Lambert-Beer's law, the relation between transmission and absorption can be calculated by Eqs. 3.6 and 3.7:

$$\Delta T = I / I_0 = 10^{-\varepsilon c L} \qquad (3.6)$$

$$\Delta OD = \log 10 \, (1 / \Delta T) = \log 10 \, (I_0 / I) \qquad (3.7)$$

Where T is transmission, I is the intensity received by detector, ε is the molar extinction coefficient, c is the sample concentration, and L is the optical path length. The relation between the change of transmission and optical density is shown in Fig. 3.6.

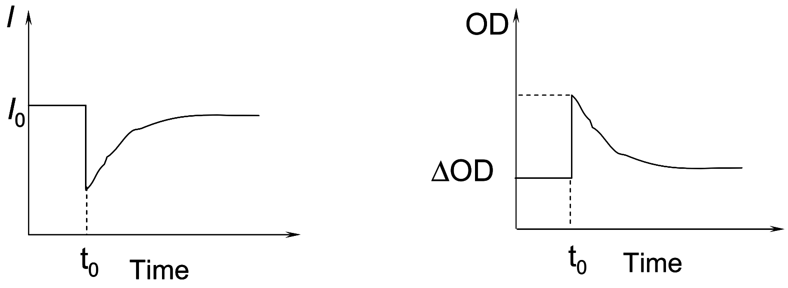

Fig. 3.6. Change of transmission and absorption after laser pulse.

When the change of transmission is not too much, the relation between transmission and absorption is close to linearity. Usually, $\Delta T < 0.2$, therefore the $\Delta OD < 0.08$.

3.6 Cell experiment

The cell samples were prepared by Annegret Preuß and Carmen Ludwig. For in vitro experiments, Jurkat cells (clone E 6-1 human acute T-cell leukaemia) and HT-29 cells (Human colon adenocarcinoma grade II cell line) were cultured in RPMI 1640 medium with L-glutamine (GIBCO) supplemented with 10% fetal calf serum (FCS), 100 U/ml of penicillin and 100 lg/ml of streptomycin without phenol red [Rancan 2005]. Cells were cultivated at 37 ºC in 100% humidity and 5% CO_2 and were seeded in new medium every 2–3 days.

Before intracellular singlet oxygen and triplet lifetime measurement, Jurkat cells (clone E 6-1 human acute T-cell leukaemia) and HT-29 cells were incubated in cell culture medium (RPMI 1640, GIBCO) with photosensitizer, following the procedure described in [Rancan 2005]. After incubation, the cells were harvested and counted (about 2×10^5 cells/ml). The cells were washed with PBS after centrifugation (room temperature, 350 g, 5 min).

4. Materials and basic experiments

4.1 Photosensitizers

Pheo is a dye first extracted from leaves of *Urtica urens* [Willstaetter 1913]. The Pheo used in this thesis was extracted from spirulina *Arthrospira platensis* by Mr. Lutz Jäger.

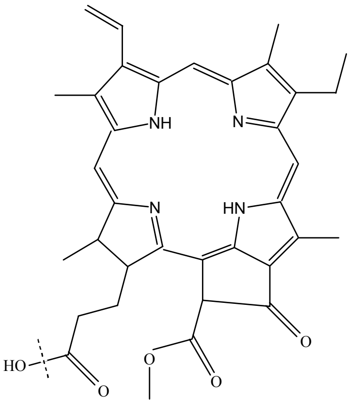

Fig. 4.1. Structural formula of Pheo

The photosensitizing molecules *m*THPP and *m*THPC were obtained from Biolitec AG and Prof. M. Senge (Trinity College, Dublin), respectively.

Name	Mol. Formula	Mol. Weight
Pheophorbide a	C35H36N4O5	592.68 g mol^{-1}
*m*THPP	C44H30N4O4	678.75 g mol^{-1}
*m*THPC	C44H32N4O4	680.77 g mol^{-1}

Table 4.1. Description of photosensitizers pheophorbide a, *m*THPP and *m*THPC

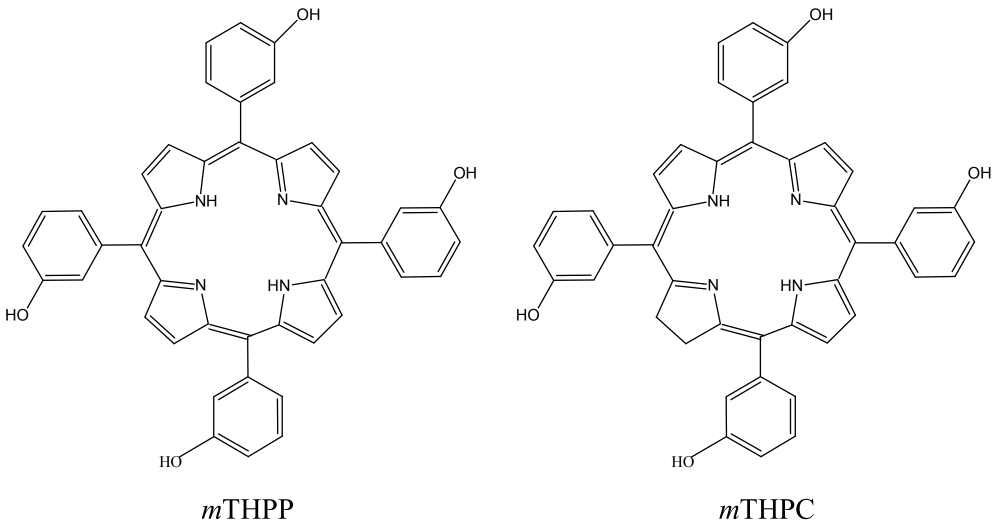

*m*THPP *m*THPC

Fig. 4.2. Structural formula of *m*THPP and *m*THPC

The basic PDT-associated photophysical parameters of Pheo, *m*THPP, and *m*THPC are shown in Table 4.2.

	λ_{max} [nm] (Soret band)	ε [$Mol^{-1}cm^{-1}$]	λ_{max} [nm] $S_{0,0} \rightarrow S_{1,0}$	ε [$Mol^{-1}cm^{-1}$]	Flλ_{max} [nm]	Φ_{fl} (±1%)	Φ_{Δ} (±0.06)
Pheo	406	60600	666	30000	673	0.22	0.52
*m*THPP	412	521600	645	9000	648	0.06	0.63
*m*THPC	417	207000	650	24000	652	0.07	0.65

Table 4.2. PDT-associated photophysical properties of Pheo, *m*THPP, and *m*THPC; Solvent: ethanol; Fl λ_{max}: Fluorescence maximum; Φ_{fl}: Fluorescence quantum yield; Φ_{Δ}: Singlet oxygen quantum yield

As a phorbide, Pheo has a strong Q band absorption at the transition $S_{0,0} \rightarrow S_{1,0}$ with an extinction coefficient of ε=30 000 $Mol^{-1}cm^{-1}$ at 666 nm. More interestingly, the singlet oxygen quantum yield Φ_{Δ} reaches 0.52 [Röder 1986].

The absorption spectrum of *m*THPP has a typical character for porphyrin. The Soret band extinction coefficient is as high as 521600 $Mol^{-1}cm^{-1}$. At the same time, the transition $S_{0,0} \rightarrow S_{1,0}$ reduces to 9000 $Mol^{-1}cm^{-1}$, which becomes a shortcoming for PDT. The fluorescence quantum yield also has great attenuation compared to that of Pheo. The singlet oxygen quantum yield (0.63) is higher than that of Pheo.

The *m*THPC also has a very good ability to generate singlet oxygen. The singlet oxygen quantum yield in ethanol solution is 0.65. As a chlorin, it exhibits strong absorption at Q_y (0, 0) band of $S_{0,0} \rightarrow S_{1,0}$ transition due to its degeneration of one side double bond in the porphyrin ring, which coincides with the result of [Maillard 2007].

4.2 HSA nanoparticles

In preparing human serum albumin (HSA) nanoparticles, water-soluble glutaraldehyde was used to build cross-linkages between different HSA molecules. With glutaraldehyde, cross-linked solid HSA nanoparticles can be formed from unstable HSA colloids. HSA nanoparticles with more cross-linkages are usually more stable during storage [Weber 2000a]. HSA nanoparticles with fewer amounts of cross-linkages may decompose faster and release drugs more rapidly in cells. For this reason, the question of optimal cross-linkage is essential for development of new drug carrier systems. As will be demonstrated in this work, optimized cross-linkage can be determined using photophysical and in vitro singlet oxygen generation evaluation.

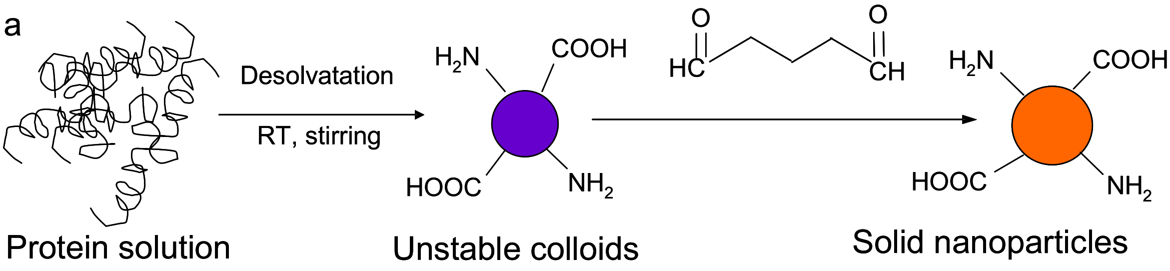

Fig. 4.3. Preparation of HSA nanoparticles, working group conference for BMBF-Project "Development of Cell Type Specific Drug Carrier Systems for Cancer Therapy (NanoCancer)", June 2007

One hundred percent (100%) and forty percent (40%) cross-linked HSA nanoparticles were obtained from Mathias Wacker, Institute of Pharmaceutical Technology, Goethe-Universität, (Frankfurt, Germany). HSA-based nanoparticles prepared in the group of Prof. Klaus Langer [Langer et al. 2000] have a defined particle diameter between 100 and 300 nm with a narrow size distribution [Langer et al. 2000, Weber et al. 2000a]. The fabrication process is shown in Fig. 4.3.

4.3 PLGA nanoparticles

Among numerous biodegradable polymers utilized in surgery and pharmaceutical industry, poly (lactic acid) (PLA) and poly (glycolic acid) (PGA) have been the most widely investigated. In recent decades, their copolymer, biodegradable poly (lactide-co-glycolide) acid (PLGA), has also been considered to be a potential drug delivery agent [Birnbaum 2000] and gene carrier [Csaba 2005].

The safety of both PLGA and its nanoparticles in vitro and in vivo has already been widely evaluated [Panyam 2003, Hirosue, 2001, Perez 2001]. In these studies, PLGA nanoparticles were proven to be taken up by certain kinds of cell lines, including dendritic cells. PLGA nanoparticles can be transported from endo-lysosomal environment to cytoplasmic environment accompanied by drug release [Bivas-Benita 2004].

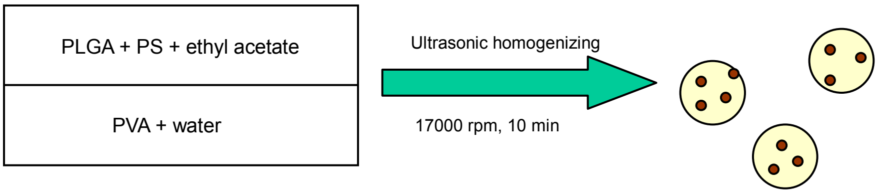

Fig. 4.4. Preparation of photosensitizer-PLGA samples, T. Knobloch, “PLGA-nanoparticle as Carrier for Photosensitizer” working group conference for BMBF-Project “Development of Cell Type Specific Drug Carrier Systems for Cancer Therapy (NanoCancer)”, November 2007

The PLGA nanoparticles studied in Chapter 5 are prepared via emulsion-diffusion-evaporation method [Kwon, 2001]. *m*THPP- and *m*THPC-PLGA or poly (D, L lactide-co-glycolide) were provided by Thomas Knobloch, Institute of Pharmaceutics Technology, (Goethe-Universität, Frankfurt a. M.).

4.4 Pheo-HSA nanoparticles as starting system

The photophysical properties of Pheo-HSA nanoparticle-mixtures were investigated along with their in vitro photoactivity, as well as intracellular singlet oxygen luminescence.

4.4.1 Preparation of Pheo-HSA nanoparticles

A simplified Pheo-HSA nanoparticle preparation procedure is shown in Fig. 4.5.

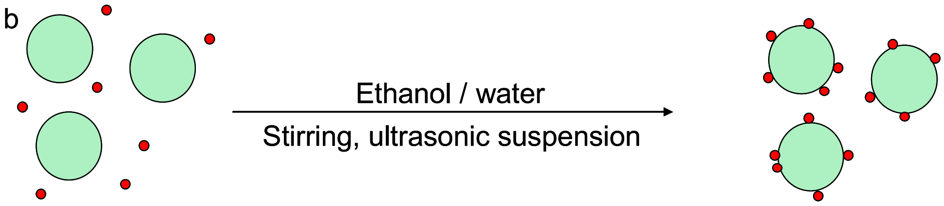

Fig. 4.5. Preparation of photosensitizer-loaded HSA samples

Pheo molecules were loaded on HSA nanoparticles by non-covalent drug adsorption. The molar loading ratio for Pheo and HSA was 4:1. PHSA40 are photoactive nanoparticles with Pheo adsorbed on the surface of 40% cross-linked HSA nanoparticles. PHSA100 are photoactive nanoparticles with Pheo adsorbed on the surface of 100% cross-linked HSA nanoparticles.

Solutions of 100.0 µl Pheo-ethanol (1 mM) were added to 1.6 mg of 100% HSA nanoparticles (18.74 mg/ml in distilled water, or 0.288 mM) and 40% HSA nanoparticles (15.02 mg/ml in distilled water, or 0.231 mM), respectively. After Pheo addition, the mixtures were shaken with a minishaker (IKA-MS1, Milian AG) for 5 min. The mixtures were then adjusted with distilled water to 2.0 ml by slow mixing at room temperature, and nanoparticles were suspended for 10 min by ultrasonication (Elma Hans Schmidbauer GmbH & Co. KG). Pheo-HSA nanoparticles showed an average diameter of 200 nm, as measured by photon correlation spectroscopy using laser light scattering with a Malvern zetasizer 3000HSA (Malvern Instruments Ltd., Malvern, UK) [Langer 2003]. The Pheo-HSA nanoparticles were proven to be stable for several days without changing photophysical properties. The absorption spectra, fluorescence spectra, and fluorescence lifetime of newly prepared Pheo-HSA maintained the same levels after a week's storage.

Unless otherwise stated, for all photophysical experiments Pheo was dissolved in ethanol (spectroscopic grade) and Pheo-HSA nanoparticles were dispersed in distilled water (MilliQ).

4.4.2 Photophysical characterization of Pheo-HSA nanoparticles

First, the absorption spectra were recorded to address the issue of nanoparticle influence on photosensitizer ground state properties. In particular, the problem of possible aggregation or ground state interaction with the nanoparticle had to be investigated because the absorption peaks will attenuate when photosensitizer molecules aggregate. Moreover, the positions of absorption peaks shift if interactions occur between photosensitizer molecules and nanoparticles.

The absorption spectra of Pheo, PHSA40, and PHSA100 are shown in Fig. 4.6, and the data are given in Table 4.3.

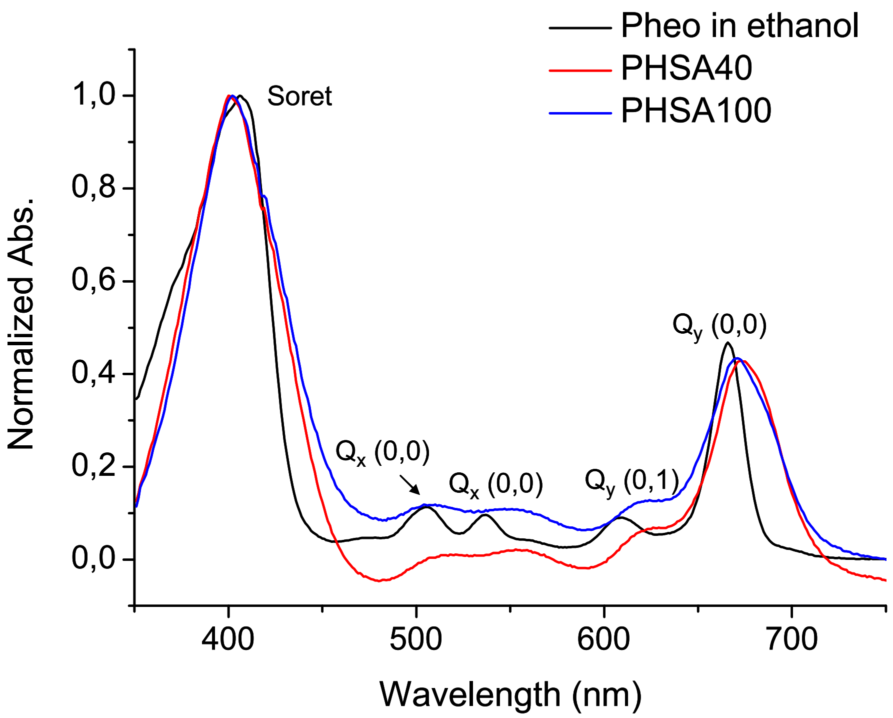

Fig. 4.6. Absorption of Pheo, PHSA40, and PHSA100. Black line: Pheo; Red line: PHSA40; Blue line: PHSA100. Data are normalized at Soret band maximum (the scattering and absorption of HSA nanoparticles were taken into account). The Soret band and four Q bands locate from short wavelength to long wavelength, respectively. The most important Q band for PDT is Q$_y$ (0,0) band formed by $S_{0,0} \rightarrow S_{1,0}$ electron transition.

	λ_{max} [nm] (Soret band)	ε [$Mol^{-1}cm^{-1}$]	λ_{max} [nm] $S_{0,0} \rightarrow S_{1,0}$	ε [$Mol^{-1}cm^{-1}$]	Fl λ_{max} [nm]	Φ_{fl} (±1%)
Pheo	406	60600	666	30000	673	1[a]
PHSA40	400	24000	673	11000	678	0.14[a]
PHSA100	402	26000	671	12100	677	0.14[a]

[a] relative to Pheo

Table 4.3. Photophysical parameters of Pheo, PHSA40, and PHSA100. Pheo was dissolved in ethanol; PHSA40 and PHSA100 were diluted in water. Since the fluorescence quantum yield is determined by comparison with a known reference, the error is mainly caused by the error of the reference, and thus it has the same percentage for all samples. (Fl λ_{max}: Fluorescence maximum; Φ_{fl}: Fluorescence quantum yield.)

As shown in Fig. 4.6 and Table 4.3, for all Pheo-HSA nanoparticles, the extinction coefficient of Pheo at $S_{0,0} \rightarrow S_{1,0}$ transition is reduced to approximately 1/3 compared with that of Pheo. The $S_{0,0} \rightarrow S_{1,0}$ transition is red-shifted to 673 nm for PHSA40 and

671 nm for PHSA100, compared with Pheo, where the $S_{0,\ 0} \rightarrow S_{1,\ 0}$ transition maximum is located at 666 nm. This shift is typical for Pheo if it is attached to large molecules such as dendrimers or nanoparticles [Hackbarth 2005]. At the same time, the full width at half maximum (FWHM) of the $S_{0,0} \rightarrow S_{1,0}$ transition of PHSA40 (39 nm) and PHSA100 (45 nm) is broadened compared with that of Pheo (21 nm). These observations can be treated as a first hint for dye aggregation processes inside or on the surface of nanoparticles.

The differing behaviours of Pheo and Pheo-HSA nanoparticles are more visible in steady-state fluorescence. The radiative transition from excited state Pheo to ground state will be weakened because of competition from all other non-radiative processes in the Pheo-HSA system.

The steady-state fluorescence spectra of Pheo, PHSA40, and PHSA100 are shown in Fig. 4.7.

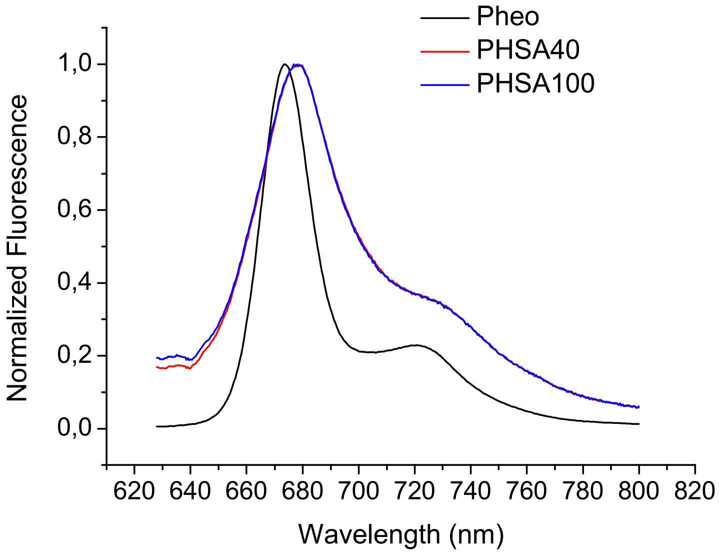

Fig. 4.7. Steady-state fluorescence of Pheo, PHSA40, and PHSA100. Black line: Pheo; Red line: PHSA40; Blue line: PHSA100. Data are normalized at fluorescence peak.

The bathochromic shift of Pheo attached to the nanoparticles was also observable in fluorescence. While Pheo shows its $S_{1,0} \rightarrow S_{0,0}$ transition peak at 673 nm, the fluorescence maximum of the PHSA40 is shifted to 678 nm, while PHSA100 is shifted to 677 nm. The relative fluorescence quantum yields for PHSA40 and

PHSA100 are approximately 14% of that of Pheo. The fluorescence bathochromic shift and the fluorescence intensity reduction of Pheo-HSA nanoparticles are probably caused by interactions between Pheo molecules. The attachment to the protein and the interaction with surrounding water molecules probably result in some strong interaction between closely neighboring Pheo molecules attached to one nanoparticle (Fig. 4.6, Table 4.3).

To prove this theory, the excited Pheo singlet state lifetime was investigated using Time-Correlated Single Photon Counting (TCSPC). The results will reveal the pattern of fluorescence quantum yield attenuation in Pheo-HSA nanoparticles.

Fluorescence lifetimes of Pheo and Pheo-HSA nanoparticles are listed in Table 4.4.

	τ_1 [ns] (±0.2)/A [%]	τ_2 [ns] (±0.1)/A [%]	τ_3 [ns] (±0.05) /A [%]	χ^2
Pheo	5.7/100	-	-	1.02
PHSA40	4.9/57.8	1.6/22.0	0.21/20.3	1.02
PHSA100	5.0/53.1	1.8/23.7	0.29/23.2	0.97

Table 4.4. Fluorescence lifetime of Pheo, PHSA40, and PHSA100 in solution. Pheo was dissolved in ethanol; PHSA40 and PHSA100 were diluted in water. Errors represent the standard deviation of data fitting.

The fluorescence lifetime of Pheo in ethanol is 5.7 ns (Table 4.4). Three different lifetimes were observed for PHSA40 and PHSA100. The longest lifetime component, τ_1, approximately 5 ns, is only slightly shorter than that of Pheo. Such behaviour was also reported in case of other inhomogeneous Pheo molecules environments, such as in Pheo-dendrimer complexes [Hackbarth 2005] or coupled with antibodies [Röder 2000b]. The second decay time, τ_2, can be attributed to Pheo molecules undergoing different interactions that reduce normal fluorescence decay time. The shortest lifetime, τ_3, is probably related to Pheo molecules having strong interactions. Pheo dimers or higher aggregates have little or no contribution to the PDT effect since their singlet oxygen quantum yield is negligible [Röder 2000b].

Pheo is a photosensitizer with high singlet oxygen quantum yield in solution. This is certainly favorable since good PDT therapeutic effect can be achieved even with minimal light and drug dose. However, the high singlet oxygen quantum yield will also be a hazard if patients are unpredictably exposed to light. Therefore, photosensitizer-nanoparticle design should minimize the singlet oxygen quantum yield in solution. Low singlet oxygen quantum yield can be achieved in two ways: via low efficiency of energy transfer from triplet-state PS to molecular oxygen and via singlet oxygen quenching. Singlet oxygen luminescence determination and laser flash photolysis were investigated to study singlet oxygen generation of Pheo-HSA NPs in solution.

The triplet lifetimes of Pheo, as well as PHSA40 and PHSA100 under normal air condition τ_{Tair} and in oxygen-depleted samples τ_{TN2}, singlet oxygen lifetime τ_Δ, and singlet oxygen quantum yield Φ_Δ, are shown in Table 4.5.

	τ_{Tair} (µs)	τ_{TN2} (µs)	f_{ET}	τ_Δ (µs)	Φ_Δ (±10%)
Pheo ^{a}	0.16 ± 0.05	31 ± 3	0.99	15 ± 2	0.52
PHSA40 ^{b}	7.9 ± 0.5	38 ± 4	0.79	11 ± 1	0.07
PHSA100 ^{b}	6.4 ± 0.5	33 ± 3	0.81	11 ± 1	0.08

Table 4.5. Triplet decay times of Pheo in ethanol, PHSA40, and PHSA100 in H_2O air-saturated τ_{Tair} and flushed with nitrogen τ_{TN2}; Singlet oxygen lifetime τ_Δ and quantum yield Φ_Δ; λ_{exc}: 673 nm; λ_{obs}: 488 nm. Pheo was measured in ethanol, Pheo-HSA nanoparticles were measured in D_2O; Rose Bengal in D_2O was taken as standard for Pheo-HSA nanoparticles

The triplet lifetime τ_{Tair} of Pheo in ethanol in air-saturated sample is quite short (0.16 µs). However, the triplet lifetime in oxygen-depleted sample τ_{TN2} is 31 µs, which makes the energy transfer efficiency factor $f_{ET} = (\tau_{TN2} - \tau_{Tair}) / \tau_{TN2}$ nearly equal to 1. Pheo molecules in triplet state are rapidly quenched by molecular oxygen. This leads the large singlet oxygen quantum yield of Pheo (0.52) in ethanol. Triplet decay time τ_{Tair} of PHSA40 and PHSA100 is 7.9 and 6.4 µs, respectively. The calculated f_{ET} of Pheo-HSA NPs decreases to 0.8, which demonstrates low energy transfer efficiency between Pheo and oxygen.

The singlet oxygen quantum yield Φ_Δ of Pheo molecules solved in ethanol is 0.52 [Röder 1986]. For PHSA40 and PHSA100, values of 0.07 and 0.08 were obtained, respectively, which are in the region of the error margin. The singlet oxygen lifetime τ_Δ for PHSA40 and PHSA100 is 11 µs. When compared with the value of singlet oxygen lifetime in D_2O (60–70 µs), singlet oxygen generated by Pheo-HSA nanoparticles is strongly quenched. There are two possible explanations for this phenomenon: efficient interaction between Pheo molecules in the first excited singlet state, and Pheo aggregation on or near the nanoparticle surface.

4.5 Photo-induced singlet oxygen generation in cells

4.5.1 Laser flash photolysis

In contrast to low singlet oxygen quantum yield in solution, the requirement for PS-nanoparticle carrier system in targeting cells should be rapid drug release. The result of laser flash photolysis offers an indicator for intracellular drug release. Here, we use triplet lifetime as a tool to reveal this process in Jurkat cells.

The singlet oxygen generation in Jurkat cells was studied indirectly using laser flash photolysis. The triplet decay time of Pheo was detected under air-saturated conditions and after flushing the sample for 40 min with nitrogen. The measurements were carried out for all photosensitizers after 24 h incubation. The measured triplet decay times (Table 4.6) indicate that Pheo molecules have already been released from HSA nanoparticles after 24 h incubation. This is evidenced in the similar triplet lifetimes of Pheo and Pheo-HSA NPs after 24 h incubation in Jurkat cells. Meanwhile, Pheo release was also proved by Annegret Preuß using confocal laser scanning microscopy (CLSM).

	τ_{Tair} (μs)	τ_{TN2} (μs)	f_{ET}
Pheo	1.8±0.3	35±7	0.95
PHSA40	2.0±0.1	41±24	0.95
PHSA100	2.1±0.1	68 ±34	0.97

Table 4.6. Triplet decay times of Pheo, PHSA40, and PHSA100 in Jurkat cells air-saturated and flushed with nitrogen. Errors represent the standard deviation of three measurements. The error rates of τ_{N2} are caused by low degassing efficiency.

Indirect determination of singlet oxygen generation by laser flash photolysis reveals that Pheo and Pheo-HSA nanoparticles generate similar amounts of singlet oxygen in Jurkat cells after 24 h incubation. This experimental result is in agreement with the studies of phototoxicity done by Preuß [Chen et al. 2009]. The similar amount of singlet oxygen generated by Pheo and Pheo-HSA coincides with their high phototoxicity in Jurkat cells after 24 h incubation. The singlet oxygen generation is also in good agreement with fluorescence lifetime imaging microscopy (FLIM) experiments conducted by Preuß [Chen et al. 2009]. The expected singlet oxygen generation inside cells and high phototoxicity were observed.

Although the singlet oxygen quantum yields of PHSA40 and PHSA100 in solution are relatively low (Table 4.6), before Pheo releasing, the singlet oxygen generation of these samples was very low. This is in good agreement with the observed low phototoxicity of PHSA40 and PHSA100 after 1 h incubation [Chen et al. 2009]. When compared with the triplet lifetime τ_{Tair} in solution (Table 4.5), triplet lifetime of Pheo and Pheo-HSA nanoparticles in cells after 5 h incubation reaches the same level. This indicates that Pheo molecules are discharged from HSA nanoparticles.

4.5.2 Intracellular singlet oxygen luminescence

To date, there is still one question that requires answering: Is Pheo released from HSA nanoparticles still capable of singlet oxygen generation? If yes, is this capability weakened? To reveal the answers, intracellular singlet oxygen luminescence measurement was conducted in two types of cell lines.

The choice of incubation time is based on the intracellular uptake results obtained by Preuß [Chen et al. 2009]. The amount of Pheo inside Jurkat cells after 1 h and 3 h incubation is too small for quantified singlet oxygen luminescence detection. The intracellular uptake by HT-29 cells is even less than that of Jurkat cells.

The choice of cell line is based on the comparable principle. The intracellular uptake and phototoxicity of Pheo and Pheo-HSA nanoparticles have been investigated by Preuß [Chen et al. 2009]. The relationship among intracellular uptake, phototoxicity, and intracellular singlet oxygen luminescence should be compared. However, Jurkat cells are not typical PDT target cells. As adenocarcinoma cells, HT-29 cells are ideal PDT target cells.

	Jurkat cells		
	τ_{Δ} [μs] ± 0.05	τ_{Tair} [μs]	$I_{\Delta}{}^{a}$ ± 30%
Pheo	0.50	3.9 ± 0.2	100%
PHSA40	0.70	3.7 ± 0.4	47%
PHSA100	0.55	3.6 ± 0.5	29%
	HT-29 cells		
Pheo	0.50	5.0 ± 0.5	100%
PHSA40	0.50	3.8 ± 0.4	90%
PHSA100	0.40	3.7 ± 0.4	117%

Table 4.7. Singlet oxygen generation of Pheo and Pheo-HSA nanoparticles in HT-29 cells and Jurkat cells. Incubation time: 5 h; cell number: 5×10^5 cells/ml; illumination time: 20 s; λ_{exc}: 668 nm; laser power: 1.5 mW.

The results of intracellular singlet oxygen luminescence detection show that both Pheo and Pheo-HSA nanoparticles generate singlet oxygen in cells. The singlet oxygen lifetime in Jurkat cells is in the range of 0.40–0.70 µs, which is comparable to previous results [Schlothauer 2008]. The intensity of singlet oxygen luminescence generated by Pheo-HSA nanoparticles in Jurkat cells is less than that of Pheo. On the contrary, the singlet oxygen luminescence intensity of Pheo-HSA nanoparticles in HT-29 cells is nearly the same as that of Pheo. This may indicate a faster Pheo release rate from HSA nanoparticles in HT-29 cells than in Jurkat cells after 5 h incubation. Even in Jurkat cells, however, Pheo discharge from HSA nanoparticles causes high phototoxicity after 24 h incubation, as shown by Annegret Preuß [Chen et al. 2009].

4.6 Conclusions

The fluorescence quantum yield and fluorescence lifetime of PHSA40 and PHSA100 in solution revealed interactions among the photosensitizer and HSA nanoparticles. For the same reason, the singlet oxygen quantum yield of PHSA40 and PHSA100 is significantly lower compared with that of Pheo. Due to the singlet oxygen quenching process caused by HSA nanoparticles, the singlet oxygen lifetime τ_{Δ} of Pheo-HSA nanoparticles is shortened. Due to strong interactions, an extremely low singlet oxygen quantum yield Φ_{Δ} of Pheo-HSA nanoparticles in solution is observed.

Intracellular singlet oxygen luminescence further proves that Pheo-HSA nanoparticles can generate singlet oxygen because of Pheo discharge from HSA nanoparticles both in Jurkat and HT-29 cells after 5 h incubation. HSA nanoparticles are proven to be useful in releasing photosensitizers in cells. Moreover, photosensitizers carried by HSA nanoparticles maintain singlet oxygen generation capability.

Low dark toxicity and remarkable phototoxicity of the released dye molecules make Pheo-HSA nanoparticles potential candidates for PDT treatment. As the next step, other possible photosensitizers, such as *m*THPP and *m*THPC attached to the HSA and PLGA nanoparticles, are investigated in Chapters 5 and 6.

5. HSA-nanoparticles as biodegradable carrier system for PDT

In Chapter 4, the potential of HSA nanoparticles as photosensitizer carriers was demonstrated as they can transmit Pheo into Jurkat and HT-29 cells. After 24 h incubation, the singlet oxygen generation from Pheo-HSA inside both Jurkat and HT-29 cells proves that Pheo molecules can be released from HSA nanoparticles.

Pheo is a natural photosensitizer requiring extraction and purification from leaves or algae. Generally, the quality of mass production is difficult to control in the pharmaceutical industry. The synthetic photosensitizer *m*THPP can be produced in large amounts with constant quality standards. Moreover, modification can be easily achieved by changing functional groups. For instance, chlorin *m*THPC can be obtained by one-side double bond degeneration. Another functional group – hydroxyl group – promotes photosensitizer-nanoparticle conjugation.

In this chapter, the ability of HSA nanoparticles to serve as carriers for *m*THPP and *m*THPC is investigated. The photophysical properties of *m*THPP and *m*THPC-HSA nanoparticles in dependence of loading ratio and degree of HSA cross-linking are also investigated. Furthermore, intracellular singlet oxygen generation by photosensitizer-HSA nanoparticles in Jurkat cells is investigated to evaluate the photosensitizer release from HSA nanoparticles with different degrees of cross-linking. These results will be helpful to further optimize photosensitizer-loaded drug carrier systems since controlled drug release is one of the goals of a potential drug carrier.

5.1 Photophysical properties of *m*THPP-HSA with different loading ratios

In the PS-loaded HSA nanoparticle preparation process, hydrophobic photosensitizer molecules are adsorbed on the surface of HSA nanoparticles. The surface area of HSA nanoparticles restrains maximum drug loading capacity. Within this range, whether or not the photophysical properties of low and high loading ratio *m*THPP-HSA sample are maintained is an interesting question. This is discussed in the following section.

5.1.1 Sample description

The *m*THPP-HSA nanoparticles investigated here were prepared by Matthias Wacker, Institute of Pharmaceutics Technology, Goethe-Universität, Frankfurt, A. M., unless otherwise mentioned. *m*THPP molecules were loaded on the surface of HSA nanoparticles using drug adsorption strategy. Dispersion media for *m*THPP-HSA samples is water.

*m*THPP-HSA nanoparticles were loaded with different loading ratios. The high loading sample (HLPP-HSA) has a loading ratio of *m*THPP/HSA 19.9 µg/mg or 88.35% loading, while the low loading sample (LLPP-HSA) has a loading ratio of 11.1 µg/mg or 49.31% loading.

5.1.2 Absorption and steady-state fluorescence

In Chapter 4, absorption spectra showed that the absorption of photosensitizer-loaded HSA nanoparticles is less than that of the free photosensitizer. However, it remains unclear whether or not the absorption changes once the drug-loading ratio increases. In this section, absorption spectra are taken when the loading ratio changes to study the influence of loading ratio on absorption.

UV-vis absorption spectra of *m*THPP and *m*THPP-HSA were measured. The *m*THPP was dissolved in ethanol, while *m*THPP-HSA nanoparticles were diluted in distilled water. The concentration of *m*THPP used in ethanol is 2 µg/ml or 3 µM. The concentrations of *m*THPP contained in *m*THPP-HSA samples were also adjusted to 3 µM.

The absorption spectra of *m*THPP in ethanol and *m*THPP-HSA nanoparticles in aqueous solution are shown in Fig. 5.1a.

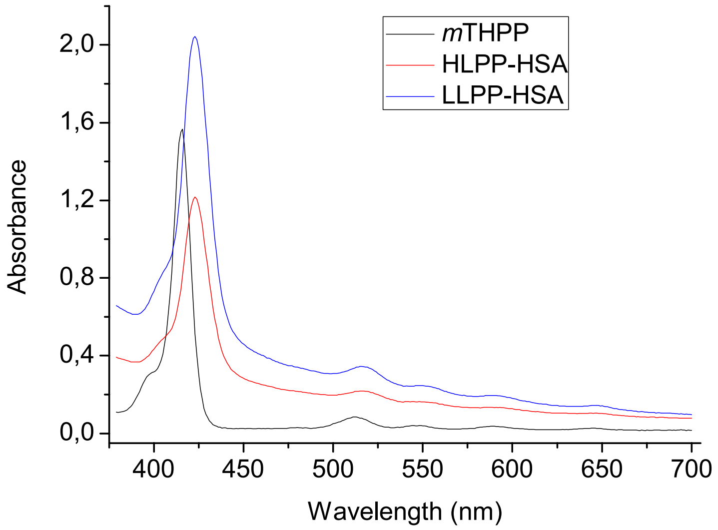

Fig. 5.1a. UV-vis absorption spectra of *m*THPP in ethanol and *m*THPP-HSA in aqueous solution

As can be seen from Fig. 5.1a, the absorption spectrum of free *m*THPP consists of the Soret band transition and four Q band transitions with low absorption in the long wavelength region. The maximum of the *m*THPP Soret band is located at 416 nm. The *m*THPP-HSA Soret band has a bathochromic shift to 423 nm. The centers of four *m*THPP Q bands in ethanol are 512, 546, 589, and 645 nm, respectively. Their counterparts for *m*THPP in *m*THPP-HSA nanoparticles are 517, 552, 591, and 648 nm. These red shifts in the absorption spectrum are caused by the photosensitizer attached to a large unit, such as the nanoparticle surface.

To obtain real extinction coefficient from absorption of *m*THPP in nanoparticles, the absorption data of *m*THPP-HSA were scattering-corrected. Absorptions of *m*THPP-HSA are shown in Fig. 5.1b.

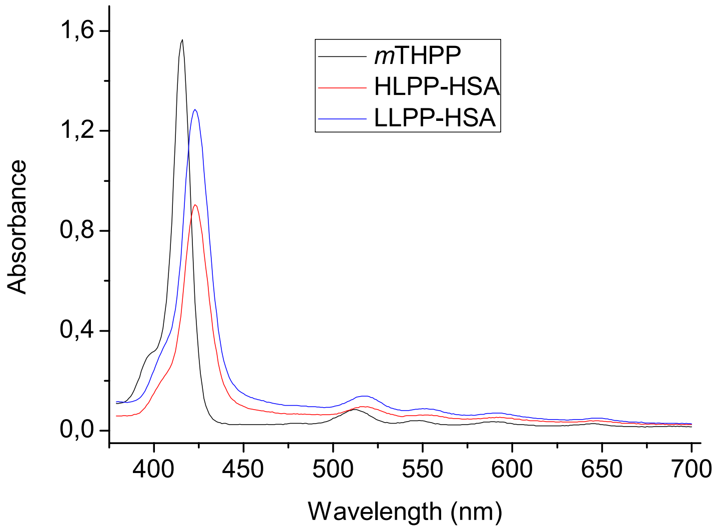

Fig. 5.1b. UV-vis absorption spectra of *m*THPP in ethanol and *m*THPP-HSA in aqueous solution after scattering calibration

Both HLPP-HSA and LLPP-HSA show decreasing absorption in the Soret band region compared to *m*THPP in ethanol. The relative intensity of the HLPP-HSA Soret band is 57% of that of free *m*THPP in ethanol. At the same time, the relative intensity of the LLPP-HSA Soret band is 82% of that of free *m*THPP in ethanol. This absorbance change relates to the photosensitizer-nanoparticle interaction formation due to the increasing concentration of HSA nanoparticles in LLPP-HSA sample. Similar behaviour of absorbance change in the case of photosensitizer-nanoparticle has been reported earlier [Wang 2005].

Absorption spectra show that high loading ratio sample has less absorbance, which also means less *m*THPP molecules participate in fluorescence emission. As proof, the steady state fluorescence was excited at 411 nm. The fluorescence spectra of *m*THPP in ethanol and *m*THPP-HSA samples in aqueous solution are shown in Fig. 5.2.

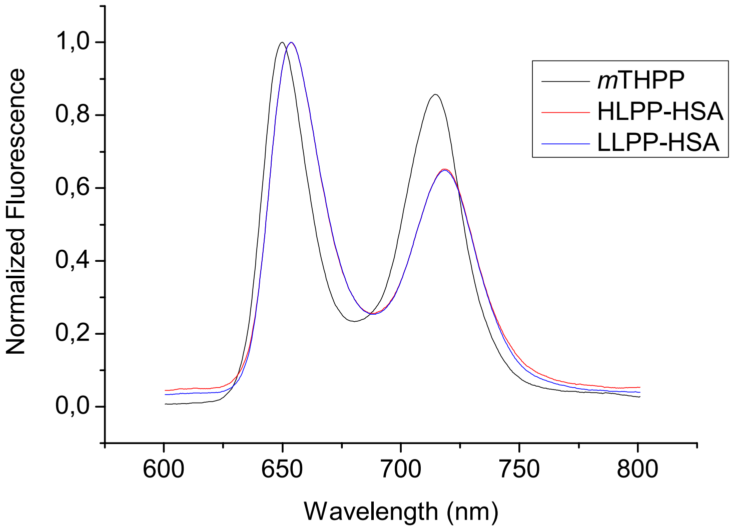

Fig. 5.2. Steady-state fluorescence of *m*THPP in ethanol and *m*THPP-HSA in aqueous solution. Data were normalized

The fluorescence curves of two *m*THPP-HSA nanoparticles with different loading ratios are very similar in shape. The fluorescence peak of $S_{1,0} \rightarrow S_{0,0}$ transitions for *m*THPP-HSA nanoparticles has a bathochromic shift of 4 nm to 654 nm compared to that of *m*THPP in ethanol. The fluorescence peak of $S_{1,0} \rightarrow S_{0,1}$ transition of *m*THPP-HSA nanoparticles also shifts from 714 to 719 nm. This is typical behaviour when photosensitizers are coupled to a large unit, such as a dendrimer [Hackbarth 2005]. The ratio of $S_{1,0} \rightarrow S_{0,1}$ transition to $S_{1,0} \rightarrow S_{0,0}$ transition in *m*THPP-HSA nanoparticles decreases to 0.64 compared with 0.85 of *m*THPP in ethanol. The fluorescence quantum yield of *m*THPP-HSA nanoparticles is also reduced. Compared with *m*THPP in ethanol, HLPP-HSA has 46% and LLPP-HSA has 57% of their fluorescence quantum yield.

5.1.3 Fluorescence kinetic parameters

High loading ratio HLPP-HSA has less fluorescence quantum yield than LLPP-HSA. There are two possible explanations: the population of *m*THPP in excited state reduces, and the fluorescence of HLPP-HSA is strongly quenched. To resolve this, TCSPC is conducted to obtain fluorescence lifetime.

Fluorescence lifetime measurements were carried out using TCSPC with the following parameters: in Chapter 5, for all samples, the excitation wavelength λ_{exc}=532 nm, and fluorescence emission from *m*THPP and *m*THPP-HSA samples are recorded at 650 nm.

Fluorescence lifetimes and their amplitudes of *m*THPP-HSA in aqueous solution are shown in Table 5.1

	τ_1 [ns] ± 0.2 / A [%]	τ_2 [ns] ± 0.1 / A [%]	τ_3 [ns] ± 0.05 / A [%]	τ_4 [ns] ± 0.02 / A [%]	χ^2
HLPP-HSA	8.7 / 19.3	1.3 / 8.4	-	0.019 / 72.3	1.06
LLPP-HSA	9.2 / 63.8	2.1 / 20.0	0.3 / 16.2	-	1.03

Table 5.1. Fluorescence lifetime of *m*THPP in ethanol and *m*THPP-HSA in aqueous solution

The fluorescence spectra of *m*THPP-HSA nanoparticles contain three fluorescence lifetime species for each sample. The shortened fluorescence lifetimes τ_2, τ_3, and τ_4 coincide with the reduced fluorescence quantum yields of *m*THPP-HSA nanoparticles. The steady-state and time-resolved fluorescence data illustrate *m*THPP-*m*THPP interactions in *m*THPP-HSA nanoparticles. However, these interactions change according to *m*THPP loading ratio. The longest fluorescence decay component of *m*THPP-HSA nanoparticles τ_1 is caused by monomer-like *m*THPP molecules similar to *m*THPP (9.6 ns). However, this lifetime (8.7 ns for HLPP-HSA and 9.2 ns for LLPP-HSA) is shorter than that of free *m*THPP, indicating that *m*THPP monomer-like behaviour occurs when photosensitizer attached to large units, such as dendrimers [Hackbarth 2005]. The variables τ_1 and τ_2 can be obtained from the fluorescence decay of both samples. The main fluorescence component in LLPP-HSA is τ_1 (63.8%). However, in HLPP-HSA τ_1 only contributes 19.3% to the total fluorescence signal. Clearly, τ_3 and τ_4 distinguish HLPP-HSA and LLPP-HSA fluorescence decay. The fluorescence decay of LLPP-HSA contains τ_3, which represents *m*THPP-HSA interaction. In contrast, the shortest lifetime, τ_4, exists only in the fluorescence decay of HLPP-HSA caused by strong *m*THPP-*m*THPP interactions. This result coincides with the fluorescence quantum yields of HLPP-HSA and LLPP-HSA.

5.1.4 Singlet oxygen generation

Side effects of PDT such as skin photosensitization are caused by singlet oxygen generation outside tumour tissues or before treatment. The requirement to the third generation photosensitizer is to minimize singlet oxygen quantum yield outside targeting cells and to maximize singlet oxygen quantum yield inside targeting cells. In some cases, a photosensitizer with high singlet oxygen quantum yield generates little or no singlet oxygen when photosensitizers are combined with drug carriers. This phenomenon relies on a number of factors, such as the singlet oxygen quenching by drug carriers and the low efficiency between photosensitizer and oxygen. In the “NanoCancer” project, the manner in which singlet oxygen quantum yield during transportation is minimized depends on photosensitizer-nanoparticle attachment.

Singlet oxygen generation of *m*THPP in ethanol was also measured for comparison. *m*THPP-HSA nanoparticles have weak singlet oxygen luminescence. Obtained singlet oxygen luminescence curves and fitting curves are shown in Fig. 5.3.

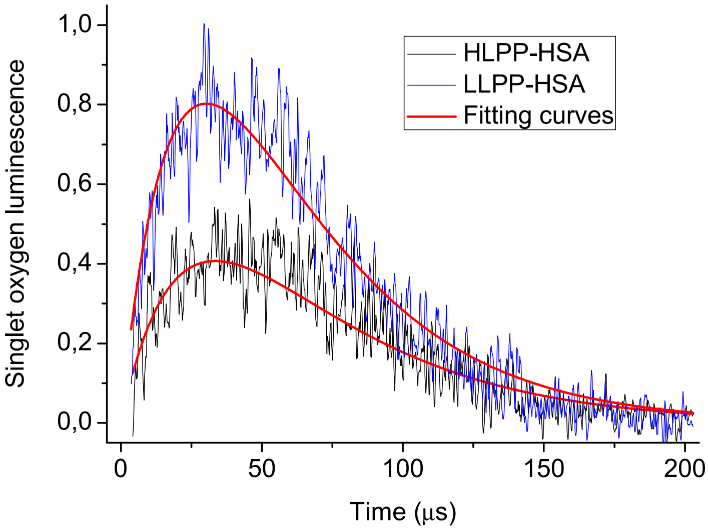

Fig. 5.3. Singlet oxygen luminescence of *m*THPP-HSA nanoparticles in D_2O. λ_{exc}: 514 nm; *m*THPP Conc: 8 μM; Φ_Δ standard for *m*THPP-HSA NPs: Rose Bengal in D_2O (Φ_Δ=0.75)

According to the fitting data from singlet oxygen luminescence signal shown in Fig. 5.3, singlet oxygen luminescence lifetime τ_Δ, triplet state lifetime of photosensitizer with and without oxygen τ_{Tair} and τ_{TN2}, and singlet oxygen quantum yield Φ_Δ of *m*THPP-HSA can be calculated. Results are shown in Table 5.2.

	τ_{Tair} [μs]	τ_{TN2} [μs]	f_{ET}	τ_Δ [μs]	Φ_Δ
*m*THPP	0.31 ± 0.05	47 ± 2	0.99	15.2 ± 0.5	0.63 ± 0.06[a]
HLPP-HSA	29 ± 3	91 ± 3	0.53	42 ± 3	0.04 ± 0.03
LLPP-HSA	33 ± 7	78 ± 2	0.41	29 ± 7	0.07 ± 0.03

Table 5.2. Singlet oxygen generation and triplet decay of *m*THPP in ethanol and *m*THPP-HSA in D_2O. [a]: Φ_Δ standard for *m*THPP in ethanol: Pheo

As can be seen from Fig. 5.3, for the same concentration of *m*THPP loading on HSA nanoparticles, LLPP-HSA has higher singlet oxygen generation quantum yield. It achieves 11% of free *m*THPP in ethanol. However, the singlet oxygen lifetime (29 μs) is much shorter than singlet oxygen lifetime generated by Rose Bengal in D_2O (63–70 μs). This indicates singlet oxygen quenching process in HSA nanoparticles since HSA is a highly effective singlet oxygen quencher [Korinek 2006]. The oxidation reaction constant of singlet oxygen to HSA was determined to be $(5 \pm 3) \times 10^8$ $M^{-1}S^{-1}$ [Davila 1990]. During this process, singlet oxygen can be quenched by both the densely packed *m*THPP molecules and the HSA around it. The different singlet oxygen generation behaviours of HLPP-HSA and LLPP-HSA can be explained by their loading ratios. In the case of LLPP-HSA, the percentage of photosensitizer monomers is higher, which can generate more singlet oxygen than a photosensitizer undergoing interaction. In contrast, the higher loading ratio of HLPP-HSA produces more energy traps or strong interactions among *m*THPP molecules. Only a small amount of *m*THPP molecules, which locate very closely to the surface between HSA nanoparticles and D_2O, can generate singlet oxygen. In this way, HLPP-HSA singlet oxygen quantum yield is less than that of LLPP-HSA. Singlet oxygen generated by *m*THPP in this case locates very closely to the HSA nanoparticle-D_2O interface. Singlet oxygen lifetime τ_Δ of HLPP-HSA (42 μs) is longer than that of LLPP-HSA (29 μs) due to its lower HSA concentration.

Singlet oxygen generation can also be determined via laser flash photolysis. Triplet-triplet photosensitizer absorption was investigated when comparing triplet decay behaviour in air-saturated and nitrogen-saturated solution. For laser flash photolysis measurement, *m*THPP was dissolved in ethanol. *m*THPP-HSA nanoparticles were diluted in D_2O. The samples were excited with an ns-pulse laser pumped optical parameter oscillator at 589 nm, and the change of absorption was monitored at 488 nm. The samples were bubbled with nitrogen for 40 min at room temperature to remove oxygen in solution.

*m*THPP in ethanol exhibited a very short triplet decay time (0.31 µs) in the air-saturated sample, indicating its high singlet oxygen generation efficiency. This also indicates that the difference of solvents should be considered. The *m*THPP is in a hydrophobic environment and the concentration of oxygen in ethanol is different from that in D_2O. Under normal air conditions, *m*THPP-HSA nanoparticles exhibit a long triplet decay time (29 and 33 µs for HLPP-HSA and LLPP-HSA respectively). One possible reason could be that the *m*THPP molecules are closely stacked on the HSA nanoparticles surface, which offers a lower oxygen concentration microenvironment. Another explanation could be the higher viscosity around the nanoparticles, which reduces oxygen diffusion rate [Aveline 1998].

5.2 Photophysical properties of *m*THPC-HSA with different loading ratios

In the last section, the loading ratio issue of *m*THPP-HSA nanoparticles was discussed. The benefits of using *m*THPP as photosensitizer include easy manufacture and relatively inexpensive production costs. It also can be conjugated to nanoparticles covalently. However, the low absorption in the Q_y band region prevents *m*THPP from further clinical PDT usage. In the “NanoCancer” project, *m*THPC was chosen to be the final photosensitizer in following in vivo and clinical investigation. For this reason, more sophisticated photophysical study on *m*THPC-HSA nanoparticles is demonstrated in the following section.

5.2.1 Sample description

*m*THPC molecules were loaded on HSA nanoparticles (7.656 mg / ml) by non-covalent adsorption. After *m*THPC addition (1 mM), the mixtures were shaken with a minishaker (IKA-MS1, Milian AG) for 5 min and suspended for 10 min by ultrasonication (Elma Hans Schmidbauer GmbH & Co. KG).

Samples in Section 5.2 contained different *m*THPC/HSA loading ratios (Table 5.3).

For the preparation of HSA nanoparticles, glutaraldehyde was used as the cross-linking agent. The amount of added glutaraldehyde mainly influences drug release and the stability of HSA nanoparticles during long-term storage [Weber 2000]. A typical amount of glutaraldehyde used for particle stabilization is between 40% and 200% of the amount necessary for stoichiometric cross-linking of the 59 amino groups in the HSA molecule [Carter 1994]. The HSA nanoparticles used here have 100% cross-linking, which means that theoretically, 100% of amino groups in HSA are cross-linked by glutaraldehyde. This loading procedure was carried by the candidate in PBP chemical laboratory. The dispersion media for all *m*THPC-HSA samples is water.

	CL	Lr (µg / mg)
NPL1	100%	4.5
NPL2	100%	8.9
NPL3	100%	17.8
NPL4	100%	44.5
NPL5	100%	89

Table 5.3. Sample description: *m*THPC-HSA nanoparticles with different loading ratios; CL: HSA cross-linking; Lr: Loading ratio *m*THPC / HSA

Unless otherwise mentioned, *m*THPC was dissolved in ethanol for all photophysical investigations described in Sections 5.2 and 5.3. The *m*THPC-HSA nanoparticles were diluted in distilled water. The concentration of *m*THPC used in ethanol was 3 µM, while the concentration of *m*THPC contained in *m*THPC-HSA samples were also adjusted to 3 µM.

5.2.2 Absorption spectra

The most obvious effect in absorption is the dependency of both the strength and spectral position of the Soret band from the loading ratio (Fig. 5.4).

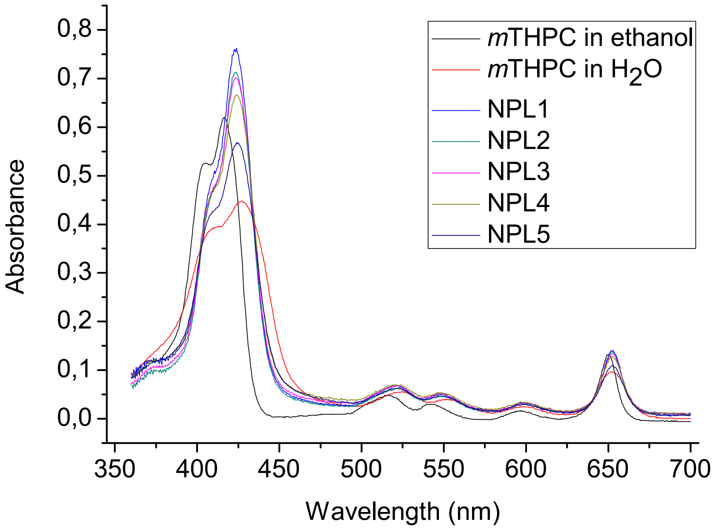

Fig. 5.4a. UV-vis absorption spectra of *m*THPC in ethanol and water, and of *m*THPC-HSA in aqueous solution, *m*THPC Conc.: 3 µM (scattering corrected)

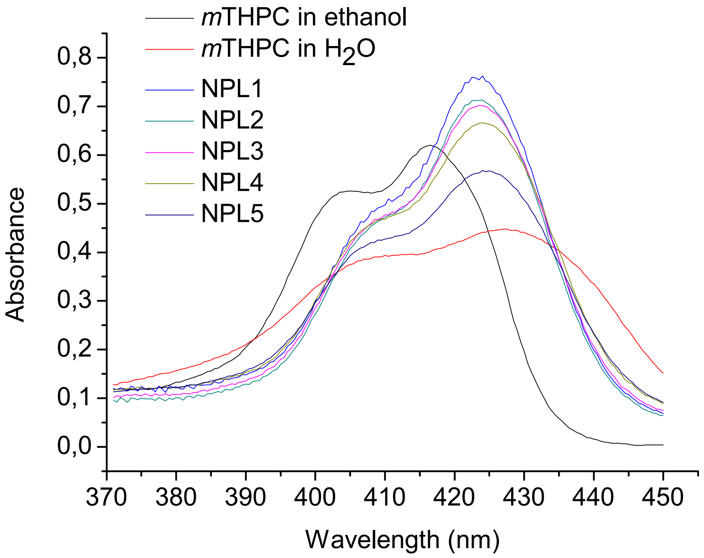

Fig. 5.4b. UV-vis absorption spectra (Soret band region) of *m*THPC in ethanol and aqueous solution, and of *m*THPC-HSA nanoparticles in aqueous solution, (scattering corrected)

	λ_{max} (nm)	ε ($M^{-1}cm^{-1}$)	FWHM (nm)
*m*THPC in ethanol	416.6	2.07×10^5	32.7
NPL1	423.4	2.52×10^5	32.2
NPL2	423.4	2.39×10^5	32.4
NPL3	423.7	2.32×10^5	33.3
NPL4	424.0	2.22×10^5	35.4
NPL5	424.8	1.88×10^5	37.7
*m*THPC in H_2O	427.2	1.49×10^5	54.2

Table 5.4. Soret band maxima and extinction coefficient of *m*THPC and *m*THPC-HSA

The Soret band maximum of *m*THPC in ethanol is at 416.6 nm and exhibits a large bathochromic shift, approximately 10 nm in aqueous solution. The Soret band maximum of *m*THPC in NPL1 is at 423.4 nm and shifts slightly to 424.8 nm for *m*THPC in NPL5.

For *m*THPC, the extinction coefficient at Soret band maximum decreases from 2.07×10^5 $M^{-1}cm^{-1}$ in ethanol to 1.49×10^5 $M^{-1}cm^{-1}$ in water (Table 5.4). Accompanied by reducing extinction, the FWHM of the Soret band broadens to 54.2 nm compared to 32.7 nm of *m*THPC in ethanol.

For the loaded HSA nanoparticles, the extinction of the Soret band maximum continuously decreases from 2.52×10^5 $M^{-1}cm^{-1}$ for NPL1 to 1.88×10^5 $M^{-1}cm^{-1}$ for NPL5 (Fig. 5.4). The FWHM increases about 5.5 nm with increasing loading ratio.

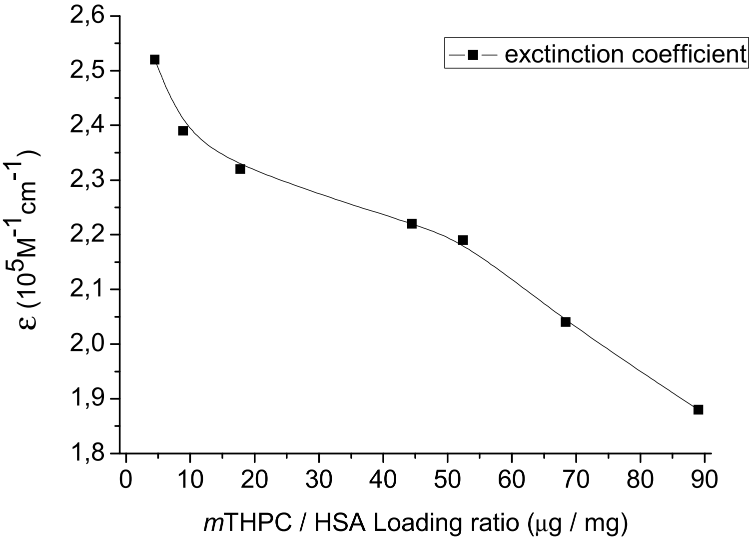

Fig. 5.5. Extinction coefficient in dependence on *m*THPC / HSA loading ratio, *m*THPC concentration: 3 µM

As can be seen from Fig. 5.5, the extinction coefficient of the *m*THPC correlates with the loading ratio. Moreover, the changes of the extinction coefficient are not linear with loading ratio increase. This observation suggests that, aside from the interaction of *m*THPC molecules with the HSA nanoparticles, another type of interaction that occurs mainly at higher loading ratios should exist. Owing to geometric considerations, the interaction of *m*THPC with the HSA nanoparticle should be nearly independent from the loading ratio. In contrast, at high loading ratio, the closer positioning of the individual *m*THPC molecules in each nanoparticle causing additional interactions between the dye molecules is highly probable. Owing to the superposition of these two effects, the extinction coefficient changes are not linearly dependent on the loading ratio. As a result, the intensity of this interaction does not simply depend on the number, but on the distance between neighboring molecules on/in the nanoparticle. At low loading ratio (< 10 µg/mg), more *m*THPC molecules are "lone standing" or exhibit monomer-like behaviour. For these samples, the observed differences from *m*THPC in solution are mainly caused by the interaction between the photosensitizer and HSA nanoparticles.

At loading ratios between 10 and 40 µg/mg, the extinction coefficient is decreasing. This effect is even more pronounced at high loading ratios (> 44.5 µg/mg). For these samples, *m*THPC-HSA interaction plays a minor role because of the influence from neighboring *m*THPC.

Since the interactions are visible in the ground state, it is highly probable that the *m*THPC molecules undergo strong interactions. Such interactions have also been reported for other multichromophoric chlorin systems [Ermilov 2005, Hackbarth 2005].

5.2.3 Steady-state fluorescence spectra

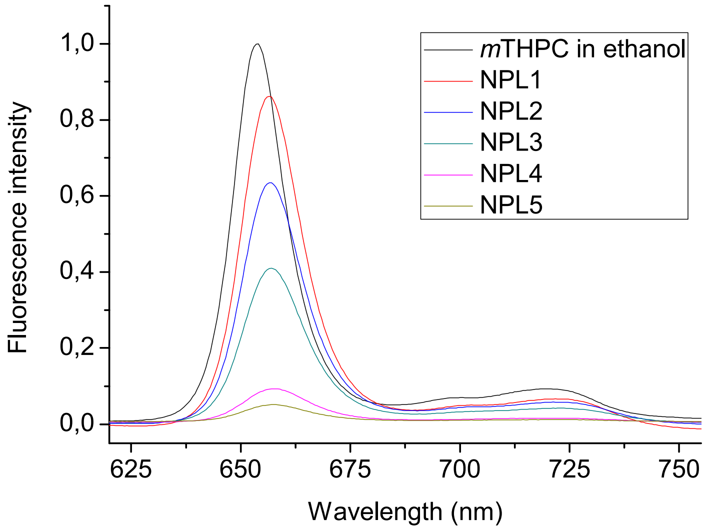

Fig. 5.6. Fluorescence spectra of *m*THPC in ethanol and of *m*THPC-HSA nanoparticles with

different loading ratios (*m*THPC conc.: 3 μM; λ_{exc}: 506 nm)

The fluorescence emission maximum of *m*THPC in ethanol is at 653.8 nm (Fig. 5.6). The fluorescence peak of *m*THPC-HSA nanoparticles in aqueous solution bathochromically shifts slightly. This bathochromic shift increases when drug loading ratio rises, and is accompanied by decreasing fluorescence emission. The fluorescence peak of NPL1 has a 2.5 nm bathochromic shift to 656.3 nm. This sample has 80% of fluorescence quantum yield compared to that of *m*THPC. The fluorescence quantum yield of NPL3 is still 46.2%. However, the quantum yield decreases below 20% for NPL4. Furthermore, the fluorescence maximum of NPL5 shifts approximately 4.9 nm. It has only 8.6% of fluorescence quantum yield compared to that of *m*THPC. The low fluorescence quantum yield and large red shift indicate that *m*THPC-*m*THPC interaction is dominant in high loading ratio samples. The fluorescence data are summarized in Table 5.5.

Sample	Lr [μg / mg]	λ_{max}[nm] of $S_{1,0}\rightarrow S_{0,0}$	λ_{max} [nm] of $S_{1,0}\rightarrow S_{0,1}$	Φ_{Fl} [%] [a]
NPL1	4.5	656.3	722.3	80.0
NPL2	8.9	656.7	722.5	65.9
NPL3	17.8	657.0	722.7	46.2
NPL4	44.5	657.5	721.4	19.5
NPL5	89	658.7	723.3	8.6

Table 5.5. Fluorescence emission of *m*THPC in ethanol and *m*THPC-HSA in aqueous solution

Lr: Loading ratio *m*THPC/HSA; λ_{max}: Location of fluorescence maximum; Φ_{FL}: Fluorescence quantum yield.

[a]: Standard: *m*THPC in ethanol.

5.2.4 Fluorescence kinetic parameters

Fluorescence lifetimes (τ) and their amplitudes of *m*THPC in ethanol and *m*THPC-HSA nanoparticles in aqueous solutions are shown in Table 5.6. The fluorescence decay curves of *m*THPC-HSA nanoparticles are shown in Fig. 5.7.

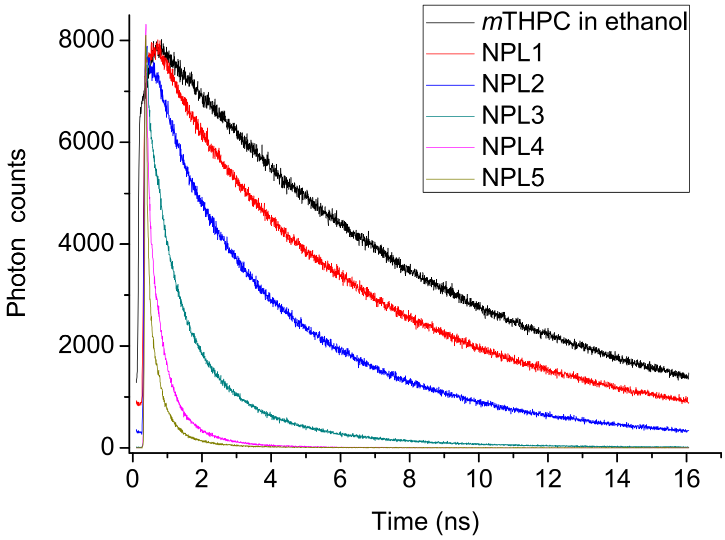

Fig. 5.7. Fluorescence decay curves of *m*THPC and of *m*THPC-HSA nanoparticles with different loading ratios

Samples	τ_1 [ns] ± 0.2 / A [%]	τ_2 [ns] ± 0.1 / A [%]	τ_3 [ns] ± 0.1 / A [%]	τ_4 [ns] ± 0.05 / A [%]	τ_5 [ns] ± 0.02 / A [%]	χ^2
*m*THPC	8.5 / 100	-	-	-	-	1.06
NPL1	8.5 / 51.3	3.5 / 26.8	-	0.37 / 21.9	-	1.1
NPL2	8.0 / 12.4	3.5 / 34.9	0.6 / 19.5	-	0.056 / 33.3	1.15
NPL3	-	3.4 / 6.4	1.3 / 21.0	0.35 / 25.6	0.040 / 46.9	1.08
NPL4	-	-	1.0 / 6.8	0.29 / 27.7	0.040 / 65.5	1.14
NPL5	-	-	0.8 / 3.3	0.20 / 15.8	0.027 / 80.9	1.12

Table 5.6. Fluorescence decay parameters of *m*THPC in ethanol and of *m*THPC-HSA nanoparticles with different loading ratios in aqueous solutions; λ_{exc}: 532 nm; λ_{obs}: 650 nm

Fluorescence lifetime results coincide with fluorescence quantum yields. The fluorescence lifetime of *m*THPC in ethanol is τ_1=8.5 ns. The fluorescence lifetime of *m*THPC in the HSA nanoparticles strongly depends on the drug loading ratio. Moreover, in difference to the dye in solution, multi-exponential decay behaviour was found. The lifetime τ_1 (8.0 and 8.5 ns) is very similar to the fluorescence lifetime of *m*THPC in ethanol and is therefore attributed to “lone standing” molecules in the nanoparticles behaving as monomers. The lifetime τ_1 contributes more than 50% to the total fluorescence signal of NPL1. The percentage of τ_1 decreases to 12.4% for NPL2. Interestingly, τ_1 disappears in NPL3, which indicates that no more “lone standing" *m*THPC monomers contribute to emission. The fluorescence signal of NPL3 contains 6.4% of τ_2 (3.3–3.5 ns), which could probably be attributed to *m*THPC-HSA interaction. τ_2 was observed for NPL1, NPL2, and NPL3. The contribution of τ_2 is less than 0.1% when the *m*THPC loading ratio is higher than 17.8 µg/mg. The dominant parts in the fluorescence signal are three shorter fluorescence lifetimes (τ_3, τ_4, and τ_5) when the loading ratio is higher than 44.5 µg/ mg.

The disappearance of τ_1 and τ_2 in the fluorescence decay of NPL4 and NPL5 exhibits that the *m*THPC-HSA interaction mechanism is negligible compared with *m*THPC-*m*THPC interaction. Due to the strong dye-dye interactions, the fluorescence decay of high loading ratio samples NPL4 and NPL5 contains only three short lifetimes, τ_3, τ_4, and τ_5. Thereby, τ_3 (0.6–1.3 ns) and τ_4 (0.19–0.37 ns) probably indicate different *m*THPC-*m*THPC traps, which means photosensitizers with excited state interaction cause a much faster decay time and much lower emission [Hackbarth 2005].

The contribution of the shortest lifetime τ_5 caused by energy transfer to total fluorescence decay signal increases significantly from 33.3% for NPL2 to 80.9% for NPL5 (Table 5.6). The fluorescence quantum yield of *m*THPC-HSA nanoparticles noticeably decreases from 65.9% for NPL2 to 8.6% for NPL5. This observation is typical for strong interacting molecules of random orientation.

Low loading ratio samples exhibit stronger interaction between *m*THPC and HSA (monomer *m*THPC) as the interaction can be followed by absorption, steady-state fluorescence, and fluorescence lifetime analysis. In contrast, high loading ratio samples indicate stronger interaction between *m*THPC molecules (traps, electronic energy transfer, etc.).

5.2.5 Singlet oxygen generation and triplet lifetime in solution

Singlet oxygen data and triplet lifetime of *m*THPC in ethanol and of *m*THPC-HSA nanoparticles measured in D_2O are summarized in Table 5.7. Laser flash photolysis results are shown in Fig. 5.8.

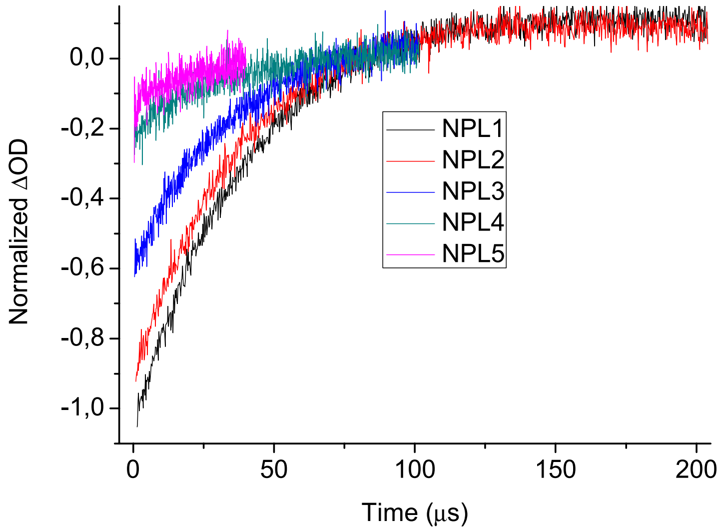

Fig. 5.8a. Triplet decay curves of *m*THPC-HSA nanoparticles in D_2O under normal air conditions. λ_{exc}: 652 nm; λ_{obs}: 470 nm

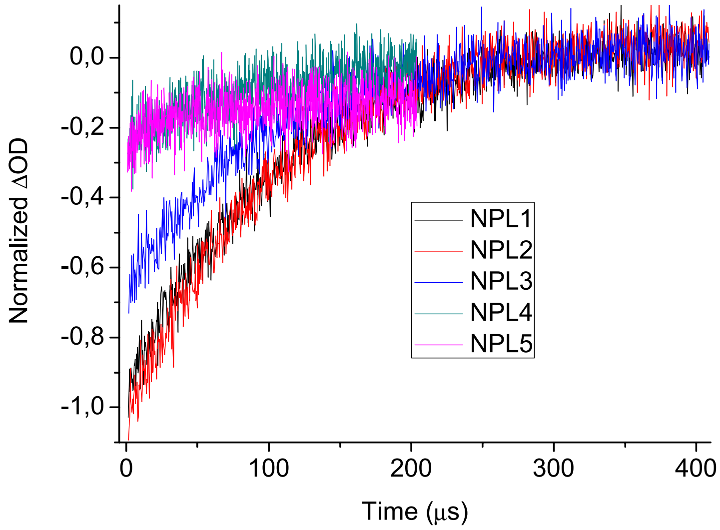

Fig. 5.8b. Triplet decay curves of *m*THPC-HSA nanoparticles in D_2O after 40 min N_2 flushing. λ_{exc}: 652 nm; λ_{obs}: 470 nm

Samples	τ_{Tair} [μs]	τ_{TN2} [μs]	f_{ET}	ΔOD [a]	τ_Δ [μs]	Φ_Δ (±0.02) [b]
NPL1	38 ± 3	106 ± 10	0.64	1	65 ± 5	0.04
NPL2	35 ± 3	103 ± 10	0.66	0.86	67 ± 5	0.03
NPL3	35 ± 3	98 ± 10	0.64	0.56	68 ± 5	< 0.03
NPL4	33 ± 3	104 ± 10	0.68	0.20	-	-
NPL5	41 ± 4	47 ± 4	0.13	0.14	-	-

Table 5.7. PDT-relevant photophysical parameters of *m*THPC-HSA nanoparticles: triplet lifetime obtained under normal conditions: τ_{Tair}, for air-depleted samples; τ_{TN2}, singlet oxygen lifetime (τ_Δ); and singlet oxygen quantum yield (Φ_Δ).

[a] The change of absorption (ΔOD) of NPL1 is taken as standard.

[b] All samples were excited at 652 nm in singlet oxygen measurement. TPPS in D_2O is taken as singlet oxygen quantum yield standard ($\Phi_\Delta = 0.70$).

Owing to low absorption and strong scattering of *m*THPC-HSA nanoparticles, determining the triplet quantum yield Φ_T using picosecond-transient absorption spectroscopy (TAS) is difficult. However, the changing tendency of Φ_T can be evaluated using ΔOD values obtained from laser flash photolysis experiments (Table 5.7). The ΔOD indicates that Φ_T decreases when the *m*THPC loading ratio increases. The relative ΔOD decreases from 1 for NPL1 to 0.14 for NPL5, which means high loading ratio samples may have efficient triplet-triplet quenching (Fig. 5.8, Table 5.7). The low Φ_T and fluorescence quantum yield Φ_{FL} (Table 5.5) show that non-radiative intermolecular deactivation processes play the leading role in high loading ratio samples due to dye-dye interaction.

The factor $f_{ET}=(\tau_{TN2}-\tau_{Tair}) / \tau_{TN2}$ contains some information about singlet oxygen quantum yield Φ_Δ. The triplet lifetime τ_{Tair} under normal air condition is determined by $\tau_{Tair}= (k_{phor} + k_{non\text{-}rad} + k_{ET}[O_2])^{-1}$ [Regehly 2007]. The triplet lifetime τ_{TN2} after oxygen removal is given by $\tau_{Tair}= (k_{phor} + k_{non\text{-}rad})^{-1}$. The triplet lifetime τ_{Tair} under normal air condition of *m*THPC in ethanol was determined to be 0.23 μs, and τ_{TN2} after oxygen removal was 36 μs. Singlet oxygen quantum yields in ethanol and water are different due to the different oxygen concentrations. Therefore, the singlet oxygen generation of TPPS in D_2O was measured as reference. The triplet lifetime τ_{Tair} under normal air condition of TPPS in D_2O was determined to be 1.85 μs, and $\tau_{TN2,}$ after oxygen removal is 99 μs. The factor $f_{ET}=(\tau_{TN2}-\tau_{Tair}) / \tau_{TN2}$ of TPPS in D_2O and *m*THPC in ethanol are in the range of 0.98–0.99, which indicates that 98%–99% triplet state photosensitizer molecules participate in singlet oxygen generation. This relates to their high singlet oxygen quantum yields (0.70 for TPPS in D_2O and 0.63 for *m*THPC in ethanol).

However, *m*THPC-HSA nanoparticles in D_2O have a long triplet lifetime τ_{Tair} (33–41 μs) under normal air condition (Table 5.7) compared to “free” photosensitizer TPPS in D_2O (1.85 μs) and *m*THPC in ethanol (0.23 μs). This long triplet lifetime indicates a change of oxygen diffusion rate within the microenvironment of *m*THPC-HSA nanoparticles. This may be caused by factors related to the preparation procedure of *m*THPC-HSA nanoparticles since many factors can influence oxygen concentration, such as pH value, solvents, and the cross-linking structure of HSA nanoparticles.

The τ_{TN2} of oxygen-depleted *m*THPC-HSA nanoparticles was determined to be in the range of 98–106 μs, except NPL5. The factor f_{ET} of all *m*THPC-HSA nanoparticles, except for this sample, is in a narrow range of 0.64–0.68 (Table 5.7). For NPL5, the factor f_{ET} is 0.13. This factor coincides with its low singlet oxygen quantum yield (Table 5.7).

In D_2O, only NPL1, NPL2, and NPL3 are able to generate singlet oxygen with low quantum yield Φ_Δ (Table 5.7). This is possible because some of *m*THPC molecules behave like monomers. The singlet oxygen lifetime of *m*THPC-HSA nanoparticles dissolved in D_2O is in the range of 65–68 μs. This coincides with TPPS in D_2O value of 64 μs. This means singlet oxygen generated from *m*THPC diffuses out of the nanoparticles into D_2O environment or it is generated on the surface of the nanoparticles.

As can be seen from the photophysical characterization and singlet oxygen generation results, the choice of *m*THPC loading ratio should be a compromise between loading efficiency and photophysical properties. HSA nanoparticles cannot be utilized efficiently when the loading ratio is lower than 17.8 μg/mg. However, no detectable singlet oxygen generation can be obtained for high loading ratios starting from 44.5 μg/mg. For this reason, a fixed value in a narrow range of *m*THPC loading ratio, approximately 17–20 μg/mg, was chosen for further investigation.

5.3 Photophysical investigations of *m*THPC-HSA with different cross-linkages

HSA nanoparticles are connected by cross-linker glutaraldehyde. Aldehyde concentration ranges from 40% to 200% of the theoretic amount of the quantity necessary for connection to 59 amino groups in HSA. In a former work, the influence of cross-linker on particle size, zeta potential, and available surface amino group, as well as long-term storage, were studied [Lin et al. 1993, Roser 1993, Weber 2000]. In this section, the influence of the cross-linker of the HSA nanoparticles on photophysical properties is investigated. This parameter is changed via different amounts of glutaraldehyde cross-linker added into the HSA molecules during preparation.

The series of samples in this section were loaded at very similar ratios. Cross-linking of the HSA nanoparticles is presented in Table 5.8.

	CL	Lr (µg / mg)
NPC40	40%	19.05
NPC100	100%	20.71
NPC200	200%	20.59

Table 5.8. Sample description: *m*THPC-HSA nanoparticles with different cross-linkages
CL: HSA cross-linking; Lr: Loading ratio *m*THPC/HSA

5.3.1 Absorption and steady-state fluorescence

The amount of cross-linkers can change the number of available amino groups on the surface of HSA nanoparticles. The influence of changing cross-linkage on HSA NPs drug loading has been reported [Rubino 1993]. The final goal of the "NanoCancer" project is the stable and repeatable conjugation between photosensitizer and HSA nanoparticles. In this context, the photophysical properties, including absorption and steady-state fluorescence, were measured in order to investigate *m*THPC-HSA NPs with different amounts of cross-linker.

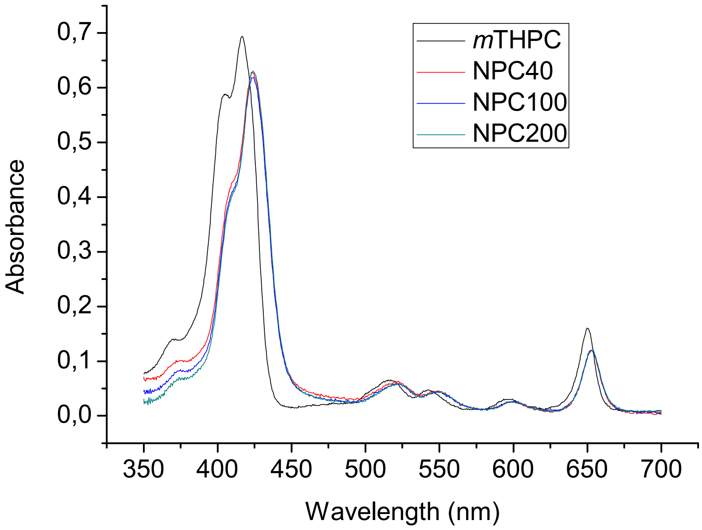

Fig. 5.9. UV-vis absorption spectra of *m*THPC in ethanol and of *m*THPC-HSA nanoparticles with different cross-linkages in aqueous solution (scattering corrected)

The absorption spectra of the three *m*THPC-HSA nanoparticle samples have similar shapes and extinction coefficient. The different degrees of cross-linking do not influence the absorption properties of the dye molecules.

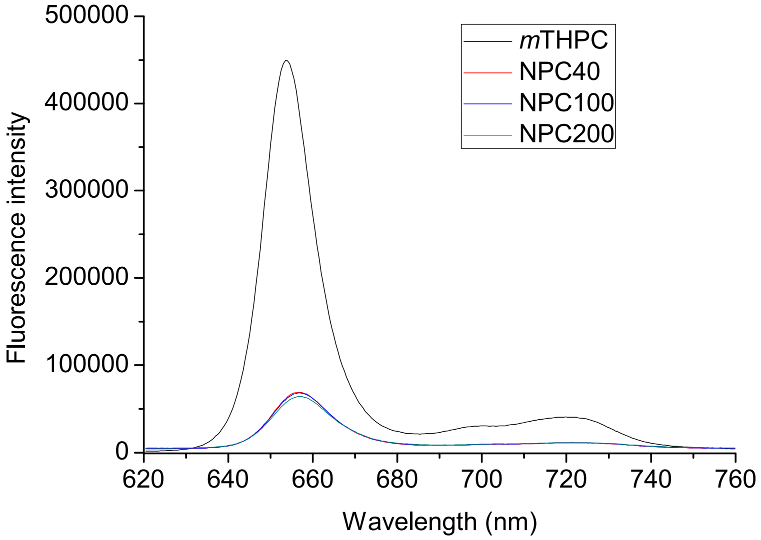

Fig. 5.10. Fluorescence spectra of *m*THPC in ethanol and *m*THPC-HSA nanoparticles with different cross-linkages in aqueous solution

The maximum *m*THPC-HSA nanoparticles fluorescence of the $S_{1,0} \rightarrow S_{0,0}$ transitions locates at 657 nm, while the fluorescence peak of *m*THPC is at 654 nm in ethanol. The fluorescence quantum yield of all three *m*THPC-HSA nanoparticle samples is approximately 30% relative to *m*THPC.

5.3.2 Fluorescence kinetic parameters

	τ_1 [ns] ± 0.1 / A [%]	τ_2 [ns] ± 0.1 / A [%]	τ_3 [ns] ± 0.05 / A [%]	τ_4 [ns] ± 0.010 / A [%]	χ^2
NPC40	2.7 / 9.9	0.9 / 24.2	0.17 / 30.2	0.027 / 35.6	1.1
NPC100	2.3 / 10.2	0.8 / 26.1	0.20 / 28.5	0.042 / 35.2	1.06
NPC200	2.1 / 10.3	0.7 / 30.6	0.21 / 25.6	0.045 / 33.5	1.07

Table 5.9. Fluorescence decay parameters of *m*THPC-HSA nanoparticles with different cross-linkages in aqueous solutions; A: amplitude; λ_{exc}: 532 nm; λ_{obs}: 650 nm

The fluorescence decay of *m*THPC-HSA nanoparticles consists of four fluorescence lifetime species (Table 5.9). However, three *m*THPC-HSA nanoparticles have similar fluorescence decays. Monomer-like *m*THPC molecules do not contribute to the fluorescence of these *m*THPC-HSA nanoparticles since τ_1 is much shorter than the fluorescence lifetime of *m*THPC in ethanol.

The differences among absorption and fluorescence spectra of NPC40, NPC100, and NPC200 are negligible (Figs. 5.9 and 10). Both the fluorescence decay times and amplitudes of three *m*THPC-HSA samples are quite similar (Table 5.9). *m*THPC-HSA nanoparticles with different degrees of HSA cross-linking show no systematic differences in absorption, steady-state, and time-resolved fluorescence. This means that these parameters only depend on dye loading of the nanoparticles. They are independent of the density/rigidity of the HSA matrix.

5.3.3 Singlet oxygen generation and laser flash photolysis

Absorption and fluorescence spectra prove that different cross-linkers have no influence on photosensitizer molecules in the ground state and excited singlet states. In the next step, the work should move to characterization of the PS in triplet state as well as to its energy transfer to molecular oxygen. Singlet oxygen luminescence determination and laser flash photolysis are used to achieve this goal.

Singlet oxygen and triplet lifetimes of the *m*THPC-HSA nanoparticles are shown in Table 5.10.

	τ_{Tair} [μs] ± 3 [a]	τ_Δ [μs] ± 5 [b]	Φ_Δ (±0.02)
NPC40	30	67	0.04
NPC100	36	66	0.03
NPC200	42	55	0.03

Table 5.10. PDT-relevant photophysical parameters of *m*THPC-HSA nanoparticles with different cross-linkages in D_2O; triplet lifetime under normal conditions; τ_{Tair}, singlet oxygen lifetime (τ_Δ); and singlet oxygen quantum yield (Φ_Δ).

[a] Data obtained from laser flash photolysis.

[b] All samples were excited at 652 nm in singlet oxygen measurement. TPPS in D_2O is taken as the singlet oxygen quantum yield standard ($\Phi_\Delta = 0.70$).

*m*THPC-HSA nanoparticles have a long triplet lifetime τ_{Tair} under normal air condition. This decay time increases with rising cross-linking of the HSA nanoparticles. τ_{Tair} (42 μs) of NPC200 is slightly longer than the value of NPC40 (30 μs) and NPC100 (36 μs) (Table 5.10). The longer triplet lifetime of NPC200 illustrates that stronger cross-linkage may induce less oxygen accessibility or diffusion within the dye microenvironment than in NPC40 and NPC100.

The long singlet oxygen lifetime τ_Δ of NPC40 (67 μs) and NPC100 (66 μs) (Table 5.10) in D_2O indicates that singlet oxygen diffuses out of the nanoparticles. For NPC40 and NPC100, singlet oxygen lifetime equals to the standard value in D_2O (64–70 μs). The shorter singlet oxygen lifetime τ_Δ of NPC200 (55 μs) indicates weak singlet oxygen quenching. This effect could be caused by the tight inner structure of NPC200. HSA is an efficient singlet oxygen quencher [Davila 1990]. This suggests that the probability of singlet oxygen quenching during diffusion is higher because of more densely cross-linked HSA molecules in NPC200.

Singlet oxygen quantum yield Φ_Δ of the three *m*THPC-HSA nanoparticles is low. Among them, Φ_Δ of NPC40 (0.04) (Table 5.10) is slightly higher than the value of the other samples (0.03). This coincides with its shorter triplet lifetime τ_{Tair}, which illustrates a looser HSA cross-linking structure with higher local oxygen concentration. However, this difference can be negligible.

The photosensitized intracellular singlet oxygen luminescence in Jurkat cells incubated with *m*THPC and NPC40, and NPC100 and NPC200 was investigated.

5.3.4 Singlet oxygen luminescence detection in Jurkat cells

Cross-linkage is considered an impact factor on biodegradability and drug release from the carrier system [Lee et al. 1981]. It is convenient if rapid and controllable drug release in targeting cells can be attained via adjusting glutaraldehyde cross-linker. Thus, in this section, the methods of singlet oxygen luminescence detection and laser flash photolysis are used in order to check the influence of cross-linker on drug release.

Singlet oxygen generated from *m*THPC is relatively independent of incubation time. It has only a slight reduction of singlet oxygen lifetime for 24 h incubation (Fig. 5.11a).

In the case of *m*THPC-HSA nanoparticles, an increase of singlet oxygen lifetime τ_Δ with incubation time of the cells can be clearly seen. After 1 h incubation, τ_Δ of *m*THPC-HSA nanoparticles is in the range of 0.3–0.4 µs. This value gives an impression of *m*THPC liberation from HSA nanoparticles [Preuß 2010]. With increasing incubation time, the singlet oxygen lifetime becomes longer. For NPC40 and NPC100, τ_Δ increases to the level of 0.55–0.6 µs after 24 h incubation. It is close to τ_Δ of *m*THPC (Fig. 5.11a). This can be explained by photosensitizer liberation from the nanoparticles. However, τ_Δ of NPC200 (0.5 µs) still falls short compared to other samples after 24 h incubation. This finding suggests an incomplete release process of *m*THPC from the nanoparticles, which coincides with the phototoxicity results [Preuß 2010].

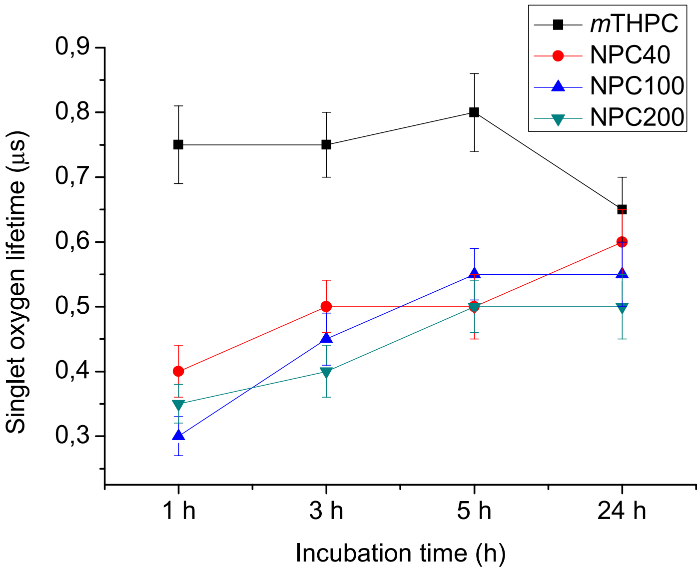

Fig. 5.11a. Singlet oxygen lifetime in Jurkat cells incubated with *m*THPC and *m*THPC-HSA nanoparticles with different cross linkages. *m*THPC Conc. 3 µM; illumination wavelength: 652 nm; illumination time: 20 s; laser power: 1.5 mW; light dose: 1 µJ / cell

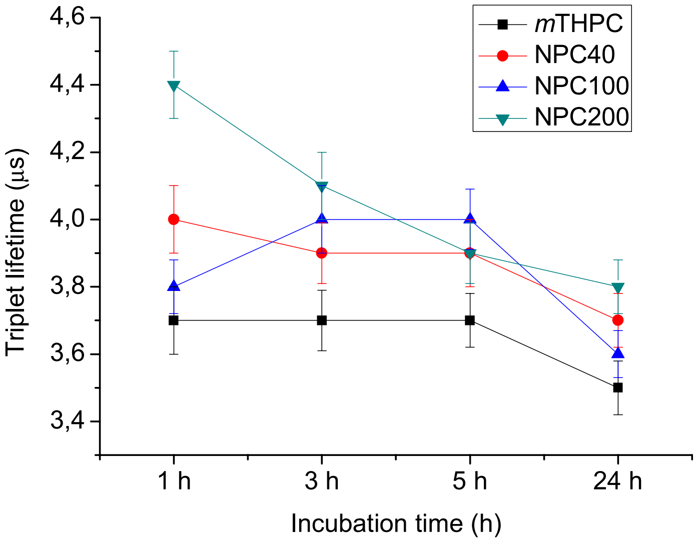

Fig. 5.11b. Triplet lifetime of the photosensitizer *m*THPC in Jurkat cells incubated with *m*THPC and *m*THPC-HSA nanoparticles with different cross linkages

Intracellular triplet lifetime also indicates *m*THPC release from HSA nanoparticles. The triplet lifetime τ_{Tair} of *m*THPC in cells remains unchanged with a value of 3.7 µs for the different incubation times of 1, 3, and 5 h (Fig. 5.11b). After 24 h incubation, the triplet lifetime of *m*THPC in Jurkat cells is 3.5 µs. The deviation is within the range of measurement error. In contrast, the triplet lifetimes of *m*THPC-HSA nanoparticles show a decreasing tendency with increasing cell incubation time. The triplet lifetime of NPC200 after 1 h incubation is 4.4 µs. After 24 h incubation, it is decreased to 3.8 µs. τ_{Tair} of NPC40 and NPC100 after 1 h incubation are 3.8 and 4.0 µs, respectively. τ_{Tair} of NPC40 and NPC100 is between 3.6 and 3.8 µs after 24 h incubation, which is longer than that of *m*THPC but much shorter than that of NPC200. This result also illustrates drug release from HSA nanoparticles. However, τ_{Tair} of NPC200 for all the times is slightly longer than other samples, which assumes an incomplete *m*THPC release from NPC200. Controllable intracellular drug release can be achieved by adjusting the amount of glutaraldehyde.

5.4 Conclusions

Preparations for both *m*THPP-HSA nanoparticles generate singlet oxygen luminescence in solution. Singlet oxygen quantum yield of LLPP-HSA (low loading ratio sample) is higher than HLPP-HSA (high loading ratio sample). The singlet oxygen lifetime of *m*THPP-HSA, however, is shorter than normal value (63–70 μs) in D_2O. It seems that singlet oxygen quenching occurs in this photosensitizer-nanoparticle system.

The photophysical properties of *m*THPC-HSA nanoparticles such as absorption and fluorescence spectra, as well as fluorescence lifetime, mainly depend on loading ratio. Low loading ratio samples exhibit stronger interaction between *m*THPC and HSA (monomer *m*THPC) as it can be followed by absorption, steady-state fluorescence, and fluorescence lifetime analysis. For low loading ratio samples (< 17.8 μg/mg), the leading mechanism is *m*THPC-HSA interaction. The fluorescence lifetime and fluorescence quantum yield illustrate that low loading ratio *m*THPC-HSA nanoparticles contain a fraction of *m*THPC behaving like monomers. On the contrary, *m*THPC-*m*THPC interaction (traps, electronic energy transfer, etc.) becomes the prior interaction mechanism in high loading ratio samples (> 17.8 μg/mg).

The choice of *m*THPC loading ratio is a balance between photophysical properties and loading efficiency. A narrow range of loading (17–20 μg/mg) was determined when considering both properties. *m*THPC-HSA nanoparticles with loading ratio in this range still have capability to generate singlet oxygen in a detectable amount. At the same time, the loading ratio is sufficiently high for full utilization by HSA nanoparticles. For further investigation, the drug loading ratio for all of *m*THPC-HSA nanoparticles was chosen from within this range.

The cross-linkage influences photophysical properties that concern photosensitizer-oxygen interaction such as the triplet lifetime τ_{Tair} and singlet oxygen lifetime τ_Δ. NPC200 has the longest triplet lifetime. This means that the oxygen concentration within the microenvironment of *m*THPC-HSA nanoparticles is strongly influenced by the amount of cross-linkages. Triplet lifetime τ_{Tair} can be used as a realistic indicator for HSA NPs cross-linkage determination due to its high sensitivity and repeatability. In HSA nanoparticles with high number of cross-linkages, singlet oxygen can be quenched, resulting in shortened singlet oxygen lifetime.

The singlet oxygen generation and triplet lifetime of Jurkat cells incubated with *m*THPC-HSA indicates that all samples generate singlet oxygen inside cells. After 24 h incubation, the *m*THPC molecules are released from the NPC40 and NPC100. In contrast, the high amount of cross-linkages makes NPC200 an unideal candidate as drug carrier since the required time for *m*THPC release is too long. This can be explained by incomplete HSA nanoparticle decomposition because of strong particle matrix cross-linking.

6. PLGA -nanoparticles as biodegradable carrier system for PDT

In Chapter 5, photophysical properties of *m*THPP- and *m*THPC-HSA nanoparticles, as well as intracellular drug release and singlet oxygen generation, were discussed. As another interesting biodegradable nanoparticle, photosensitizer-combined PLGA nanoparticle was prepared [Konan 2002b] and evaluated in EMT-6 mammary tumor cells [Konan 2003b]. Photophysical characterization to photosensitizer-loaded PLGA NPs and the intracellular singlet oxygen generation are discussed in this chapter. In particular, the highlight will be the research of drug release from PLGA matrices in organic solvent, cell culture media, and inside cells by monitoring the triplet lifetime of photosensitizer. This is carried out using laser flash photolysis.

6.1 Comparison of the photophysical properties of *m*THPP- and *m*THPC-PLGA

*m*THPP and *m*THPC molecules were incorporated into the PLGA nanoparticles matrix. Dispersion medium of the *m*THPP-and *m*THPC-PLGA nanoparticles is distilled water. Concentrations of incorporated *m*THPP and *m*THPC are 0.720 and 0.768 mg/ml, respectively. For *m*THPP-PLGA nanoparticles, the loading ratio is 89.53 µg *m*THPP/mg PLGA. For *m*THPC-PLGA nanoparticles, the loading ratio is 83.21 µg *m*THPC/mg PLGA.

6.2 Absorption and steady-state fluorescence

To compare photophysical properties of *m*THPP and *m*THPC-PLGA NPs, absorption and steady-state fluorescence are taken as follows.

UV-vis absorption spectra of *m*THPP, *m*THPC, *m*THPP-, and *m*THPC-PLGA were measured. If without special descriptions, *m*THPP and *m*THPC were dissolved in ethanol. *m*THPP- and *m*THPC-PLGA were diluted with distilled water. The absorption spectra of *m*THPP, *m*THPC, *m*THPP-, and *m*THPC-PLGA are shown in Fig. 6.1.

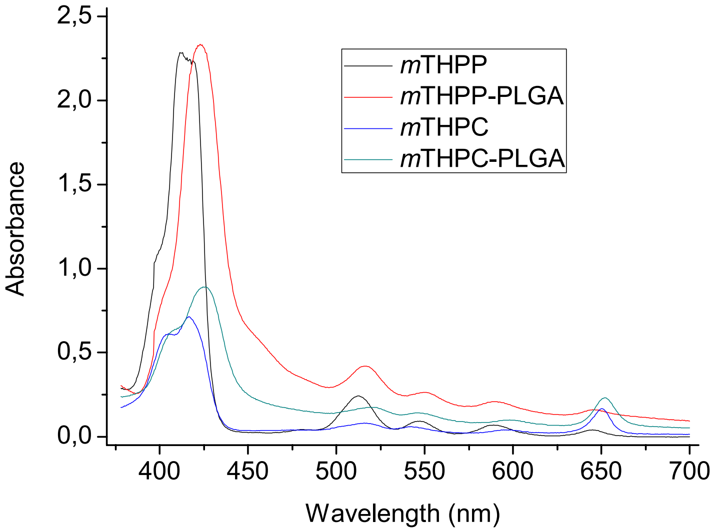

Fig. 6.1a. UV-vis absorption spectra of *m*THPP, *m*THPC in ethanol, and *m*THPP- and *m*THPC-PLGA nanoparticles in aqueous environment

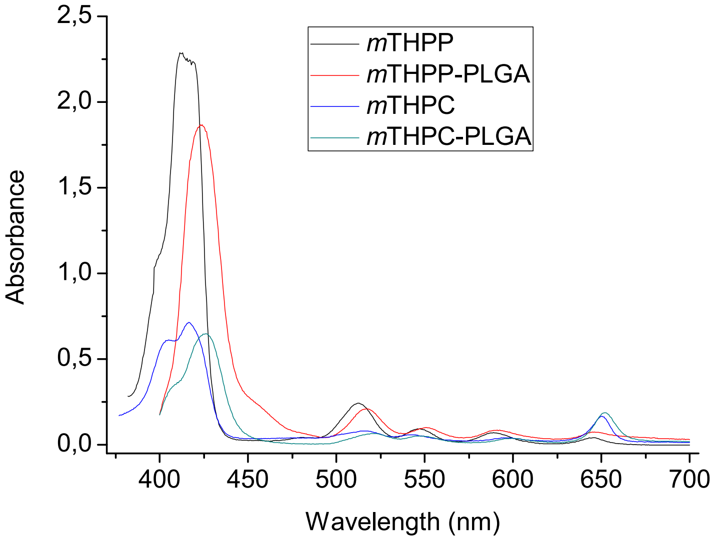

Fig. 6.1b. UV-vis absorption spectra of *m*THPP, *m*THPC in ethanol, and *m*THPP- and *m*THPC-PLGA nanoparticles in aqueous environment, scattering corrected

As shown in Fig. 6.1a, the maximum of the Soret band of *m*THPP is located at 413 nm. For *m*THPP-PLGA, it is bathochromically shifted to 423 nm. The real extinction from absorption when scattering is considered is shown in Fig. 6.1b. The absorption at Q band region is drawn separately in Fig. 6.1c to get a better view of Q band region. The four Q band maxima of *m*THPP-PLGA locate at 515, 550, 590, and 646 nm. At the same time, their *m*THPP counterparts are at 512, 546, 588, and 645 nm. Although

Q band maxima of *m*THPP-PLGA have also systematically red-shifted, the shift is not as significant as at the Soret band maximum.

After scattering correction, the absorption of the *m*THPC-PLGA is very similar to that of *m*THPC in ethanol, except in the shift of absorption maxima. The Soret band maximum of the *m*THPC-PLGA absorption spectrum locates at 425 nm, while the Soret band maximum of the absorption spectrum of *m*THPC is at 416 nm. This shift is probably caused by the interaction of *m*THPC with the PLGA matrix. The four Q band maxima in the absorption of *m*THPC are located at 515, 541, 594, and 650 nm. Their counterparts in the absorption of *m*THPC-PLGA shift to 520, 546, 597, and 652 nm.

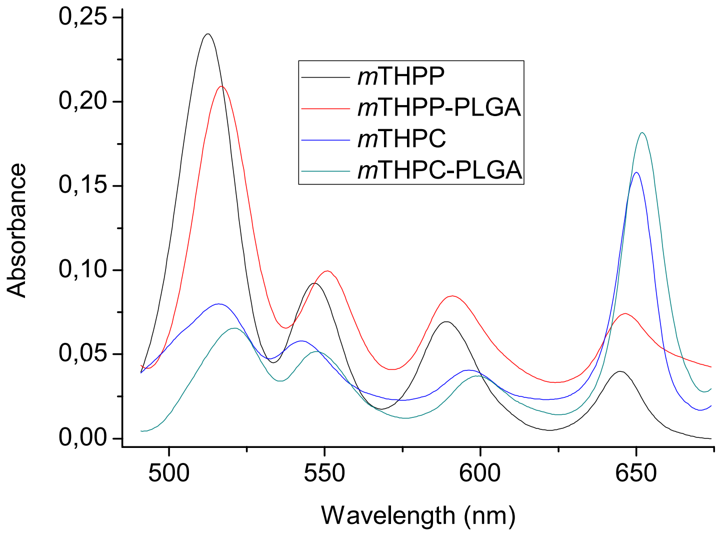

Fig. 6.1c. UV-vis absorption spectra of *m*THPP, *m*THPC in ethanol, and *m*THPP- and *m*THPC-PLGA in aqueous solution at Q band region

Due to the degeneration of one double bond, the chlorin *m*THPC has a stronger absorption in the Q_x (0, 0) band than the porphyrin *m*THPP. The extinction coefficient of *m*THPC at 650 nm is approximately 24000 $Mol^{-1}cm^{-1}$, which is three fold higher than that of *m*THPP (Fig. 6.1c). 650 nm is suitable for PDT. For this reason, *m*THPC is regarded as a better photosensitizer than *m*THPP [Berenbaum 1993].

The steady-state fluorescence of *m*THPP and *m*THPP-PLGA was excited at 414 nm. The steady-state fluorescence of *m*THPC and *m*THPC-PLGA was excited at 506 nm. Normalized fluorescence spectra of *m*THPP, *m*THPC, *m*THPP-, and *m*THPC-PLGA are shown in Fig. 6.2.

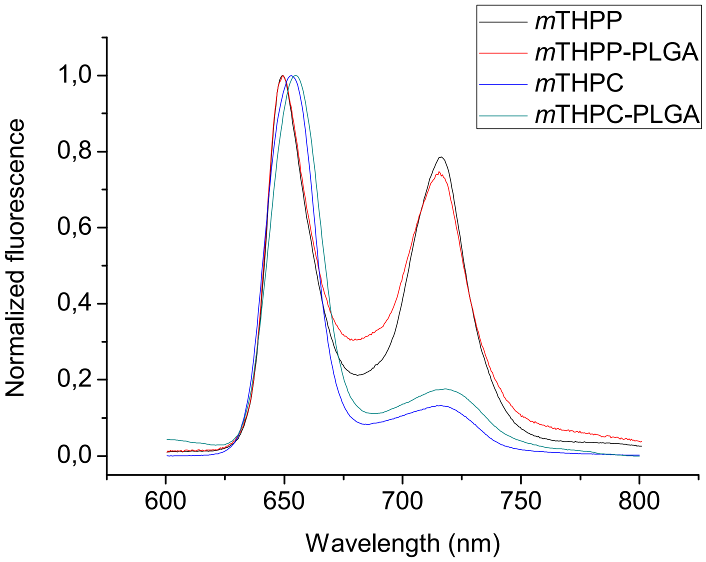

Fig. 6.2. Steady-state fluorescence of *m*THPP, *m*THPC in ethanol, and *m*THPP- and *m*THPC-PLGA in water, data normalized

Compared to *m*THPP in ethanol, the relative fluorescence quantum yield of *m*THPP-PLGA is 0.38. Compared to 653 nm of *m*THPC in ethanol, the fluorescence peak of the $S_{1,0} \rightarrow S_{0,0}$ transition for *m*THPC-PLGA nanoparticles is slightly shifted to 654.5 nm. Compared to *m*THPC, the relative fluorescence quantum yield of *m*THPC-PLGA was calculated to be 0.07. The reduction of fluorescence quantum yield and appearance of different fluorescence decay times prove the occurrence of interactions between chromophores and PLGA matrix.

To make full utilization of drug carriers, high drug loading ratio should be achieved. Nevertheless, prior evaluation of the influence of loading ratio on drug-loaded nanoparticles in vivo and clinical tests must be conducted.

6.3 Fluorescence kinetic parameters and DAFS

In Chapter 5, the influence of drug loading ratio on the photophysical properties of photosensitizer-loaded HSA nanoparticles, especially singlet oxygen generation, was shown. Fluorescence decay and singlet oxygen generation of *m*THPP- and *m*THPC-PLGA nanoparticles with different loading ratios are studied in Sections 6.3 and 6.4, respectively.

*m*THPP and *m*THPC were encapsulated into PLGA matrices with different loading ratios. The dispersion medium of *m*THPP- and *m*THPC-PLGA is distilled water. The loading ratio of each sample is listed in Table 6.1.

	PS	Lr (µg / mg)
PNPL1	*m*THPP	2.39
PNPL2	*m*THPP	10.07
PNPL3	*m*THPP	89.53
CNPL1	*m*THPC	1.72
CNPL2	*m*THPC	9.08
CNPL3	*m*THPC	83.21

Table 6.1. Description of three *m*THPP-PLGA and three *m*THPC-PLGA nanoparticles.
PS: photosensitizer; Lr: loading ratio PS / PLGA

Fluorescence decay times and amplitudes of *m*THPP and *m*THPC in ethanol, and *m*THPP- and *m*THPC-PLGA in aqueous environment are shown in Table 6.2. The decay-associated fluorescence spectra of *m*THPP- and *m*THPC-PLGA are shown in Figs. 6.3 and 6.4, respectively.

Samples	τ_1 [ns] ± 0.2 / A [%]	τ_2 [ns] ± 0.1 / A [%]	τ_3 [ns] ± 0.1 / A [%]	τ_4 [ns] ± 0.05 / A [%]	τ_5 [ns] ± 0.02 / A [%]	χ^2
*m*THPP	9.6 / 100	-	-	-	-	1.06
PNPL1	11.7 / 66.7	4.0 / 14.1	-	0.58 / 19.2	-	1.07
PNPL2	8.2 / 23.5	-	1.6 / 23.4	-	0.21 / 53.1	1.01
PNPL3	8.7 / 7.4	-	1.5 / 33.2	-	0.26 / 59.4	1.19
*m*THPC	8.5 / 100	-	-	-	-	1.06
CNPL1	8.0 / 29.5	-	-	0.75 / 26.0	0.15 / 44.5	1.18
CNPL2	-	3.9 / 10.6	1.1 / 29.5	-	0.22 / 60.0	1.13
CNPL3	-	2.8 / 0.3	-	0.52 / 7.8	0.14 / 91.9	1.27

Table 6.2. Fluorescence lifetime of *m*THPP and *m*THPC in ethanol, and *m*THPP- and *m*THPC-PLGA in aqueous solution. λ_{exc}: 532 nm; λ_{obs}: 717 nm

Table 6.2 and Fig 6.3 show the fluorescence of each *m*THPP-PLGA sample containing three different lifetimes. The fluorescence peaks of the $S_{1,\ 0} \rightarrow S_{0,\ 0}$ transitions for three different fluorescence components of *m*THPP-PLGA nanoparticles are all located at 650 nm (Fig. 6.3). This indicates that the three decay times are generated by *m*THPP. The amplitude of the longest lifetime τ_1 (> 8 ns) decreases as the drug loading ratio rises. In low loading ratio sample PNPL1, the amplitude of τ_1 is 66.7%. τ_1 usually represents monomer-like *m*THPP since the fluorescence lifetime of *m*THPP in ethanol (monomers) is 9.6 ns. In addition τ_1, the fluorescence signal of PNPL1 also contains τ_2 (4.0 ns, 14.1%) and τ_4 (0.58 ns, 19.2%). These indicate that *m*THPP molecules interact with PLGA matrices. In middle and high loading ratio samples PNPL2 and PNPL3, τ_1 is reduced to 23.5% and 7.4%, respectively. These results indicate the reduction of *m*THPP monomers in PLGA nanoparticles when the loading ratio increases. In these two samples, τ_2 and τ_4 are replaced by shorter lifetime τ_3 (1.5–1.6 ns) and the shortest lifetime τ_5 (0.21–0.26 ns). The shortened fluorescence lifetimes exhibit much closer *m*THPP-PLGA interactions. It might be related to the localization of *m*THPP in the PLGA matrix. One possible distribution of different fluorescence components could be that *m*THPP clusters are trapped deeply inside the network of PLGA matrix while monomers locate mainly near the surface of nanoparticles. Nevertheless, more evidence is needed in order to prove fluorescence decay times.

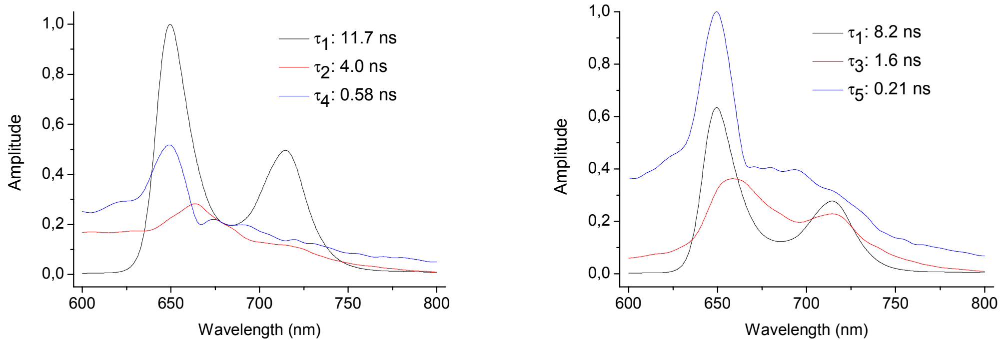

PNPL1 PNPL2

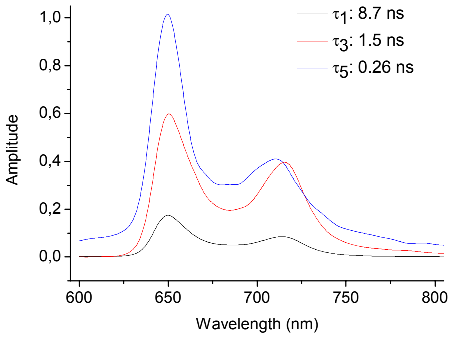

PNPL3

Fig 6.3. Decay-associated fluorescence spectra of *m*THPP-PLGA in water solution

The fluorescence decay behaviour of *m*THPC-PLGA nanoparticles differs from *m*THPP-PLGA nanoparticles. The fluorescence lifetime of *m*THPC in ethanol (monomers) is 8.5 ns. Only CNPL1, the sample with the lowest loading ratio, contains monomer-like *m*THPC (29.5%). For middle and high loading ratio samples CNPL2 and CNPL3, there are no monomer-like *m*THPC in the PLGA matrices. Even the lifetime τ_2 (2.8–3.9 ns) of these samples contributes only 10% and 0.3% to the whole fluorescence signal. The very strong lifetime shortening speaks of efficient interaction processes. The main part of fluorescence signal of CNPL3 is contributed by the shortest lifetime τ_5 (0.14 ns, 91.9%) (Table 6.2 and Fig. 6.4). These *m*THPC-PLGA interactions are correlated with the loading ratio. This means they are correlated with increasing interactions between the dye molecules. The low fluorescence quantum yield and the shortened fluorescence decay time indicate that the dominant deactivation processes are non-radiative [Hackbarth 2005]. A similar behaviour was found for photosensitizer-loaded HSA nanoparticles.

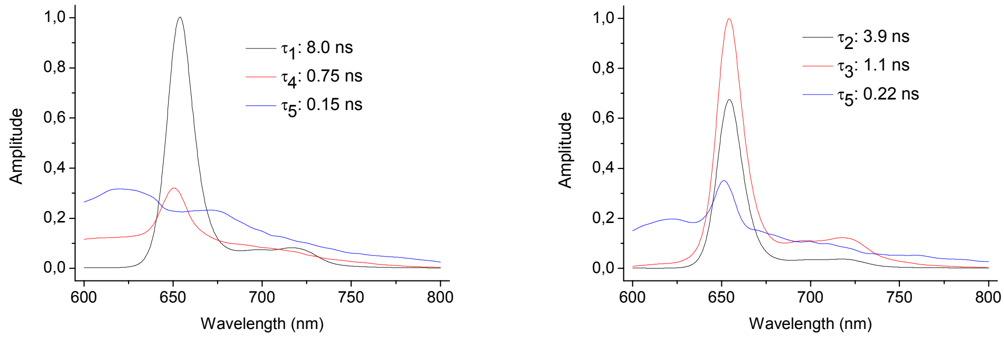

CNPL1 CNPL2

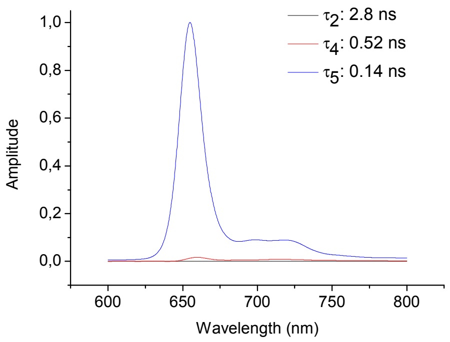

CNPL3

Fig 6.4. Decay-associated fluorescence spectra of *m*THPC-PLGA in water solution

This result illustrates that *m*THPC has a more pronounced tendency to aggregate in

PLGA nanoparticles than *m*THPP. The different behaviour of *m*THPP and *m*THPC-PLGA in fluorescence decay measurement should have a relation with the energy transfer efficiency between *m*THPP and *m*THPC dye molecules. The Förster radius of *m*THPP and *m*THPC in ethanol are 3.3 and 4.9 nm, respectively. The protonation of the imino nitrogen atoms will influence the electron distribution and change photosensitizer-photosensitizer interaction tendency. *m*THPC reduces the protonation capability because of its degeneration [Cunderlikova 2001]. Therefore, hydrophobicity of *m*THPC increases and thus leads to stronger aggregate tendency.

6.4 Singlet oxygen generation and triplet lifetime

Singlet oxygen quantum yield of PS-loaded HSA nanoparticles attenuates with increasing drug loading ratio (Chapter 5). PS-loaded PLGA NPs may not follow this pattern since PLGA NPs are produced by a different method. Photosensitizers are entrapped into matrices instead of surface-adsorbed. For this reason, whether or not the loading ratio determines singlet oxygen generation of PS-loaded PLGA NPs remains unknown.

In this section, the singlet oxygen generation of *m*THPP- and *m*THPC-PLGA in D_2O is measured. *m*THPP- and *m*THPC-PLGA nanoparticles have very weak singlet oxygen luminescence and shortened lifetimes, which leads to singlet oxygen quenching. Singlet oxygen generation and triplet lifetimes of *m*THPP, *m*THPC, *m*THPP-, and *m*THPC-PLGA in air-saturated solutions are shown in Table 6.3.

	τ_{Tair} [μs]	$\tau_{\Delta 1}$ [μs]	$\tau_{\Delta 2}$ [μs]	Φ_Δ [±0.03]
PNPL1	31 ± 2	-	51 ± 3	0.10
PNPL2	60 ± 1	-	43 ± 7	0.08
PNPL3	9.5 ± 0.2	6.1 ± 0.5 [86%]	74 ± 6 [14%]	0.05
CNPL1	29 ± 3	16.7 ± 0.3	-	0.12
CNPL2	24 ± 8	12.7 ± 0.3	-	0.11
CNPL3	22 ± 4	10.5 ± 0.2	-	0.08

Table 6.3. Singlet oxygen lifetime τ_Δ, singlet oxygen quantum yield Φ_Δ, and triplet lifetime τ_{Tair} of *m*THPP-PLGA and *m*THPC-PLGA. Singlet oxygen luminescence: λ_{exc}: 545 nm; Photosensitizer Conc.: 3 μM; OD: 0.1; Singlet oxygen quantum yield standard: Rose Bengal;

Solvent: D_2O. Laser flash photolysis: λ_{exc}: 591 nm; λ_{obs}: 488 nm

Typical singlet oxygen lifetime in D_2O is 60 μs. However, the situations of *m*THPP- and *m*THPC-PLGA nanoparticles are quite complex. For *m*THPP-PLGA, the singlet oxygen lifetime of the lowest loading ratio sample *m*THPP-PLGA PNPL1 is 51 μs. This indicates that the singlet oxygen generated by PNPL1 is only slightly quenched before diffusion into the surrounding D_2O.

On the contrary, the singlet oxygen luminescence from high loading ratio sample PNPL3 is strongly quenched. The time-resolved singlet oxygen luminescence curve can be fitted with two exponential decays. The singlet oxygen lifetime of 6.1 μs (86%) is attributed to singlet oxygen, which undergoes quenching effect during diffusion. However, a small amount of singlet oxygen (14%) is diffused outside PLGA nanoparticles without quenching. One possible explanation is that they represent singlet oxygen generated from different locations. For instance, singlet oxygen with long lifetime generates near the PLGA nanoparticles surface, while singlet oxygen with shortened lifetime generates deeply inside the nanoparticles.

Singlet oxygen generated from all three *m*THPC-PLGA nanoparticles is quenched. The singlet oxygen lifetime generated from low loading ratio sample is 16.7 μs. The singlet oxygen lifetime decreases with increasing loading ratio, which indicates stronger singlet oxygen quenching process in high loading ratio samples. For this reason, the singlet oxygen quantum yield of all samples is low. Obviously, Φ_Δ also decreases when the drug loading ratio increases. The observed decreased Φ_Δ can partially explain the experimental fact observed by Zeisser et al., where increasing drug loading ratio reduces the phototoxicity of Hypericin-loaded PLGA nanoparticles on NuTu-19 cells [Zeisser-Labouebe 2006].

Photosensitizer-loaded PLGA nanoparticles have longer triplet lifetimes under normal air condition compared to Rose Bengal. This coincides with singlet oxygen measurement. Two possible reasons may cause long triplet lifetime: inefficient energy transfer between triplet state photosensitizer and oxygen; and lower local oxygen concentration within PLGA matrices than in D_2O.

6.5 PLGA matrix decomposition in organic solvent

Controllable decomposing and drug release in hydrophobic/hydrophilic environment are the goals of designing a drug carrier system. In this section, *m*THPP- and *m*THPC-PLGA nanoparticles are dissolved in ethanol to investigate the PLGA degradation and drug release from PLGA nanoparticles.

*m*THPP and *m*THPC in ethanol, and *m*THPP- and *m*THPC-PLGA nanoparticles in aqueous solution, were used for comparison. Absorption spectra of *m*THPP, *m*THPC, *m*THPP-, and *m*THPC-PLGA are shown in Fig. 6.5.

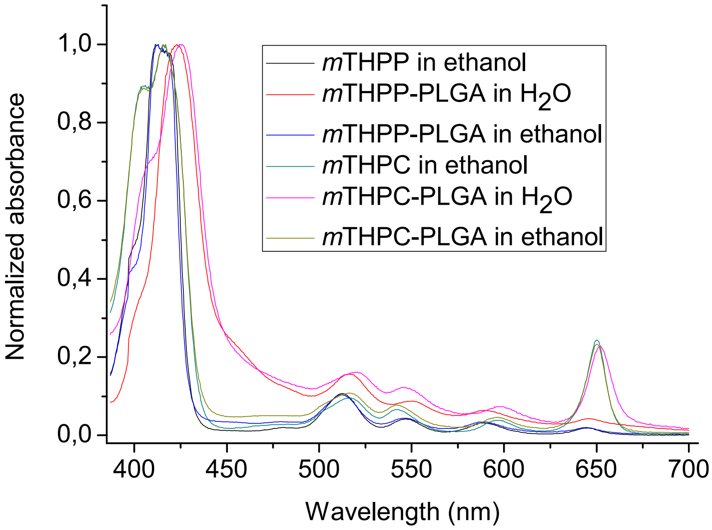

Fig. 6.5. UV-vis absorption spectra of *m*THPP and *m*THPC in ethanol, and of *m*THPP- and *m*THPC-PLGA in aqueous solution and in ethanol

In comparison with *m*THPP, the absorption maxima of *m*THPP-PLGA demonstrated bathochromic shift compared to *m*THPP, as mentioned in Section 6.2. However, *m*THPP-PLGA dissolved in ethanol exhibited no band shift. At the same time, the scattering caused by PLGA nanoparticles in absorption of *m*THPP-PLGA in water disappeared when the solvent was changed to ethanol. This illustrates that PLGA nanoparticles decompose to PLGA polymers when *m*THPP-PLGA is dissolved in ethanol. *m*THPP molecules trapped inside the PLGA matrix are released as monomers. This behaviour also exists in the absorption spectra of *m*THPC-PLGA nanoparticles.

The fluorescence quantum yield of *m*THPP-PLGA in ethanol reaches 0.97 of the value of *m*THPP. The relative fluorescence quantum yield of *m*THPP-PLGA in aqueous environment is only 0.38. The fluorescence quantum yield of *m*THPP-PLGA in ethanol also reaches 0.94. These two findings indicate that PLGA nanoparticles do not quench fluorescence when they are dissolved in ethanol.

In addition to steady-state fluorescence, fluorescence decay also illustrates whether or not drugs attach to nanoparticles. Fluorescence decay times and amplitude of all the samples are shown in Table 6.4.

	τ_1 [ns] ± 0.2 / A [%]	τ_2 [ns] ± 0.1 / A [%]	τ_3 [ns] ± 0.1 / A [%]	τ_4 [ns] ± 0.05 / A [%]	τ_5 [ns] ± 0.02 / A [%]	χ^2
*m*THPP in ethanol	9.7 / 100	-	-	-	-	1.01
*m*THPP-PLGA in ethanol	9.6 / 100	-	-	-	-	1.04
*m*THPP-PLGA in H_2O	-	3.5 / 6.4	1.4 / 26.0	0.51 / 35.1	0.085 / 32.5	1
*m*THPC in ethanol	8.5 / 100	-	-	-	-	1.01
*m*THPC-PLGA in ethanol	8.7 / 94.0	-	0.72 / 1.5	-	0.073 / 4.5	1.04
*m*THPC-PLGA in H_2O	-	3.2 / 0.2	0.68 / 3.9	0.19 / 49.2	0.089 / 46.7	1.21

Table 6.4. Fluorescence lifetime of photosensitizer and photosensitizer-loaded PLGA nanoparticles in ethanol and in aqueous solution. λ_{exc}: 532 nm; λ_{obs}: 717 nm

The fluorescence decay of *m*THPP-PLGA nanoparticles in aqueous solution does not contain τ_1. In aqueous solution, *m*THPP molecules are trapped inside the PLGA matrix. The fluorescence lifetime of these *m*THPP molecules shortens due to different interactions, probably dye-PLGA interaction or dye-dye interaction. As can be seen from Table 6.4, *m*THPP-PLGA in ethanol exhibits similar fluorescence decay (9.6 ns) as *m*THPP in ethanol (9.7 ns). These fall within typical fluorescence lifetime for *m*THPP monomers. The fluorescence lifetime of *m*THPP-PLGA in ethanol illustrates that *m*THPP molecules are released from PLGA nanoparticles.

The fluorescence lifetime of *m*THPC-PLGA nanoparticles in ethanol is also similar to that of *m*THPC. The longest lifetime, τ_1, contributes to more than 90% of total fluorescence.

In D_2O, only very weak singlet oxygen luminescence generated from photosensitizer-loaded PLGA was observed. The singlet oxygen quantum yields of both *m*THPP- and *m*THPC-PLGA nanoparticles are very low (Table 6.3). The low singlet oxygen quantum yields as well as shortened singlet oxygen lifetimes of photosensitizer-loaded PLGA nanoparticles in D_2O are only caused by strong photosensitizer-photosensitizer interactions inside PLGA matrices. However, both *m*THPP- and *m*THPC-PLGA nanoparticles generate singlet oxygen in ethanol (87% compared to *m*THPP and 89% compared to *m*THPC). The singlet oxygen luminescence curve and exponential fitting are shown in Fig. 6.6.

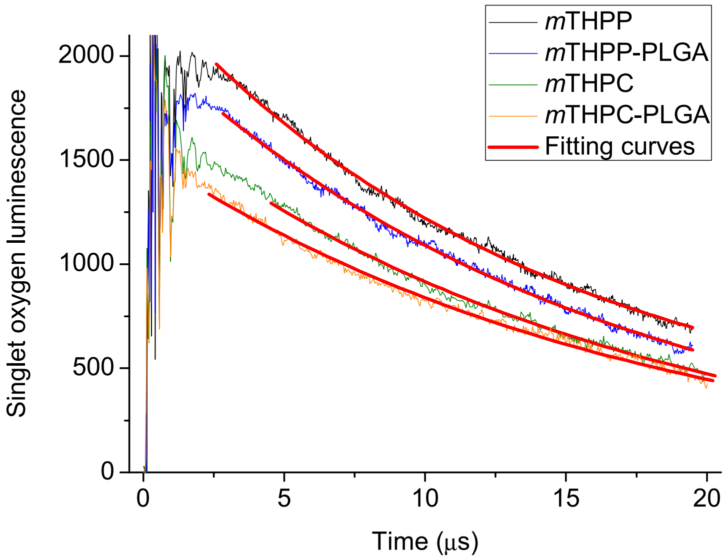

Fig. 6.6. Singlet oxygen luminescence of *m*THPP, *m*THPP-PLGA, *m*THPC, and *m*THPC-PLGA in ethanol. λ_{exc}: 512 nm for *m*THPP; λ_{exc}: 545 nm for *m*THPC; Photosensitizer Conc. 10 µM

PLGA matrices are formed via emulsion-diffusion-evaporation method. They decompose and release trapped photosensitizers when PLGA nanoparticles are dissolved in ethanol. Photosensitizers released from PLGA matrices still generate singlet oxygen. However, a question needs to be answered: whether or not PLGA matrices release photosensitizers in cell culture medium and finally in cells. The answer can be found in the next section.

6.6 PLGA matrix decomposition and drug release in Jurkat cells

Photosensitizer-loaded PLGA nanoparticles are characterized by their long triplet lifetimes. On the contrary, free photosensitizer in ethanol and in water has short triplet lifetime. Triplet lifetime of photosensitizer-loaded PLGA nanoparticles in aerobic environment is used as an indicator for PLGA decomposition and drug release since this method is fast and the result is credible.

Baier et al. [Baier et al. 2005] reported that the decay time of singlet oxygen luminescence curve in HT-29 cells changes with incubation time, and identified the decay time as singlet oxygen lifetime. This has caused difficulty in explaining their result. In fact, the rise and decay of singlet oxygen luminescence are decided by the competition of two processes: triplet state photosensitizer decay and singlet oxygen decay. The decay time of singlet oxygen luminescence will be determined by the slower process [Hackbarth 2010]. The rising time of the curve is decided by the faster process. Both times can either be singlet oxygen lifetime or triplet lifetime.

Data fitting singlet oxygen luminescence curves of *m*THPP-PLGA nanoparticles incubated with Jurkat cells results in two decay times: the shorter time between 0.5 and 1.0 μs is now considered as singlet oxygen lifetime. It coincides with the singlet oxygen lifetime of photosensitizer in cells [Hackbarth 2010]. The longer time is recognized as triplet lifetime. This lifetime changes dramatically with the incubation time. For this reason, this parameter was measured by determination of triplet-triplet absorption using laser flash photolysis in order to investigate behaviours of photosensitizer-loaded PLGA nanoparticles in different environments, including liposomes, protein solution, cell culture medium, and inside Jurkat cells. Triplet lifetimes of *m*THPP-PLGA samples under normal air condition are shown in Table 6.5.

Samples	τ_{Tair1} [µs]	Amplitude %	τ_{Tair2} [µs]	Amplitude %
*m*THPP in ethanol	0.31 ± 0.05	100	-	-
*m*THPP in 10% FCS solution	7.3 ± 0.4	100	-	-
*m*THPP in RPMI	9.2 ± 0.3	100	-	-
*m*THPP in liposomes	1.8 ± 0.2	100	-	-
*m*THPP in cells 5 h	3.0 ± 0.2	100	-	-
*m*THPP-PLGA in H_2O	-	-	70 ± 4	100
*m*THPP-PLGA in RPMI	7.9 ± 0.6	41.9	86 ± 5	58.1
*m*THPP-PLGA in cells 1 h	-	-	18 ± 3	100
*m*THPP-PLGA in cells 3 h	3.4 ± 0.3	100	-	-
*m*THPP-PLGA in cells 5 h	3.2 ± 0.2	100	-	-
*m*THPP-PLGA in cells 24 h	2.7 ± 0.2	100	-	-

Table 6.5. Triplet lifetimes of *m*THPP and *m*THPP-PLGA in different environments under normal air condition. RPMI 1640: cell culture media with FCS 10%; Liposome: DPPC; Cell line: Jurkat cells; λ_{obs}: 470 nm; λ_{exc}: 515 nm

Hydrophobic *m*THPP in ethanol under normal air conditions inhibits a very short triplet lifetime (0.31 µs), which indicates highly efficient energy transfer between triplet state photosensitizer and ground state oxygen.

*m*THPP molecules form aggregates in hydrophilic solution. For this reason, triplet lifetime of *m*THPP in water cannot be detected. However, τ_{Tair} of *m*THPP in cell culture medium RPMI 1640 containing protein Fetal Calf Serum (FCS) and in 10% FCS water solution were obtained (7.3 and 9.2 µs, respectively). These two times could be observed because *m*THPP molecules are attracted by the plasma proteins. Such photosensitizer-FCS combination behaviour has been reported by Hadjur [Hadjur 1998].

Bi-layer liposomes composed of phospholipids offer an environment in which *m*THPP behaves similarly as in cell membranes [Lasic 1997]. The triplet lifetime of *m*THPP in liposomes prepared using Dipalmitoylphosphatidylcholine (DPPC) was investigated. In this case, triplet lifetime was determined to be 1.8 µs. This is longer than τ_{Tair} in ethanol, but shorter than the τ_{Tair} of *m*THPP combined with plasma protein.

The long triplet lifetime (70 µs) of *m*THPP-PLGA in air-saturated aqueous solution indicates the low intersystem crossing quantum yield. For photosensitizer molecules encapsulated within PLGA matrices, many non-radiative deactivation processes compete with intersystem crossing. This relates to low singlet oxygen quantum yield of *m*THPP-PLGA nanoparticles.

The triplet decay of *m*THPP-PLGA in protein-containing RPMI medium contains two components that relate to two populations of *m*THPP molecules with different localizations. One is 7.9 μs, or short triplet lifetime, which is similar to τ_{Tair} of *m*THPP in FCS-containing RPMI. This lifetime is caused by *m*THPP combined with FCS. The second lifetime is 86 μs, or long triplet lifetime, which is suggested to belong to *m*THPP remaining inside the PLGA nanoparticles. This result brings important information: *m*THPP can be attracted from PLGA nanoparticles and attached to plasma protein during the drug administration via vessel injection. Other loading strategies, such as covalent conjugation, should be considered to prevent undesired releasing of drug outside tumor tissue.

Triplet photosensitizer lifetime of *m*THPP-PLGA nanoparticles in Jurkat cells indicates the intracellular decomposition of PLGA nanoparticles and drug release of *m*THPP. Inside Jurkat cells, triplet lifetime of *m*THPP after 5 h incubation is 3 μs, slightly longer than the value in liposomes.

After 1 h incubation, *m*THPP-PLGA has a triplet lifetime of 18 μs. This is much shorter than triplet lifetime of *m*THPP-PLGA nanoparticles in water (70 μs). It exhibits the immediate start of drug releasing process after intracellular drug uptake.

After 3 h and 5 h incubation, the triplet lifetime of *m*THPP-PLGA decreases to 3.4 and 3.2 μs, respectively. It exhibits the undergoing drug release of *m*THPP from PLGA inside Jurkat cells. After 5 h incubation, the triplet lifetime (3.2 μs) of *m*THPP-PLGA in Jurkat cells almost equals the value of *m*THPP (3.0 μs). After 24 h incubation, the triplet lifetime of *m*THPP-PLGA is 2.7 μs, which is nearly unchanged when compared to the result of 5 h incubation. Such rapid drug release from PLGA nanoparticles has also been reported by Zeisser-Labouebe [2006]. A parallel investigation on *m*THPC-PLGA gives a similar result (data not shown). This proves that this drug releasing mechanism is independent of photosensitizers.

6.7 Conclusions

The photophysical behaviour of photosensitizer-loaded PLGA nanoparticles indicates that photosensitizer molecules encapsulate inside PLGA matrices and also attach on the surface. *m*THPC has stronger tendency of photosensitizer-photosensitizer interaction inside PLGA matrices than *m*THPP due to higher hydrophobicity caused by double bond degeneration.

Similar to drug-loaded HSA nanoparticles, drug loading ratio is also an essential determination factor of photophysical properties and singlet oxygen generation of photosensitizer-PLGA nanoparticles. High loading ratio *m*THPP- and *m*THPC-PLGA nanoparticles generate less singlet oxygen than low loading ratio samples.

When photosensitizer-loaded PLGA nanoparticles are dissolved in ethanol, PLGA nanoparticles decompose and release photosensitizers. After the photosensitizers are released, singlet oxygen can no longer be quenched by the residues of lactic acid and glycolic acid.

Triplet lifetime of drug-carrier system offers information of drug-environment interaction, drug-nanoparticle binding, and in vitro microenvironment. Therefore, it can be utilized as an indicator for nanoparticles decomposition and drug release. Triplet lifetime of *m*THPP-PLGA nanoparticles in aqueous solution is extremely long (more than 70 µs). *m*THPP-PLGA nanoparticles in cell culture medium RPMI containing protein (FCS Albumin) have two triplet lifetimes: long time (86 µs), representing *m*THPP still entrapped in PLGA matrices, and short time (7.9 µs), relating to *m*THPP adsorbed on plasma protein. This result indicates that hydrophobic drug may have leaked out of PLGA matrices into plasma. The problem could be solved via covalent conjugation between drug molecules and PLGA matrices.

The triplet lifetime of *m*THPP-PLGA nanoparticles in Jurkat cells exhibits a decreasing tendency with incubation time. The decreasing triplet lifetime indicates undergoing PLGA nanoparticles decomposition and drug release.

7. Comparison between PLGA and HSA nanoparticles

PLGA and HSA nanoparticles are both potential biodegradable drug carriers. Hydrophobic drugs can be loaded via different strategies. Drugs are adsorbed or conjugated on the surface of HSA nanoparticles. In PLGA nanoparticles, drugs are encapsulated inside PLGA matrices. Which nanoparticle can deliver drug into tumour cells effectively and achieve rapid drug release? To answer this question, singlet oxygen generations of *m*THPP-PLGA and *m*THPP-HSA nanoparticles both in solution and in cells are compared in this chapter.

7.1 Singlet oxygen generation of *m*THPP-PLGA and *m*THPP-HSA in solution

*m*THPP is a photosensitizer with high singlet oxygen quantum yield. However, singlet oxygen generation during drug transportation can be avoided if *m*THPP is attached to large carriers such as nanoparticles. Singlet oxygen generation experiment in solution is verification whether *m*THPP attachment to PLGA and HSA NPs remarkably decrease Φ_Δ or not.

Singlet oxygen generation results of *m*THPP-PLGA and *m*THPP-HSA nanoparticles in D_2O are shown in Fig. 7.1 and Table 7.1.

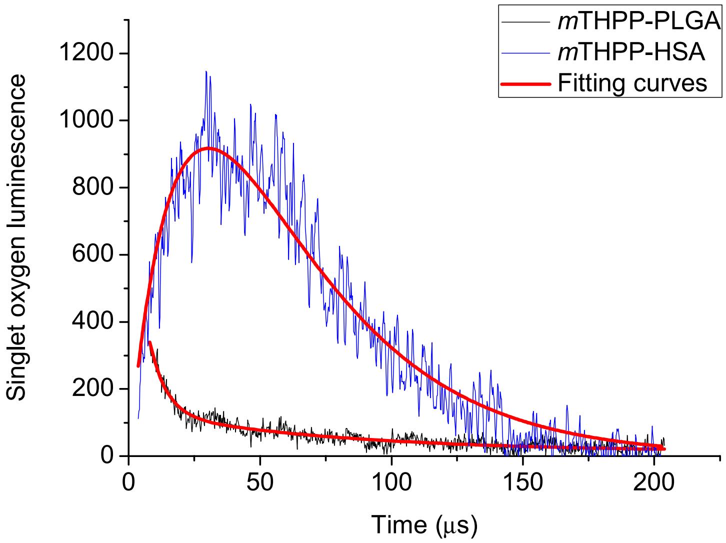

Fig. 7.1. Singlet oxygen generation of *m*THPP-PLGA and *m*THPP-HSA in D_2O, OD=0.2; excitation at 545 nm

	Φ_{fl} [1]	τ_T (μs) [2]	$\tau_{\Delta 1}$ (μs) [3]	$\tau_{\Delta 2}$ (μs) [3]	Φ_Δ [3]
*m*THPP	1	0.31 ± 0.01	-	-	0.63 ± 0.06
*m*THPP-PLGA	0.38 ± 0.01	9.5 ± 0.2	6.1 ± 0.5 (86%)	74 ± 6 (14%)	0.05 ± 0.03
*m*THPP-HSA	0.40 ± 0.01	46 ± 5	-	29 ± 7	0.07 ± 0.03

Table 7.1. PDT-correlated photophysical properties of *m*THPP-PLGA and *m*THPP-HSA nanoparticles

[1] λ_{exc}: 506 nm; fluorescence quantum yield: relates to *m*THPP

[2] Triplet lifetime was measured under normal air condition; λ_{exc}: 545 nm; λ_{obs}: 488 nm

[3] Singlet oxygen measurement: *m*THPP in ethanol, *m*THPP-PLGA, and *m*THPP-HSA in D_2O, λ_{exc}: 545 nm

From Table 7.1, *m*THPP-PLGA nanoparticles have two singlet oxygen lifetimes in D_2O. Most of singlet oxygen molecules (86%) have shortened singlet oxygen lifetime, $\tau_{\Delta 1}$ (6.1 μs), which indicates strong quenching. This lifetime is supposed to be generated by *m*THPP entrapped inside PLGA matrices. $\tau_{\Delta 2}$ is 74 μs, which means singlet oxygen without quenching. However, the part of these singlet oxygen molecules is small (14%). This relates to singlet oxygen generated from PLGA surface. *m*THPP-HSA nanoparticles have only one singlet lifetime since all *m*THPP molecules are adsorbed on the surface of HSA nanoparticles. The difference between singlet oxygen quantum yields of *m*THPP-HSA nanoparticles (0.07) and that of *m*THPP-PLGA nanoparticles (0.05) is negligible.

7.2 Behaviour of *m*THPP-PLGA and *m*THPP-HSA nanoparticles in Jurkat cells

Biodegradable PLGA nanoparticles simultaneously decompose in surface and inside the matrix. For this reason, the drug release process is rapid [von Burkersroda 2002]. In contrast, the design idea of HSA nanoparticles is to obtain stability during long-term storage. To achieve this, glutaraldehyde cross-linker is used. Could HSA quickly degrade inside targeting cells and release photosensitizers? To answer this question, intracellular singlet oxygen luminescence from PLGA and HSA NPs in Jurkat cells is measured, as shown below.

Singlet oxygen generation results of *m*THPP-PLGA and *m*THPP-HSA nanoparticles in Jurkat cells are shown in Fig. 7.2 and Table 7.2.

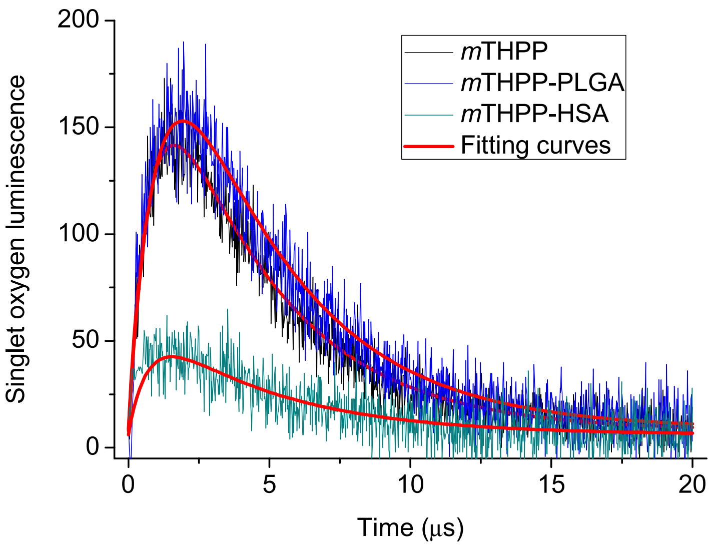

Fig. 7.1. Singlet oxygen luminescence in cells. Cell line: Jurkat cells; incubation time: 5 h; *m*THPP conc.: 3 μM; λ_{exc}: 532 nm

	τ_{Tair} (μs) [1]	τ_{Tair} (μs) ± 0.1 [2]	τ_{Δ} (μs) ± 0.05	Φ_{Δ} [3] ± 30%
*m*THPP	3.0 ± 0.1	4.0	0.80	100%
*m*THPP-PLGA	3.2 ± 0.2	4.1	1.05	114%
*m*THPP-HSA	5.9 ± 0.6	4.5	0.70	28%

Table 7.2. Singlet oxygen generation from *m*THPP, *m*THPP-PLGA and *m*THPP-HSA in Jurkat cells

[1] Triplet lifetime of photosensitizer obtained from laser flash photolysis under normal air condition

[2] Triplet lifetime of photosensitizer obtained from singlet oxygen luminescence data fitting

[3] Relates to *m*THPC in Jurkat cells

Unlike their Behaviour in solution, *m*THPP-PLGA nanoparticles generate four fold more singlet oxygen luminescence intensity inside Jurkat cells compared to *m*THPP-HSA nanoparticles after 5 h incubation. This is induced by possible two reasons. First, the intracellular decomposition rate of HSA nanoparticles is slower than PLGA nanoparticles since HSA nanoparticles are bound via covalent glutaraldehyde cross-linking. This is contrary to the fact that PLGA matrices are formed by hydrophobic/hydrophilic interaction. Second, the amount of HSA nanoparticles taken up by Jurkat cells is possibly smaller than that of PLGA nanoparticles [Preuß 2010]. Due to their faster drug release inside cells, PLGA nanoparticles should be further investigated in vivo, possibly in a clinical setting.

7.3 Conclusions

Singlet oxygen quantum yields of photosensitizer-loaded PLGA and HSA nanoparticles in solution are similar and very low. An in vitro experiment demonstrates that PLGA generates more singlet oxygen than HSA in cells after 5 h incubation. Drug encapsulation inside PLGA matrices results in faster drug release in tumour cells. PLGA NPs is superior to HSA NPs in terms of rapid drug release. However, it was proven in Chapter 6 that PLGA NPs can release the PS to serum albumins. This may hinder the usage of drug transportation by PLGA NPs in vivo.

8. PLGA- and HSA-NPs as carriers for active tumour targeting

In Chapters 5 and 6, photophysical properties as well as singlet oxygen generation in vitro of biodegradable HSA and PLGA nanoparticles for passive tumour targeting were discussed. Intracellular singlet oxygen luminescence from photosensitizer-loaded HSA nanoparticles has only 25% of the luminescence intensity when compared to free photosensitizers. This result is supported by intracellular uptake and phototoxicity [Preuß 2010].

Passive tumour targeting, such as EPR effect, functions only on tissue level. To enhance photosensitizer accumulation in single cells and achieve active tumour targeting, photosensitizer-antibody conjugation was tested [Jiang 1990]. Enhanced photosensitizer accumulation in targeting cells was reported both in vitro and in vivo experiments [Berki 1992, Gutowski 2001]. However, direct conjugation of antibody to photosensitizer reduces cutaneous phototoxicity [Van Dongen 2004]. The hydrophobicity of photosensitizer severely influences the physicochemical properties of the antibody, which changes pharmacokinetics and biodistribution [Pelegrin 1991, Vrouenraets 2000]. These problems can be avoided if photosensitizers are conjugated to antibody-modified nanoparticles. In this chapter, photosensitizer-loaded biodegradable nanoparticles designed for active tumour targeting are studied.

8.1 Covalently conjugated and antibody modified *m*THPC-HSA nanoparticles

Compared to drug adsorbed loading strategy, covalent conjugation offers a more stable drug loading during long-term storage and administration via blood vessel, as well as more controllable drug release [Kreuter 2007]. Nanoparticle surface modification with polyethylene glycol (PEG) can enhance the solubility of HSA nanoparticles in hydrophilic environment [Lin 1999]. Furthermore, HSA nanoparticles conjugated with antibodies are utilized to target certain cell types [Steinhauser 2006]. PEG shell is used to modify HSA nanoparticle surface because of its hydrophilicity and biocompatibility [Cheng 2007, Li 2007].

8.1.1 Sample description

Cetuximab-conjugated *m*THPC-HSA nanoparticles targeting the epidermal growth factor receptor (EGFR) are named CePC-HSA. IgGPC-HSA is *m*THPC-HSA nanoparticles modified by another antibody, IgG. CoPC-HSA is formed via *m*THPC covalently bound to HSA nanoparticles. The dispersion media for *m*THPC-HSA samples is distilled water.

*m*THPC-HSA nanoparticles descriptions are given in Table 8.1.

Samples	Ls	Lr [µg/mg]		
		*m*THPC	Cetuximab	IgG
CePC-HSA	Adsorptive	20.3	15.0669	-
IgGPC-HSA	Adsorptive	21.0	-	13.9573
CoPC-HSA	Covalently binding	20.6	-	-

Table 8.1. Sample description of surface modified *m*THPC-HSA nanoparticles
Ls: loading strategies; Lr: loading ratio

8.1.2 Absorption and steady-state fluorescence

To investigate the influence of antibodies and PEG modification on ground state photosensitizer molecules, absorption spectra of surface-modified *m*THPC-HSA nanoparticles were taken.

Absorption spectra of *m*THPC-HSA after scattering correction are shown in Fig. 8.1.

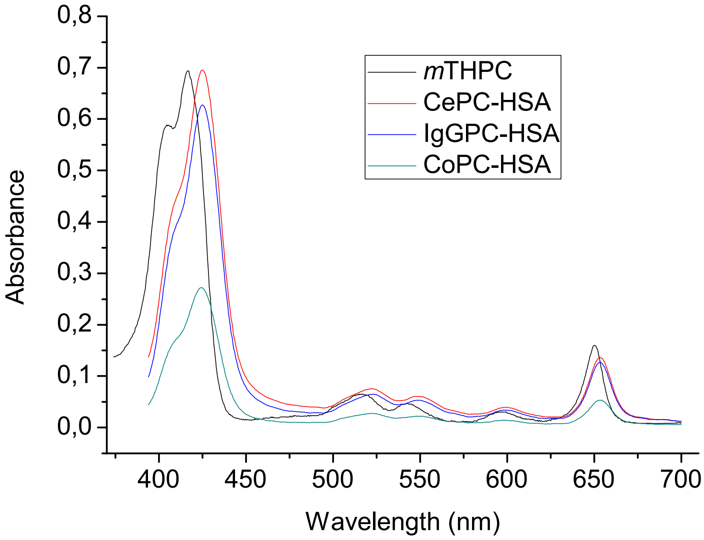

Fig. 8.1. UV-vis absorption spectra of *m*THPC in ethanol and *m*THPC-HSA in aqueous solution, scattering corrected

The Soret band maximum of CePC-HSA and IgGPC-HSA has a bathochromic shift to 425 nm compared to that of *m*THPC (417 nm). The Soret band maximum of CoPC-HSA locates at 424 nm. The absorption of CePC-HSA and IgGPC-HSA at Soret band is equal to *m*THPC, which means that antibody conjugation does not reduce the absorption of *m*THPC. The absorption extinction of CoPC-HSA, however, is only 1/3 compared to *m*THPC.

Fluorescence spectra of *m*THPC and *m*THPC-HSA are shown in Fig. 8.2.

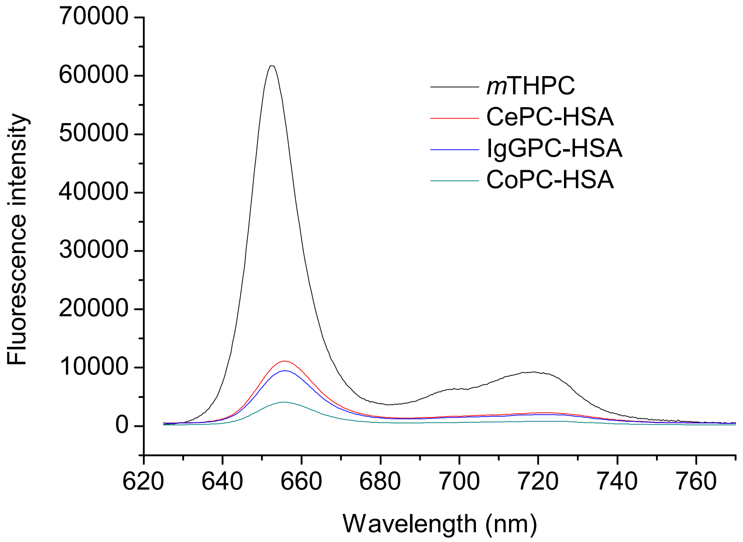

Fig. 8.2. Fluorescence spectra of *m*THPC in ethanol and *m*THPC-HSA in aqueous solution. λ_{exc}: 506 nm

The fluorescence maximum of the $S_{1,0} \rightarrow S_{0,0}$ in *m*THPC-HSA shifts to 657 nm compared to 654 nm of *m*THPC. The fluorescence quantum yields of CePC-HSA and IgGPC-HSA are approximately 24.9% and 21.4% compared with *m*THPC, respectively. The differences of Φ_{FL} between CePC-HSA and IgGPC-HSA are negligible. The Φ_{FL} of CoPC-HSA is much lower when compared to other samples.

8.1.3 Fluorescence kinetic parameters

The differences between absorption and steady-state fluorescence of Cetuximab- and IgG-loaded *m*THPC-HSA NPs are negligible. The strong reduction of the fluorescence quantum yield is a proof of an interaction between *m*THPC molecules and surrounding substances. Fluorescence lifetimes determined with TCSPC should help further clarify this issue.

Fluorescence lifetimes and their amplitudes of *m*THPC in ethanol and *m*THPC-HSA in aqueous solutions are shown in Table 8.2.

	Φ_{FL}[a]	τ_1 (ns) ± 0.1 / A [%]	τ_2 (ns) ± 0.1 / A [%]	τ_3 (ns) ± 0.05 / A [%]	$\chi2$
CePC-HSA	24.9%	3.9 / [23.0]	1.5 / [45.5]	0.30 / [31.5]	1.09
IgGPC-HSA	21.4%	3.6 / [19.8]	1.4 / [44.8]	0.29 / [35.4]	0.96
CoPC-HSA	9.3%	3.3 / [22.9]	1.3 / [43.4]	0.26 / [33.7]	1.09

Table 8.2. Fluorescence lifetime of *m*THPC-HSA nanoparticles in H_2O; λ_{exc}: 532 nm; λ_{obs}: 650 nm; Φ_{FL}: fluorescence quantum yield. [a]: Standard: *m*THPC in ethanol; *m*THPC conc. 3 μM

The fluorescence lifetime of *m*THPC monomers in ethanol is 8.5 ns. The fluorescence spectra of *m*THPC-HSA adsorptive nanoparticles consist of three fluorescence lifetime species. All three samples have similar fluorescence lifetimes with the same amplitudes. This means that antibody modification and covalent conjugation do not change the fluorescence lifetime of *m*THPC-HSA nanoparticles. The dominant interaction mechanism of antibody-modified *m*THPC-HSA NPs remains between *m*THPC and HSA in spite of additional antibody conjugation.

8.1.4 Singlet oxygen generation and laser flash photolysis

The results above show that antibody modification has no influence on PS in ground state and excited singlet state. The information about antibodies interaction with singlet oxygen, however, is still missing. Singlet oxygen luminescence determination together with laser flash photolysis is conducted in order to investigate singlet oxygen generation of antibody-modified *m*THPC-HSA NPs in solution.

Singlet oxygen and triplet lifetimes of *m*THPC-HSA in D_2O are shown in Table 8.3.

	τ_{Tair} [μs]	τ_{TN2} [μs]	f_{ET}	τ_Δ [μs]	Φ_Δ (±0.02)
CePC-HSA	35 ± 3	98 ± 7	0.64	8 ± 1	0.09
IgGPC-HSA	36 ± 3	103 ± 8	0.65	7 ± 1	0.08
CoPC-HSA	29 ± 3	103 ± 8	0.72	6 ± 1	0.08

Table 8.3. PDT-relevant photophysical parameters of *m*THPC-HSA samples: triplet lifetime under normal condition τ_{Tair}, Singlet oxygen lifetime (τ_Δ), and quantum yield (Φ_Δ)

[a]All samples were excited at 652 nm in singlet oxygen measurement. TPPS in D_2O is taken as

the singlet oxygen quantum yield standard ($\Phi_\Delta = 0.70$).

The triplet lifetime under normal air condition τ_{Tair} is mainly determined by cross-linkage and independent of drug loading ratios or antibody modification. The samples CePC-HSA and IgGPC-HSA share the same value of τ_{Tair} with *m*THPC-loaded 100% cross-linked HSA NPs without any modification (Chapter 5). However, covalently conjugated sample CoPC-HSA has shorter τ_{Tair} than drug adsorbed samples, which indicates a different microenvironment caused by loading strategy. The singlet oxygen lifetime τ_Δ of the three samples is much shorter when compared with unmodified *m*THPC-HSA nanoparticles (Chapter 5). This means that strong quenching of singlet oxygen caused by antibody modification and covalent conjugation occurs.

8.1.5 Singlet oxygen luminescence detection in cells

Unmodified *m*THPC-HSA nanoparticles generate tiny amounts of singlet oxygen in cells after 5 h incubation (Chapter 5), which makes HSA nanoparticles unsuitable as rapid drug deliver carriers. Will surface modified *m*THPC-HSA nanoparticles perform better? To investigate this, Jurkat and HT-29 cells were incubated for 5 h with 3 μM *m*THPC and *m*THPC-HSA nanoparticles in darkness, respectively. The singlet oxygen luminescence of photosensitizers located inside Jurkat and HT-29 cells was determined with the equipment described in Chapter 3. Data of intracellular singlet oxygen luminescence of *m*THPC-HSA in Jurkat cells and HT-29 cells are shown in Table 8.4.

	Jurkat cells		
	τ_Δ [μs] ± 0.05	τ_T [μs] ± 0.1	$I_\Delta{}^a$ ± 30%
*m*THPC	0.65	3.6	100%
CoPC-HSA	0.40	3.8	48%
CePC-HSA	0.45	3.7	56%
PEGPC-HSA	0.50	2.8	99%
	HT-29 cells		
*m*THPC	0.55	2.8	100%
CoPC-HSA	0.45	3.1	25%
CePC-HSA	0.45	2.7	76%
PEGPC-HSA	0.40	2.7	84%

Table 8.4. Singlet oxygen lifetime and triplet decay of *m*THPC and *m*THPC-HSA in cells after 5 h incubation; *m*THPC Conc. 3 μM; cell number: 5×10^5 cells/ml; illumination time: 20

s; λ_{exc}: 652 nm; laser power: 1.5 mW
[a]Relates to *m*THPC in Jurkat cells
[b]Relates to *m*THPC in HT-29 cells

All *m*THPC-HSA nanoparticles generated singlet oxygen in both two types of cell lines after 5 h incubation. For CoPC-HSA without any modification, the luminescence intensity is less than 50% compared to *m*THPC in Jurkat cells. In HT-29 cells, this value is only 25% of *m*THPC. The singlet oxygen luminescence intensity of CePC-HSA is three fold compared to CoPC-HSA (76% to 25%) in HT-29 cells. This may become evidence of EGFR targeting by monoclonal antibody Cetuximab. The Jurkat cells have no EGFR. Thus, no targeting effect was observed. However, better intracellular uptake enhancement against antibody modification can be obtained when PEG modification is used. The singlet oxygen luminescence intensity of PEGPC-HSA generated in Jurkat cells is equal to the value of *m*THPC. The enhanced intracellular singlet oxygen generation induced by PEG modification is independent on cell line. In HT-29 cells, intensity of singlet oxygen luminescence also achieves a high level (84%) compared to *m*THPC.

8.2 Investigation on *m*THPC-PLGA nanoparticles modified with antibodies

In Chapter 6, the comparison of photosensitizer-loaded PLGA and HSA nanoparticles showed that unmodified PLGA nanoparticles perform well in transporting drugs into cells and rapidly releasing them.

In the last section, photophysical properties of surface-modified HSA nanoparticles, as well as their capabilities of intracellular singlet oxygen generation, were investigated. Antibody and PEG modification were proved to be efficient, especially for HSA nanoparticles accumulation in HT-29 cells. In this section, the photophysical properties and intracellular singlet oxygen generation of surface-modified *m*THPC-PLGA nanoparticles are compared to examine if surface modification also enhances singlet oxygen generation in targeting cells.

8.2.1 Sample description

*m*THPC-PLGA nanoparticles were prepared with standard emulsion-diffusion-evaporation method mentioned before. ErbPC-PLGA was modified with antibodies Erbitux. IgGPC-PLGA was modified with antibodies human IgG as control sample. mPEGPC-PLGA contained surface-adsorbed antibodies Erbitux and modified with mPEG shell.

Samples	Lr (µg/mg)		
	*m*THPC	Erbitux	IgG
*m*THPC-PLGA	64.150	-	-
ErbPC-PLGA	52.806	2.517	-
IgGPC-PLGA	49.144	-	2.886
mPEGPC-PLGA	54.331	0.2093	-

Table 8.5. Description to *m*THPC-PLGA nanoparticles. Lr: loading ratio

8.2.2 Absorption and steady-state fluorescence

The absorption spectra of *m*THPC in ethanol and *m*THPC-PLGA in aqueous solution are shown in Fig. 8.3.

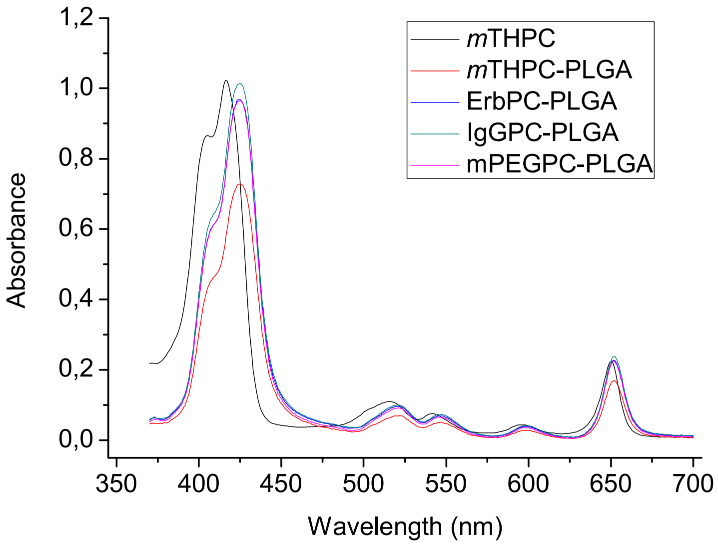

Fig. 8.3. UV-vis absorption spectra of *m*THPC in ethanol and *m*THPC-PLGA nanoparticles in aqueous environment. *m*THPC Conc. 4 µM. The absorption spectra of *m*THPC-PLGA are shown after scattering correction.

The Soret band maxima of all *m*THPC-PLGA samples show a bathochromic shift compared to *m*THPC spectrum. The Soret band maximum of *m*THPC in ethanol locates at 417 nm. The Soret band maxima of four *m*THPC-PLGA samples are shifted to 425 nm. The strongest Q band of *m*THPC absorption spectrum locates at 650 nm. Its counterpart of *m*THPC-PLGA shifts to 652 nm. Surface modification causes no additional change to absorption *m*THPC-PLGA nanoparticles.

The steady-state fluorescence of *m*THPC and *m*THPC-PLGA was excited at 506 nm. Fluorescence spectra of *m*THPC and *m*THPC-PLGA are shown in Fig. 8.4.

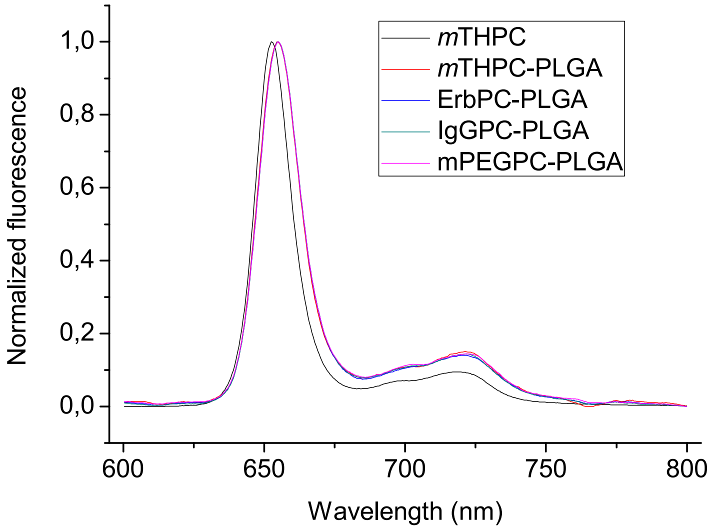

Fig. 8.4. Steady-state fluorescence of *m*THPC and *m*THPC-PLGA; λ_{exc}: 506 nm, data normalized

The fluorescence peak of *m*THPC locates at 652.5 nm. The fluorescence peaks of four *m*THPC-PLGA samples are at 654.5 nm. The relative fluorescence quantum yields of *m*THPC-PLGA nanoparticles (compared to *m*THPC) are shown in Table 8.6.

8.2.3 Fluorescence kinetic parameters

Fluorescence decay times and their amplitudes are shown in Table 8.6.

	Φ_{FL} [a]	τ_1 [ns] ± 0.05/A [%]	τ_2 [ns] ± 0.02/A [%]	χ^2
*m*THPC-PLGA	3.5%	0.31/15.6	0.12/84.5	1.3
ErbPC-PLGA	5.3%	0.35/12.9	0.14/87.1	0.94
IgGPC-PLGA	5.2%	0.38/11.1	0.15/88.9	1.01
mPEGPC-PLGA	5.0%	0.35/17.0	0.14/83.0	0.96

Table 8.6. Fluorescence lifetime of *m*THPC-PLGA in aqueous solution

[a] Φ_{FL} Fluorescence quantum yield relative to *m*THPC. λ_{exc}: 532 nm; λ_{obs}: 650 nm

The total fluorescence signal of all *m*THPC-PLGA samples consists of two lifetimes. Both the lifetimes and their amplitudes are very similar. The fluorescence lifetime result, as well as absorption and steady-state fluorescence, exhibit that surface modification does not influence the photophysical properties of *m*THPC-PLGA nanoparticles.

8.2.4 Singlet oxygen generation and laser flash photolysis

Singlet oxygen and triplet lifetime results of *m*THPC-PLGA nanoparticles are shown in Table 8.7.

	τ_Δ (μs)	τ_{Tair} (μs)	Φ_Δ (μs) ± 0.03
*m*THPC-PLGA	5.0 ± 0.5	59 ± 2	0.03
ErbPC-PLGA	13 ± 1	77 ± 3	0.04
IgGPC-PLGA	5.5 ± 0.5	87 ± 4	0.04
mPEGPC-PLGA	6.0 ± 0.5	79 ± 4	0.05

Table 8.7. Singlet oxygen lifetime τ_Δ, singlet oxygen quantum yield Φ_Δ and triplet lifetime τ_{Tair} of *m*THPC-PLGA samples. Solvent: D_2O; λ_{exc}: 545 nm. Rose Bengal in D_2O is taken as the singlet oxygen quantum yield standard ($\Phi_\Delta = 0.75$). Triplet lifetime: λ_{exc}: 652 nm; λ_{obs}: 470 nm

*m*THPC-PLGA samples generate very small amounts of singlet oxygen in solution. The shortened singlet oxygen lifetime indicates that singlet oxygen generated from *m*THPC-PLGA is strongly quenched. The triplet state quenching rate constant k_q of *m*THPC-PLGA is in the order of 10^9 $M^{-1}s^{-1}$. This illustrates that the energy transfer between triplet state photosensitizer and molecular oxygen is inefficient. The triplet lifetimes of surface-modified *m*THPC-PLGA are even longer than the unmodified sample. The reason should be the reduced exposure of triplet state *m*THPC to solvent caused by additional PEG shell and antibodies [Lang 2004].

8.2.5 Singlet oxygen luminescence in HT-29 cells

Singlet oxygen luminescence generated by *m*THPC and *m*THPC-PLGA nanoparticles in HT-29 cells was investigated. Results are shown in Table 8.8.

	τ_Δ [µs] ± 0.05	τ_{Tair} [µs] ± 0.1	$I_\Delta{}^a$ ± 30%
*m*THPC	0.75	3.8	100%
*m*THPC-PLGA	0.65	3.1	106%
ErbPC-PLGA	0.60	3.5	76%
IgGPC-PLGA	0.55	3.3	87%
mPEGPC-PLGA	0.60	2.8	69%

Table 8.8. Singlet oxygen generation of *m*THPC and *m*THPC-PLGA in HT-29 cells. Incubation time: 5 h; *m*THPC Conc. 3 µM; cell number: 5×10^5 cells/ml; illumination time: 20 s; λ_{exc}: 652 nm; laser power: 1.5 mW

[a] *m*THPC in HT-29 cells was taken as standard

Unmodified *m*THPC-PLGA has the same value of singlet oxygen luminescence with *m*THPC in HT-29 cells after 5 h incubation. *m*THPC-PLGA nanoparticles modified with antibodies, as well as mPEG modified *m*THPC-PLGA nanoparticles, show less singlet oxygen luminescence. Surface modification of PLGA nanoparticles exhibits no enhanced targeting effect to HT-29 cells containing EGFR receptors. This result illustrates that it is unnecessary to make surface modification to *m*THPC-PLGA nanoparticles to enhance targeting effect since unmodified *m*THPC-PLGA nanoparticles are well taken up by HT-29 cells with enough singlet oxygen generation inside cells.

8.3 Conclusions

Intracellular singlet oxygen experiments exhibit that Cetuximab-modified *m*THPC-HSA NPs produces more singlet oxygen inside HT-29 cells when compared to unmodified *m*THPC-HSA NPs. Cetuximab modification showed enhanced targeting effect on HT-29 cells containing EGFR factor in vitro. Besides antibody modification, PEGylated *m*THPC-HSA nanoparticles exhibit enhanced uptake in both Jurkat and HT-29 cell lines. The enhanced intracellular singlet oxygen generation of PEGylated sample is probably caused by higher molecular weight, which leads more efficient endocytosis. PEG surface modification can be used alone to promote passive tumour targeting. Nevertheless, one should consider that this result is obtained only in the level of in vitro.

The relative intensity of intracellular singlet oxygen luminescence of unmodified *m*THPC-PLGA nanoparticles is similar to that of *m*THPC. However, the luminescence intensity of the three antibody-loaded *m*THPC-PLGA samples is less than *m*THPC and unmodified *m*THPC-PLGA nanoparticles. The drug releasing mechnism of PLGA nanoparticles is drug diffusion through the polymer matrix [Mu 2003]. Surface modification may block the diffusion pathway. No benefit is evident from surface modifications of *m*THPC-PLGA nanoparticles.

9. Summary / Zusammenfassung

The main goal of this PhD thesis is the photophysical investigation of biodegradable photosensitizer-nanoparticle carrier systems achieving passive and active tumour targeting strategies. For this purpose both steady state and time-resolved spectroscopic methods accompanied by data analysis were utilized. Especially time-resolved singlet oxygen luminescence generated from photosensitizer-loaded nanoparticles was detected both in solution and in vitro.

Until now no publication was found that entirely investigates the influence of drug loading ratio on photophysical properties of photosensitizer-loaded nanoparticles and their intracellular singlet oxygen luminescence as well. The cross-linking of HSA NPs also needs to be evaluated in terms of photophysical characterization and singlet oxygen generation determination.

This work contains three main parts:

First the photophysical properties of Pheo-HSA nanoparticles were compared to free pheophorbide a. Steady-state and time-resolved fluorescence experiments have already proved that the interaction between pheophorbide a and HSA nanoparticles is strong. This interaction leads to low singlet oxygen quantum yield (0.07) in D_2O compared to free Pheo (0.52) in ethanol. But when incubated in Jurkat and HT-29 cell lines, Pheo-HSA nanoparticles have been proved to generate singlet oxygen inside cells. This result coincides with intracellular uptake and phototoxicity experiments carried out by Preuß [Chen et al 2009]. They all reveal the capability of HSA nanoparticles to carry photosensitizers into tumour cells.

In the second part the well-known photosensitizers *m*THPP and *m*THPC were loaded to HSA- and PLGA- nanoparticles. It was found that the loading ratio determines the photophysical properties of both photosensitizer-loaded HSA and PLGA nanoparticles. For HSA nanoparticles, photosensitizer-nanoparticle interaction is the preferential mechanism in low loading ratio sample. But in high loading ratio sample, photosensitizer-photosensitizer interaction becomes the determining interaction. This interaction prevents singlet oxygen generation from high loading sample. For PLGA nanoparticles, high drug loading ratio also leads to a strong singlet oxygen quenching. At high drug loading ratio PLGA nanoparticles, some photosensitizer molecules may be localized deeply inside PLGA matrices and far away from surface. This induces a slower drug release since drug will diffuse through the polymer matrix during the release process [Mu 2003].

Controllable drug release in tumour cells can be achieved by adjusting the amount of cross-linking of HSA nanoparticles. 40% and 100% cross-linking HSA nanoparticles release drug in tumour cells faster than 200% cross-linking sample. The latter needs more than 24 h to decompose therefore it is not useful for rapid drug delivery.

Pharmaceutical industry requires confirmed quantified drug loading parameters. Based on the loading ratio and cross-linking results of drug-loaded HSA NPs above, a comparable and repeatable preparation of *m*THPC-HSA nanoparticles was fixed to be: 20 µg / mg, 100% cross-linking.

Compared to covalently conjugated HSA nanoparticles, PLGA nanoparticles decompose much faster since they are formed via hydrophobic / hydrophilic interaction. However, it brings another problem that photosensitizers encapsulated inside PLGA nanoparticles can be attracted by protein in cell cultural media before they are transported to targeting cells. For this reason, further in vivo evaluation of drug-loaded PLGA NPs is needed.

The singlet oxygen quantum yields of photosensitizer-loaded PLGA and HSA nanoparticles in solution are negligible. For short period incubation (5 h), PLGA nanoparticles show 4 folds higher singlet oxygen luminescence than HSA nanoparticles. It is supposed that PLGA nanoparticles should be more hopeful carriers in terms of rapid drug release if photosensitizer can be covalently conjugated to PLGA matrices.

In the third part of this work, active tumour targeting behaviour achieved by surface modification of HSA and PLGA nanoparticles has been tested. Intracellular singlet oxygen measurement reveals that HSA nanoparticles, both with antibody and PEG surface modification have an enhanced targeting of tumour cells in vitro.

On the contrary, such surface modifications of PLGA NPs result in reduced singlet oxygen generation in HT-29 cells. The reason is the blocking of drug diffusion pathway out of PLGA matrices by surface substituents.

Another problem of antibody conjugation is to quantify the antibody number per nanoparticle. Moreover the use of antibodies as surface modification of nanoparticles for active targeting should be cautious when considering the limited impact and high costs.

Further research on this issue should be oriented to several directions as follow:

First of all, intracellular singlet oxygen detection can be used together with confocal laser scanning microscopy technique. Secondly, in vivo PDT experiments with photosensitizer-nanoparticle carrier system should be carried out based on the deep-going in vitro singlet oxygen determination. All in vitro and in vivo singlet oxygen results will feedback to promote the optimization of the preparation of photosensitizer-loaded nanoparticles. Finally, the stability of drug-loaded nanoparticles should be traced in a long-term period before clinical testing.

Ziel der vorliegenden Arbeit ist die photophysikalische Untersuchung biodegradierbarer Photosensibilisator- beladener Nanopartikel als Transportsysteme für aktives und passives Tumor-Targeting. Zu diesem Zweck wurden sowohl stationäre, als auch zeitaufgelöste spektroskopische Methoden angewand. Speziell der durch mit Photosensibilisatoren beladenen Nanopartikeln generierte Singulettsauerstoff wurde mittels zeitaufgelöster Singulettsauerstofflumineszenz sowohl in Lösung als auch in vitro nachgewiesen.

Bisher sind keine Veröffendlichungen zum Einfluss der Beladungsrate auf die photophysikalischen Eigenschaften von Photosensibilisator-beladenen Nanopartikeln und auf deren intrazelluläre Singulettsauerstofflumineszenz bekannt.

Eine wichtige Untersuchung ist auch die des Einflusses der Quervernetzung von HSA-Nanopartikel auf deren photophysikalische Eigenschaften speziell auf die Fähigkeit Singulettsauerstoff zu generieren.

Diese Arbeit besteht aus 3 Teilen:

Der erste Teil beschäftigt sich mit der photophysikalischen Charakterisierung von Pheo-HSA-Nanopartikeln. Diese Untersuchungen wurden im Vergleich mit ungebundenen Phäophorbid a durchgeführt.

Mittels stationärer und zeitaufgelöster Messungen konnte gezeigt werden, dass die Wechselwirkungen zwischen Phäophorbid a und den HSA-Nanopartikeln sehr stark ist.

Diese Wechselwirkungen bewirken eine geringe Singulettsauerstoffquantenausbeute (0,07) in D_2O verglichen mit dem von Phäophorbid a in Ethanol (0,52).

Im Gegensatz dazu konnte nach der Inkubation in Jurkat- und HT-29-Zellen eine intrazelluläre Singulettsauerstoffgenerierung der Pheo-HSA-Nanopartikel nachgewiesen werden.

Dieses Ergebnis wird auch durch Experimente zur intrazellulären Akkumulation und zur Phototoxizitäts, durchgeführt von A. Preuß [Chen et al 2009], bestätigt. Als Ergebnis der durchgeführten Untersuchungen kann die Schlussfolgerung gezogen werden, dass sich HSA-Nanopartikel sehr gut als Carrier für den Transport von

Photosensibilisatoren in Tumorzellen eignen.

Im zweiten Teil wurden mit den Photosensibilisatoren *m*THPP and *m*THPC beladene HSA- und PLGA-Nanopartikel untersucht.

Es konnte gezeigt werden, dass die Photosensibilisator-Beladungsrate die photophysikalischen Eigenschaften der HSA- und PLGA-Nanopartikel stark beeinflusst.

Für die HSA-Nanopartikel dominieren bei geringen Beladungsraten die Wechselwirkungen zwischen HSA und den Photosensibilisatormolekülen. Mit steigender Photosensibilisator-Beladung spielen Wechselwirkungen zwischen den Photosensibilisatormolekülen eine zunehmende Rolle. Diese Wechselwirkungen verringern bei hoher Beladung der HSA-Nanopartikel die Generierung von Singulettsauerstoff.

Die Geschwindigkeit der Freisetzung der Photosensibilisatoren kann mittels des Vernetzungsgrads der HSA-Monomere in den HSA-Nanopartikeln reguliert werden. 40% und 100% vernetzte HSA-Nanopartikel entlassen die Wirkstoffe in Tumorzellen deutlich schneller als 200% vernetzte HSA-Nanopartikel. Letztere benötigen mehr als 24 h um ihre Wirkstoffe freizusetzen, was für die klinische Verwendung nicht sinnvoll ist.

Die pharmazeutische Industrie benötigt quantifizierte Baladungsparameter für Transportsystem wie Nanopartikel. Aufgrund der Ergebnisse bezüglich der Beladungsrate und Vernetzung der HSA-Nanopartikel konnte eine reproduzierbare Präparationsmethode entwickelt werden, zur Herstellung von HSA-Nanoparikeln, mit einer Beladungsrate von 20 µg / mg und einer HSA-Vernetzung von 100%.

Auch für die PLGA-Nanopartikel konnte mit zunehmender Beladung ein verstärktes Singulettsauerstoffquenching nachgewiesen werden.

Für stark beladene PLGA-Nanopartikel können die Photosensibilisatormoleküle nicht nur auf der Oberfläche sondern auch im inneren der Partikel lokalisiert sein. Diese Lokalisierung bewirkt eine Verzögerung der Freisetzung der Photosensibilisatoren durch Diffusionsprozesse in den Nanopartikeln [Mu 2003].

Im Vergleich zu den kovalent verknüpften HSA-Nanopartikeln werden die durch hydrophobe und hydrophile Wechselwirkungen geformten PLGA-Nanopartikel deutlich schneller abgebaut.

Jedoch besteht bei den PLGA-Nanopartikeln das die gebundenen Photosensibilisatoren eine starke Affinität zu den im Zellkulturmedium befindlichen Proteinen aufweisen. Dies könnte zur vorzeitigen Freisetzung der Photosensibilisatoren bei systemischer Verabreichung im Organismus führen. Daher wäre eine in vivo Untersuchung der Photosensibilisator –beladenen PLGA-Nanopartikel nötig.

Die Singulettsauerstoffquantenausbeute der Photosensibilisator beladenen PLGA-Nanopartikel in Lösung ist wie auch schon für die HSA-Nanopartikel sehr gering.

Nach kurzen Inkubationszeiten (5 h) in Zellen zeigen die PLGA-Nanopartikel eine 4fach höhere Singulettsauerstoffluniniszenz als die HSA-Nanopartikel.

Das Potenzial der PLGA-Partikel als Wirkstofftransporter in der Photodynamischen Therapie könnte deutlich gesteigert werden, wenn es zukünftig gelingt die Photosensibilisatoren kovalent an die PLGA-Matrix zu binden, um eine vorzeitige Freisetzung zu verhindern

Im dritten Teil dieser Arbeit wurden, für aktives Targeting von Tumorzellen, Oberflächenmodifizierte PLGA- und HSA-Nanopartikel untersucht.

Die intrazellulären Singulettsauerstoffmessungen weisen auf eine erleichterte Aufnahmein Tumorzellen von Antikörper- und PEG-modifizierten HSA-Nanopartikeln in vitro hin.

Im Gegensatz dazu bewirkt solche Oberflächenmodifizierung bei PLGA-Nanopartikeln eine geringere Singulettsauerstoffgenerierung in HT-29-Zellen. Grund dafür ist die Blockierung der Diffusion der Wirkstoffe aus der PLGA-Matrix durch die Oberflächensubstituenten.

Ein weiteres Problem der Antikörperkonjugation ist die Quantifizierung der Antikörpermenge je Nanopartikel.

Die Verwendung von Antikörpern als Oberflächenmodifizierung der Nanopartikel für aktives Targeting scheint sehr fraglich bezüglich des geringen Effekts und der damit verbundenen hohen Kosten.

Zukünftige Arbeiten zu diesem Thema solten in unterschiedlicher Richtung erfolgen:

Als erstes sollte die Singulettsauerstoffdetektion mit der Konfokalen Laserscanning Mikroskopie kombiniert werden;

Weiterhin sollten in vivo PDT Experimente mit den Photosensibilisator-beladenen Nanopartikeln, basierend auf den umfangreichen in vitro Singulettsauerstoff-Untersuchungen angestrebt werden.

Alle in vitro und in vivo Singulettsauerstoff-Untersuchungen können zur Optimierung der Präparation Photosensibilisator-beladener Nanopartikel beitragen.

Letztendlich sollte in Langzeitstudien die Stabilistät der Wirkstoff-beladenen Nanopartikel überprüft werden befor sie klinisch getestet werden können.

Reference

Allemann E., Leroux, J. C., Gurny, R. and Doelker, E. (**1993**). *In vitro* extended-release properties of drug-loaded poly(D,L-lactic acid) nanoparticles produced by a salting-out procedure. *Pharmaceutical Research* 10, 1732–1737.

Allemann, E., Brasseur, N., Kundrevich, S. V., La madeleine, C., and Van Lier, J. E. (**1997**) Photodynamic activities and biodistribution of fluorinated zinc phthalocyanine derivatives in the murine EMT-6 tumour model. *Int. J. Cancer.*, 72: 289-294.

Anhorn, M. G., Wagner, S., Kreuter, J., Langer, K., and von Briesen, H. (**2008**) Specific Targeting of HER2 Overexpressing Breast Cancer Cells with Doxorubicin-Loaded Trastuzumab-Modified Human Serum Albumin Nanoparticles. *Bioconjugate Chem.*, *19,* 2321–2331.

Baier J, Maier M, Engl R, Landthaler M, Bäumler W (**2005**) Time-Resolved Investigations of Singlet Oxygen Luminescence in Water, in Phosphatidylcholine, and in Aqueous Suspensions of Phosphatidylcholine or HT29 Cells. *J. Phys. Chem. B* 109:3041-3046.

Baker, A. and Kanofsky, J. R. (**1992**) Quenching of singlet oxygen by biomolecules from L1210 leukemia cells. *Photochem.Photobiol.* 55, 523–528.

Balchum, O.J., Doiron, D.J. (**1985**). Photoradiation Therapy of Endobronchial Lung Cancer. *Clin. Chest. Med.*, 6, 255-275.

Ball R. H., Dorough, G. D., Calvin, M. (**1946**) Further study of the porphine-like products of the reaction of benzaldehyde and pyrrole. *J. Am. Chem. Soc.,* 68, 2278-2281.

Barber, P., Barr, H., George, J., et al. (**2002**) Photodynamic therapy in the treatment of lung and oesophageal cancers. *Clin Oncol (R Coll Radiol)*, 14: 110–116.

Barnett, A.A., Haller, J.C., Cairnduff, F., et al. (**2003**) A randomised, doubleblind, placebo-controlled trial of photodynamic therapy using 5-aminolaevulinic acid for the treatment of cervical intraepithelial neoplasia. *Int. J. Cancer*, 103**:** 829–32.

Becker, W. (**2005**) Advanced time-correlated single-photon counting techniques. Springer, Berlin, Heidelberg, New York.

Bellnier, D. A.; Greco, W. R.; Loewen, G. M.; Nava, H.; Oseroff, A. R.; Pandey, R. K.; Tsuchida, T.; Dougherty, T. J. (**2003**) Population pharmacokinetics of the photodynamic therapy agent 2-(1-hexyloxyehyl)-2-devinyl pyropheophorbide-a in cancer patients. *Cancer Res.*, 63: 1806-1813.

Bellocq, N.C., Pun, S.H., Jensen, G.S., Davis, M.E. (**2003**) Transferrin-containing, cyclodextrin polymer-based particles for tumor-targeted gene delivery. *Bioconj. Chem.,* 14, 1122–1132.

Bensasson, R.V., Land, E. J., and Truscott, T. G.. (**1993**) Excited States and Free Radicals in Biology and Medicine., (Oxford: Oxford Univ. Press).

Berenbaum, M. C., Akande, S. L., Bonnett, R., Kaur, H., Ioannou, S., White, R. D. and Winfield, U. J. (**1986**) Meso-Tetra(Hydroxyphenyl)Porphyrines, a New Class of Potent Tumour Photosensitisers with Favourable Selectivity. *Br. J. Cancer*, 54: 717-725.

Berenbaum, M. C. (**1989**) *Biochem. J.*, *261,277,*

Berenbaum, M. C.; (**1993**) Bonnett, R.; Chevretton, E. B.; Akande-Adebakin, S. L.; Ruston, M. *Lasers Med. ScL*, 8, 235.

Berki, T., Nemeth, P. (**1992**) Photo-immunotargeting with haematoporphyrin conjugates activated by a low power He–Ne laser, *Cancer Immunol. Immunother.* 35 69–74.

Bonnett, R.; Kaur, H.; loannou, S.; White, R.. D.; Winfield, U.-J. (**1986**) *Br. J. Cancer*, *54,* 717.

Bilski, P.; Kukielczak, B. M.; Chignell, C. F. (**1998**) *Photochem. Photobiol.*, *68*, 675.

Biolo, R., Jori, G.,Soncin, M., Rihter, B., Kenney, M. E., Rodgers, M. A. (**1996**) Effect of photosensitizer delivery system and irradiation parameters on the efficiency of photodynamic therapy of B16 pigmented melanoma in mice. *Photochem. Photobiol.*, 63: 224-228.

Birnbaum, D. T., Kosmala, J. D., and Brannon-Peppas, L. (**2000**) Optimization of preparation techniques for poly(lactic acid-co-glycolic acid) nanoparticles. *Journal of Nanoparticle Research* 2: 173–181.

Bivas-Benita, M., Romeijn, S. Junginger, H. E., Borchard, G. (**2004**) PLGA–PEI nanoparticles for gene delivery to pulmonary epithelium. European Journal of Pharmaceutics and Biopharmaceutics 58 1–6.

Bozkir, A, Saka, O. M. (**2005**) Formulation and investigation of 5-FU nanoparticles with factorial design-based studies. *Il Farmaco* 60 840–846.

Brigger, I., Dubernet, C., Couvreur, P. (**2002**) Nanoparticles in cancer therapy and diagnosis. *Advanced Drug Delivery Reviews* 54 631–651.

Brokx, RD, Bisland, SK, Gariepy, J. (**2002**) Designing peptide-based scaffolds as drug delivery vehicles. *J Control Release*; 78: 115–23.

Brown, S. B., Brown, E. A., Walker, I. (**2004**) The present and future role of photodynamic therapy in cancer treatment. *Lancet. Oncol.*, 5: 497–508.

Carter, D. C.; Ho, J. X. (**1994**) *Adv Protein Chem*, 45, 153–203.

Cascone, M. G., Pot, P. M., Lazzeri, L., Zhu, Z. H. (**2002**) Release of dexamethasone from PLGA nanoparticles entrapped into dextran/poly(vinyl alcohol) hydrogels. *J. Mat. Sci: Materials in Medicine* 13 265-269.

Cavalcante, R.S., Imasato, H., Bagnato, V.S., and Perussi, J.R., (**2009**) *Laser Phys. Lett*. **6**, 64.

Chen, B., Pogue, B. W., Hasan, T. (**2005**) Liposomal delivery of photosensitising agents. *Expert Opin. Drug Deliv.*, 2(3): 477-487.

Chen, **K.,** Preuß, A., Hackbarth, St., Wacker, M., Langer, K., Röder, B. (**2009**) Novel photosensitizer-protein nanoparticles for Photodynamic Therapy: Photophysical characterization and *in vitro* investigations. *J. Photochem. Photobiol. B: Biology* 96 66–74.

Cheng, J., Teplya, B., A., Sherifi, I., Sung, J., Luther, G., Gu F. X., Levy-Nissenbaum, E, Radovic-Moreno, A. F., Langer, R., Farokhzad, O. C. (**2007**) Formulation of functionalized PLGA–PEG nanoparticles for in vivo targeted drug delivery. *Biomaterials* 28 869–876.

Choi, SW, Kwon HY, Kim WS, Kim JH. (**2002**) Thermodynamic parameters on poly(d,l-lactide-co-glycolide) particle size in emulsion-diffusion process. *Colloids Surf A: Physicochem Eng Aspect*; 201:283–9.

Copper, M.P. Tan, I.B., Oppelaar, H., Ruevekamp, M.C., Stewart, F.A. (**2003**) Meta-tetra(hydroxyphenyl)chlorin photodynamic therapy in earlystage squamous cell carcinoma of the head and neck, *Arch. Otolaryngol., Head. Neck. Surg.* 129 709– 711.

Csaba, N., Caamano, P., Sanchez, A., Domınguez, F., and Alonso, M. J. (**2005**) PLGA:Poloxamer and PLGA:Poloxamine Blend Nanoparticles: New Carriers for Gene Delivery. *Biomacromolecules*, 6, 271-278.

Cunderlikova, B., Bjørklund, E. G., Pettersen, E. O. and Moan, J. (**2001**) pH-Dependent Spectral Properties of HpIX, TPPS2a, mTHPP and mTHPC. *Photochemistry and Photobiology*, 74(2): 246–252

Davenport, L.; Knutson, J. R.; Brand, L. (**1986**) *Biochemistry*, 25, 1186.

Davila, J. and Harriman, A. (**1990**). Photoreactions of macrocyclic dyes bound to human serum albumin. *Photochem. Photobiol.* 51(1), 1.

Derycke, A. S., De Witte, P. A. (**2004**) Liposomes for photodynamic therapy. *Adv. Drug Deliv. Rev.*, 56: 17-30.

Detty, M. R., Gibson, S. L., and Wagner, S. J. (**2004**) Current Clinical and Preclinical Photosensitizers for Use in Photodynamic Therapy. *J. Med. Chem.*, 47(16): 3897-3915.

Dilkes, M. G.; Benjamin, E.; Ovaisi, S.; Banerjee, A. S. (**2003**) Treatment of primary mucosal head and neck squamous cell carcinoma using photodynamic therapy: results after 25 treated cases. *J. Laryngol. Otol.*, 117: 713-717.

Dougherty, T. J., Gomer, C. J., Henderson, B. W., Jori, G., Kessel, D., Korbelik, M.,Moan, J., and Peng, Q. (**1998**) Photodynamic therapy. *J. Natl. Cancer Inst.*, 90: 889–905.

Dressler, C., Möller U., Lewald T., Berlien H.-P. ,Röder B., Risse H.-J. (**1992**) Introduction of a simple model for testingimmuno conjugates with photosensitizers *Lasers in Med. Science* 7 174.

Duncan, R. (**2005**) Targeting and intracellular delivery of drugs. In Encyclopedia of Molecular Cell Biology and Molecular Medicine, in press. Ed. R A Meyers. Weinheim, Germany: Wiley-VCH Verlag.

Ehrenberg, B., Johnson, F. M. (**1990**) Spectropscopic Studies of

Tetrabenzoporphyrins: Mg TBP, Zn TBP and H TBP. *Spectrochim. Acta.*, 46A: 1521-1532.

Ehrenberg, B. J.L. Anderson and C.S. Foote, (**1998**) Kinetics and yield of singlet oxygen photosensitized by hypericin in organic and biological Media, *Photochem. Photobiol.*, 68, 135-140.

Egorov, S.Y., Kamalov, V.F., Koroteev, N.I., Krasnovsky, A.A., Toleutaev, B.N., Zinukov, S.V. (**1989**) Rise and decay kinetics of singlet oxygen luminescence in water. Measurements with nanosecond time-correlated single photon counting technique. *Chem. Phys. Lett.* 163:421-424.

Ermilov, **E.A.,** Hackbarth, St., Al-Omari, S., Helmreich, M., Jux, N., Hirsch, A., Röder, B. (**2005**) Trap formation and energy transfer in the hexapyropheophorbide a - fullerene C60 hexaadduct molecular system. *Optics Communications* 250 95-104

Foote, C. S.; Denny, R. W. (**1968**) J. *Am. Chem.* SOC.*, 90,* 6233.

Foote, C. S. (**1991**) Definition of type I and type II photosensitized oxidation. *Photochem. Photobiol.*, 54(5): 659.

Gelperina, S., Kisich, K., Iseman, M. D., and Heifets, L. (**2005**) The Potential Advantages of Nanoparticle Drug Delivery Systems in Chemotherapy of Tuberculosis. *Am. J. Respir. Crit. Care Med.*, 172: 1487–1490.

Gorman, A. A., Krasnovsky, A. A. and Rodgers, M. A. J. (**1991**) Singlet oxygen infrared luminescence: unambiguous confirmation of a solvent-dependent radiative rate constant. J. Phys. Chem. 95, 598-601.

Gorman, A. A.; Rodgers, M. A. **(1992)** *J. Photochem. Photobiol.* B, *14*, 159.

Gouterman, M., (**1961**) *J. Mol. Spec.*, *6*, 138.

Gu, H., Xu, K., Yang, Z., Chang, C. K. and Xu, B., (**2005**) Synthesis and cellular uptake of porphyrin decorated iron oxide nanoparticles—a potential candidate for bimodal anticancer therapy, *Chem. Commun.*, 4270–4272.

Gurny R., Peppas, N. A., Harrington, D. D., Banker, G. S. (**1981**) Development of biodegradable and injectable latices for controlled release of potent drugs. *Drug Dev Ind Pharm*; 7:1–25.

Gutowski, M., Carcenac, M., Pourquier, D., Larroque, C., Siant-Aubert, B., Rouanet, P., Pelegrin, A. (**2001**) Intraoperative immunophotodetection for radical resection of cancer: evaluation in an experimental model, Clin. Cancer Res. 7 1142– 1148.

Hackbarth, St., Ermilov, E. A. and Röder, B. (**2005**) Interaction of Pheophorbide a molecules covalently linked to DAB dendrimers. *Opt. Commun.* 248, 295–306.

Hackbarth, St., Schlothauer, J., Preuß, A., Röder, B., (**2009**) New Insights to Primary Photodynamic Effects - Singlet Oxygen Kinetics in Living Cells, *J. Photochem. Photobiol. B: Biology* DOI: 10.1016/j.jphotobiol..11.013.

Hadjur, C., Lange, N., Rebstein, J., Monnier, P., van den Bergh, H., Wagnieres, G.. (**1998**) Spectroscopic studies of photobleaching and photoproduct formation of *meta* (tetrahydroxyphenyl) chlorin (*m*-THPC) used in photodynamic therapy. The production of singlet oxygen by *m*-THPC. *J. Photochem. Photobiol. B: Biology* 45 170-178.

Hagan, W. J.; Barber, D. C.; Whitten, D. G.; Kelly, M.; Albrecht, F.; Gibson, S. L.; Hilf, R.. (**1988**) *Cancer Res.*, *48,* 1148.

Hasan, T., Lin, A.; Yarmush, D.; Oseroff, A.; Yarmush, M. (**1989**) *Journal of Controlled Release, 10,* 107.

Hashimoto, T., Choe, Y. K., Nakano, H., and Hirao, K. (**1999)** Theoretical Study of the Q and B Bands of Free-Base, Magnesium, and Zinc Porphyrins, and Their Derivatives. *J. Phys. Chem. A*, *103,* 1894-1904.

Hatz, S., Lambert, J. D. C., Ogilby, P. R. (**2007**) Measuring the lifetime of singlet oxygen in a single cell: addressing the issue of cell viability. *Photochem. Photobiol. Sci*. 6:1106-1116.

He, H. M.; Carter, D. C. (**1992**) *Nature*, 358, 209–215.

Henderson, B. W., and Dougherty, T. J. (**1992**) How does photodynamic therapy work? *Photochem. Photobiol.,* , 55: 145–157.

Henderson, B. W., Bellnier, D. A., Greco,W. R., Sharma, A., Pandey, R. K., Vaughan, L. A., Weishaupt, K. R., Dougherty, T. J., (**1997)**. An in vivo quantitative structure–activity relationship for a congeneric series of pyropheophorbide derivatives as photosensitizers for photodynamic therapy. *Cancer Res.* 57, 4000–4007.

Hirosue, S., Muller, B.G., Mulligan, R.C., Langer, R. (**2001**) Plasmid DNA encapsulation and release from solvent diffusion nanospheres, J. Control Release 70 231–242.

Hopper, C. A. Kubler, H. Lewis, I.B. Tan, G. Putnam, (**2004**) mTHPC mediated photodynamic therapy for early oral squamous cell carcinoma, *Int. J. Cancer* 111 138–146.

Jeong, Y. I., Shim, Y. H., Song, K. C., Park, Y. G., Ryu, H. W., and Nah, J. W. (**2002**) Testosterone-encapsulated Surfactant-free Nanoparticles of Poly(DL-lactide-*co*-glycolide): Preparation and Release Behavior. *Bull. Korean Chem. Soc.*, Vol. 23, No. 11, 1579-1584.

Jiang, F. N., Jiang, S., Liu, D., Richter, A., Levy, J. G., (**1990**) Development of technology for linking photosensitizers to a model monoclonal antibody, *J. Immunol. Methods* 134 139– 149.

Jichlinski, P., Leisinger, H. J. (**2001**) Photodynamic therapy in superficial bladder cancer: Past, present and future. *Urol. Res.*, 29: 396-405.

Jiménez-Banzo A, Sagristà ML, Mora M, Nonell S (**2008**) Kinetics of singlet oxygen photosensitization in human skin fibroblasts. *Free Radical Bio. Med* 44:1926–1934.

Jori, G., E. Reddi, (**1993**) The role of lipoproteins in the delivery of tumour-targeting photosensitizers, *Int. J. Biochem.* 25 1369–1375.

Jux, N., and Röder, B. (**2009**) Targeting Strategies for Tetrapyrrole-based Photodynamic Therapy of Tumors. Porphyrin handbook.

Kato, H. (**1998**) Photodynamic therapy for lung cancersa review of 19 years' experience. *J. Photochem. Photobiol., B.*, 42: 96-99.

Kautsky, H.; de Bruijn, H., (**1931**) *Naturwissenschaften* 19: 1043.

Keefe, K.A., Tadir, Y., Tromberg, B., et al. (**2002**) Photodynamic therapy of high-grade cervical intraepithelial neoplasia with 5-aminolevulinic acid. *Lasers Surg Med*, 31: 289–93.

Konan, Y. N., Gurny, R., Allemann, E. (**2002a)** State of the art in the delivery of photosensitizers for photodynamic therapy. *J. Photochem. Photobiol. B:Biol.*, 66: 89-106.

Konan, Y. N., Gurny, R. and Allemann, E. (**2002b**) *Int. J. Pharm.*, 233, 239.

Konan, Y. N, Cerny, R., Favet, J., Berton, M., Gurny, R., Allemann, E. (**2003a**) Preparation and characterization of sterile sub-200 nm meso-tetra (4-hydroxylphenyl) porphyrin-loaded nanoparticles for photodynamic therapy. *Eur. J. Pharm. Biopharm.*, 55: 115-124.

Konan, Y. N., Berton, M., Gurny, R. and Allemann, E., (**2003b**) *Eur. J. Pharm. Sci.*, 18, 241.

Krasnovsky A. A. Jr. (**1976**) Photosensitized luminescence of singlet oxygen in solutions. *Bioflzica Russ* 21:748-749

Kreuter, J. (**1983**) Evaluation of nanoparticles as drug-delivery systems III: materials, stability, toxicity, possibilities of targeting, and use, *Pharma. Acta Helv.* 58 242–249.

Kreuter, J, Hekmatara, T., Dreis, S., Vogel, T., Gelperina, S., Langer, K. (**2007**) Covalent attachment of apolipoprotein A-I and apolipoprotein B-100 to albumin nanoparticles enables drug transport into the brain. *Journal of Controlled Release* 118 54–58.

Korinek, M., Dedic, R., Molnar, A., and Hala. J. (**2006**) The Influence of Human Serum Albumin on The Photogeneration of Singlet Oxygen by *meso*-Tetra(4-Sulfonatophenyl)Porphyrin. An Infrared Phosphorescence Study. *Journal of Fluorescence,* Vol. 16, No. 3, May.

Kwon, H. Y., Lee, J. Y., Choi, S. W. Jang, Y. S., Kim, J. H. (**2001**) Preparation of PLGA nanoparticles containing estrogen by emulsification–diffusion method. *Colloids and Surfaces A: Physicochemical and Engineering Aspects* 182 123–130.

Labbe, R. F.; Nishida, G. (**1957**) *Biochim. Biophys. Acta*, *14,* 437.

Labib, A., Lenaerts, V., Chouinard, F., Leroux, J. C., Ouellet, R., Van Lier, J. E. (**1991**) Biodegradable nanospheres containing phthalocyanines and naphthtalocyanines for targeted photodynamic tumor therapy, *Pharm. Res.* 8 1027–1031.

Landry, F. B., Bazile, D. V. Spenlehauer, G., Veillard, M. and Kreuter, J. (**1997**). Release of the fluorescent marker prodan from poly(D,L-lactic acid) nanoparticles coated with albumin or polyvinyl alcohol in model digestive fluids (USP XXII).

Journal of Controlled Release 44, 227–236.

Lang, K., J. Mosinger, D. Wagnerová, M. (**2004**) Photophysical properties of porphyrinoid sensitizers non-covalently bound to host molecules; models for photodynamic therapy. *Coordination Chemistry Reviews* 248 321–350

Langer, K., Coester, C., von Briesen, H., Kreuter, J., (**2000)**. Preparation of avidin-labeled protein nanoparticles as carriers for biotinylated peptide nucleic acid (PNA). *Eur. J. Pharm. Biopharm.* 49, 303–307.

Langer, K., Balthasar, S., Vogel, V., Dinauer, N., von Briesen, H., Schubert, D. (**2003**) Optimization of the preparation process for human serum albumin (HSA) nanoparticles. *International Journal of Pharmaceutics* 257 169–180

Lasic, D. D., (**1997**). Colloid chemistry. Liposomes within liposomes. *Nature* 387, 26–27.

Laustriat G. (**1986**) Molecular mechanism of photosensitization, *Biochimie*, 68: 771-778.

Lee, T.K., Sokoloski, T.D., Royer, G.P. (**1981**) Serum albumin beads: an injectible, biodegradable system for the sustained release of drugs. *Science* 213, 233–235.

Lemoine, D., Francois, C., Kedzierewicz, F., Preat, V., Hoffman, M., Maincent, P. (**1996**) Stability study of nanoparticles of poly(epsiloncaprolactone), poly(d,l-lactide) and poly(d,l-lactide-co-glycolide). *Biomaterials*;17:2191–7.

Lewis, D. H. (1990). Controlled release of bioactive agents from lactide/gylcolide polymers. In Chasin M. and Langer R. eds. Biodegradable Polymers as Drug Delivery Systems. Marcel Dekker, New York, 1–41.

Li, B., Moriyama, E. H., Li, F., Jarvi, M. T., Allen, C. and Wilson, B. C. (**2007**) Diblock Copolymer Micelles Deliver Hydrophobic Protoporphyrin IX for Photodynamic Therapy. *Photochemistry and Photobiology*, 83: 1505–1512.

Lin, C. W. (**1991**). Photodynamic therapy of malignant tumors—recent developments. *Cancer Cells* 3, 437–444.

Lin, W., Coombes, A.G., Davies, M.C., Davis, S.S., Illum, L. (**1993**) Preparation of sub-100 nm human serum albumin nanospheres using a pH-coacervation method. *J. Drug Targeting* 1, 237–243.

Lin, W., Garnett, M. C., Schacht, E., Davis, S. S., Illum, L. (**1999**) Preparation and in vitro characterization of HSA-mPEG nanoparticles. *International Journal of Pharmaceutics* 189 161–170.

Liu, D., Mori, A., Huang, L. (**2002)**. Role of liposome size and RES blockade in controlling biodistribution and tumor uptake of GM1-containing liposomes. *Biochem. Biophys. Acta* 1104, 95–101.

MacAdam, A. B., Shafi, Z. B., James, S. L., Marriott, C., Martin, G. P. (**1997)**. Preparation of hydrophobic and hydrophilic albumin microspheres and determination of surface carboxylic acid and amino residues. *Int. J. Pharm.* 151, 47–55.

Maillard, Ph., Loock, B., Grierson, D.S., Laville, I., Blais, J., Doz, F., Desjardins, L., Carrez, D., Guerquin-Kern, J.-L., Croisy, A. (**2007**) *In vitro* phototoxicity of glycoconjugated porphyrins and chlorins in colorectal adenocarcinoma (HT29) and retinoblastoma (Y79) cell lines. Photodiagnosis and Photodynamic Therapy (2007) 4, 261—268.

Makarov, S.; Litwinski, C.; Ermilov, E. A.; Suvorova, O.; Röder, B.; Wöhrle, D. (**2006**) *Chem. Eur. J.*, *12*, 1468.

Matsumura, Y. and Maeda, H. (**1986)** A new concept for macromolecular therapeutics in cancer chemotherapy; mechanism of tumoritropic accumulation of proteins and the antitumour agent SMANCS. *Cancer Research* 6 6387–6392.

Moesta, K. T., Schlag, P., Douglas, H. O., Jr., Mang, T. S. (**1995**) Evaluating the role of photodynamic therapy in the management of pancreatic cancer. *Lasers Surg. Med.*, 16: 84-92.

Moreno, S. M. J., Monson, E., Reddy, R. G., Rehemtulla, A., Ross, B. D., Philbert, M., Schneider, R. J. and Kopelman, R. (**2003**) Production of singlet oxygen by Ru(dpp(SO3)2)3 incorporated in polyacrylamide PEBBLE, *Sens. Actuators, B*, 90, 82–89.

Mu, L., Feng, S. S. (**2003)** PLGA/TPGS nanoparticles for controlled release of paclitaxel: effects of the emulsifier and drug loading ratio. *Pharm. Res.* 20, 1864–1872.

Nagayasu, A., Uchiyama, K., Kiwada, H. (**1999)** The size of liposomes: a factor which affects their targeting efficiency to tumors and therapeutic activity of liposomal antitumor drugs. *Adv. Drug Deliv. Rev.* 40, 75–87.

Nathan, T. R., Whitelaw, D. E., Chang, S. C., Lees, W. R., Ripley, P. M., Payne, H., Jones, L., Parkinson, M. C., Emberton, M., Gilliam, A. R., Mundy, A. R., Bown, S. G. (**2002**) Photodynamic therapy for prostate cancer recurrence after radiotherapy: a phase I study. *J. Urol.*, 168: 1427-1432.

Niedre, M., M. S. Patterson and B. C. Wilson (**2002**) Direct nearinfrared luminescence detection of singlet oxygen generated by photodynamic therapy in cells in vitro and tissues in vivo. *Photochem. Photobiol.* 75, 382-391.

Niwa, T, Takeuchi, H, Hino, T, Kunou, N, Kawashima, Y. (**1993**) Preparations of biodegradable nanospheres of watersoluble and insoluble drugs with dl-lactide/glycolide copolymer by a novel spontaneous emulsification solvent diffusion method, and the drug release behavior. *J Control Release*; 25: 89–98.

Norris and Taylor, (**1924**) *J. Amer. Chem. SOC.,* 46, 753.

O'Connor, D.V., Phillips, D. (**1984**) Time-correlated single photon counting, Academic Press, London.

Oelckers, S., Sczepan, M., Hanke, T., and Röder, B., (**1997**) *J. Photochem. Photobiol. B*, 39: 219.

Oelckers, S.; Ziegler, T.; Michler, I.; Röder, B. (**1999**) *J. Photochem. Photobiol. B.*, *53*, 121.

Ogilby, P. R. and Foote, C. S. (**1983**) Chemistry of Singlet Oxygen. 42. Effect of Solvent, Solvent Isotopic Substitution, and Temperature on the Lifetime of Singlet Molecular Oxygen ($^1\Delta_g$). *J. Am. Chem. SOC.*, *105,* 3423-3430.

Ono, N.; Bougauchi, M., Maruyama, K. (**1992**) *Tetrahedron Lett.*, *33,* 1629.

Pandey, R. K., Sumlin, A. B., Potter, W. R., Bellnier, D. A., Henderson, B. W., Constantine, S., Aoudia, M., Rodgers, M. R., Dougherty, T. J. (**1996a**) *J. Photochem. Photobiol.*, 63: 194.

Pandey, R. K., Sumlin, A. B., Constantine, S., Aoudia, M., Potter, W. R., Bellnier, D. A., Henderson, B. W., Rodgers, M. A., Smith, K. M., Dougherty, T. J. (**1996b**) Alkyl ether analogs of chlorophyll-a derivatives: Part 1. Synthesis, photophysical properties and photodynamic efficacy. *J. Photochem. Photobiol.* 64, 194–204.

Panyam, J., Labhasetwar, V. (**2003**) Biodegradable nanoparticles for drug and gene delivery to cells and tissue, *Adv. Drug Deliv. Rev.* 55 329–347.

Paul, A., Hackbarth, St., Mölich, A., Luban, C., Oelckers, S., Böhm, F., Röder, B. (**2003**) Comparative Study on the Photosensitization of Jurkat Cells in vitro by Pheophorbide-a and a Pheophorbide-a Diaminobutane poly-propylene-imine Dendrimer Complex. *Laser phys.*, 13: 22-29.

Peer, D., Karp, J. M., Hong, S., Farokhzad, O. C., Margalit, R. and Langer, R. (**2007**) Nanocarriers as an emerging platform for cancer therapy. *Nature Nanotechnology* 2, 751 – 760.

Pelegrin, A., Folli, S., Buchegger, F., Mach, J. P., Wagnieres, G., van den Bergh, H. (**1991**) Antibody-fluorescein conjugates for photoimmunodiagnosis of human colon carcinoma in nude mice, *Cancer* 67 2529– 2537.

Perez, C., Sanchez, A. Putnam, D., Ting, D., Langer, R., Alonso, M. J. (**2001**) Poly(lactic acid)-poly(ethylene glycol) nanoparticles as new carriers for the delivery of plasmid DNA, *J. Control Release* 75 211–224.

Peters, T. (**1985**) *Adv Protein Chem*, 37, 161–242.

Peters, T. (**1996**) All About Albumin. Biochemistry, Genetics and Medical Application; Academic Press: San Diego.

Porter and Windsor, (**1957)** *Nature*, 180, 187.

Poste, G., Kirsh, R. Allison, B. A. (**1983**) Site-specific (targeted) drug delivery in cancer therapy, *Bio/Technology* 1 869–878.

Pramod, K.G., (**1990**) Drug targeting in cancer chemotherapy: a clinical perspective, *J. Pharm. Sci.* 79 949–962.

Prasad, (**2003***)* Introduction to Biophotonics, Wiley p.439

Preuß, A., Chen, K., Hackbarth, St., Wacker, M., Langer, K., Röder, B. Photosensitizer (mTHPC and mTHPP) loaded human serum albumin nanoparticles for Photodynamic Therapy - Part II: “*In vitro*” investigations on Jurkat cells. (in preparation)

Prosst, R. L.; Wolfsen, H. C.; Gahlen, J. (**2003**) Photodynamic therapy for esophageal diseases: a clinical update. *Endoscopy*, 35: 1059-1068.

Puolakkainen, P.; Schroder, T. (**1992**) Photodynamic therapy of gastrointestinal tumors: a review. *Dig. Dis.*, 10: 53-60.

Rancan, F., Helmreich, M., Mölich, A., Jux, N., Hirsch, A., Röder, B., Witt, C. and Böhm, F. (**2005**) Fullerene-pyroPheophorbide a complexes as sensitizer for photodynamic therapy: Uptake and photo-induced cytotoxicity on Jurkat cells. *J. Photochem. Photobiol. B* 80, 1–7.

Regehly, M., Ermilov, E. A., Helmreich, M., Hirsch, A., Jux, N., and Röder, B. (**2007**) Photo-induced Energy and Electron Transfer Processes in HexapyroPheophorbide a-Fullerene [C60] Molecular Systems. *J. Phys. Chem. B 111,* 998-1006.

Renno, R. Z., Miller, J. W. (**2001**) Photosensitizer delivery for photodynamic therapy of choroidal neovascularization. *Adv. Drug Deliv. Rev.*, 52: 63-78.

Röder, B., S. Nicklisch, G. Wischnewsky, E. Slawaticki, H. Meffert: (**1984**) Mittel zur Behandlung von Hauterkrankungen und Tumoren, Patent 08.October, WP 248 282.

Röder, B. (**1986**) Pheophorbide a - a new photosensitizer for PDT. *stud. biophys.* 144 183-186.

Röder, B., D. Näther, T. Lewald, M. Braune, W. Freyer, Ch. Nowak. (**1990**) Photophysical properties and photodynamic activity in vivo of some tetrapyrroles. Biophys.Chem. 35, 303-312 (invited paper).

Röder, B. (**2000a**) Photodynamic therapy, in: Encyclopedia Analytical Chemistry. R. A. Meyers (Ed.), pp. 302-320, John Wiley & sons Ltd., Chichester (invited contribution).

Röder, B. Hanke, T., Oelckers, S., Hackbarth, St. and Symietz, C. (**2000b**) Photophysical properties of Pheophorbide a in solution and in model membrane systems. *J. Porphyrins Phthalocyanines* 4, 37–44.

Röder, B., Hackbarth St., Wöhlecke G. (**2001**) US-Patent, NDN 172-0037-2622-7: Dendrimer-photsensitizer complexes for medical applications. Publication number 00108704 WO vom 08.02.

Rodgers, A.J., Snowden, T. (**1982**) Lifetime of $O_2(^1\Delta_g)$ in Liquid Water As Determined by Time-Resolved Infrared Luminescence Measurements *J. Am. Chem. Soc.* 104:5541-5543.

Roser, M., Kissel, T. (**1993**) Surface-modified biodegradable nano- and microspheres. I. Preparation and characterization. *Eur. J. Pharm. Biopharm.* 39, 8–12.

Rubino, O.P., Kowalsky, R., Swarbrick, J., (**1993**) Albumin microspheres as a drug delivery system: relation among turbidity ratio, degree of cross-linking, and drug release. *Pharm. Res.* 10, 1059–1065.

Salokhiddinov, K. I. Byteva, I. M. and Gurinovich, G. P. (**1981**) Lifetime of singlet oxygen in various solvents. *J. Appl. Spectro.*, 34(5): 892-897.

Schachter D. M, Kohn J. (**2002**) A synthetic polymer matrix for the delayed or pulsatlie release of water-soluble peptides. *J Control Release*;78:143–53.

Schlothauer, J., Hackbarth, St., Röder, B. (**2008**) A new benchmark for time-resolved detection of singlet oxygen luminescence – revealing the evolution of lifetime in living cells with low dose illumination. *Laser Phys. Lett.* 1–6.

Sinha, R., Kim, G. J., Nie, S. M., and Shin, D. M. (**2006**) Nanotechnology in cancer therapeutics: bioconjugated nanoparticles for drug delivery. *Mol Cancer Ther*; 5(8).

Skovsen, E., Snyder, J. W., Lambert, J. D. C., and Ogilby, P. R. (**2005**) Lifetime and Diffusion of Singlet Oxygen in a Cell. *J. Phys. Chem. B, Vol. 109, No. 18,* 8570-8573.

Snyder, J. W., Skovsen, E., Lambert, J. D. C., Poulsen, L., Ogilby, P. R. (**2006**) Optical detection of singlet oxygen from single cells. *PCCP* 8:4280-4293.

Steinhauser, I., Spänkuch, B., Strebhardt, K., Langer, K. (**2006**) Trastuzumab-modified nanoparticles: Optimisation of preparation and uptake in cancer cells. *Biomaterials* 27 4975–4983.

Stella, B., Arpicco, S., Peracchia, M. T., Desmaële, D., Hoebene, J., Renoir, M., d’Angelo, J., Cattel, L., Couvreur, P. (**2000**) Design of folic acidconjugated nanoparticles for drug targeting, *J. Pharm. Sci.,* 89, 1452–1464.

Sternberg, E. D., Dolphin, D. (**1998**) Porphyrin-based Photosensitizers for Use in Photodynamic Therapy. *Tetrahedron* 54 4151—4202**.**

Stevens, P. J., Sekido, M., Lee, R. J. (**2004**) Synthesis and evaluation of a hematoporphyrin derivative in a folate receptor-targeted solid-lipid nanoparticle formulation. *Anticancer Res.*, 24: 161-165.

Tian, Y. Y., Xu, D. D., Tian, X., Cui, F. A., Yuan, H. Q., and Leung, W. N., (**2008**) *Laser Phys. Lett.* 5, 746.

Trekli, M. C., Riss, G., Goralczyk, R., and Tyrrell, R. M. (**2003**) *Free Radical Biol. Med.* 34, 456.

van Dongen, G. A. M. S., Visser, G. W. M., Vrouenraets, M. B. (**2004**) Photosensitizer-antibody conjugates for detection and therapy of cancer. *Advanced Drug Delivery Reviews* 56 31– 52.

Van Nostrum, C. F. (**2004**) Polymeric micelles to deliver photosensitizers for photodynamic therapy. *Adv. Drug Deliv. Rev.*, 56: 9-16.

Verracchia T., Spenlehauer, G., Bazile, D.V., Murry-Brelier, A., Archimbaud, Y. and Veillard, M. (**1995**) Non-stealth poly(lactic acid/albumin) and stealth poly(lactic acid–polyethylene glycol). *Journal of Controlled Release* 36, 1-2, pp. 49-61.

von Burkersroda, F, Schedl, L, Göpferich, A. (**2002**) Why degradable polymers undergo surface erosion or bulk erosion. Biomaterials 23 4221–4231.

Von Tapiener, H., and Jesionek, A. (**1903**) Therapeutische Versuche mit fluoreszierenden Stoffen, *Münchener Medizinische Wochenschrift.*, 50: 2042-2051.

Vrouenraets, M. B., Visser, G. W. M., Loup, C., Meunier, B., Stigter, M., Oppelaar, H., Stewart, F. A., Snow, G. B., van Dongen, G. A. M. S. (**2000**) Targeting of a hydrophilic photosensitizer by use of internalizing monoclonal antibodies: a new possibility for use in photodynamic therapy, *Int. J. Cancer* 88 108– 114.

Wacker, M., Chen, K., Preuss, A., Röder, B., Langer, K. (**2010**) Photosensitizer (mTHPP and mTHPC) loaded albumin nanoparticles: optimization of adsorptive binding and photophysical characterization. *Int. J. Pharm.* (*submitted*)

Wang, J., Wu, J., Zhang, Z. H., Zhang, X. D., Wang, L., Xu, L., Guo, B. D., Li, H., Tong, J. (**2005**) *Chin. Chem. Lett.* 16 1105.

Wang, S. Z., Gao, R. M., Zhou, F. M. and Selke, M. (**2004**) Nanomaterials and singlet oxygen photosensitizers: Potential applications in photodynamic therapy, *J. Mater. Chem.*, 14, 487–493.

Weber, C., Coester, C., Kreuter, J. Langer, K. (**2000a**) Desolvation process and surface characterisation of protein Nanoparticles. *International Journal of Pharmaceutics* 194 91–102.

Weber, C., Kreuter, J., Langer, K., (**2000b**) Preparation of surface modified protein nanoparticles by introduction of sulfhydryl groups. *Int. J. Pharm.* 211, 67–78.

Whitlock, J., H.W., Hanamer, R., Oester, M. Y., Bower, B. K. (**1969**) ,*/. Am. Chem. Soc.*, *91,* 7485.

Wilkinson, F. Helman, W. P. and Ross, A. B. (**1993**) Quantum Yields for the Photosensitized Formation of the Lowest Electronically Excited Singlet State of Molecular Oxygen in Solution. *J. Phys. Chem. Ref. Data.*, 22: 113-262.

Willis, K. J., Szabo, A. G., Drew, J., Zuker, M., Ridgeway, J. M. (**1990**) *Biophys. J.*, 57, 183.

Willstaetter, R. and Stoll, A. (**1913**) Untersuchungen ueber Chlorophyll**,** Springer, Berlin.

Wilson, P. C. (**1989**) Photosensitizing Compounds: Their Chemistry, Biology and Clinical Use; Wiley Interscience: Chichster, 73.

Wüstenberg, E. G., Scheibe, M., Zahnert, T., Hummel, T. (**2006**) Different Swelling Mechanisms in Nasal Septum (Kiesselbach Area) and Inferior Turbinate Responses to Histamine. *ARCH OTOLARYNGOL HEAD NECK SURG.*, 132(3): 277-281.

Yan, F. and Kopelman, R. (**2003**) The embedding of *meta*tetra(hydroxyphenyl)-chlorin into silica nanoparticle platforms for photodynamic therapy and their singlet oxygen production and pH-dependent optical properties, *Photochem. Photobiol.* 78, 587–591.

Zeisser-Labouebe, M., Lange, N., Gurny, R., Delie, F. (**2006**) Hypericin-loaded nanoparticles for the photodynamic treatment of ovarian cancer. *International Journal of Pharmaceutics* 326 174–181.

Acknowledgement

Foremost I would like to express my appreciation to Prof. Dr. Beate Röder. She gives me precious supervision and constructive suggestion within nearly four years. Furthermore she always encourages me and helps me with her tremendous patience. All these I got from her are extremely important in my whole life.

I should also thank Dr. Steffen Hackbarth for his kindly help. We have intense discussion on scientific issue. In any case he brings happiness and hope not only to me but also to other people in our group.

I will never forget to thank Dipl. Biophysik Annegret Preuß, who had shared one office with me for more than three years. Her strong biochemical background offers me a new vision for my work. Not to mention her enthusiastic assistance in terms of my living and language problems.

Mr. Lutz Jager also deserves my thanks since his patience during the chemical preparation for us. Of course I appreciate Mrs. Rosemary Linke for her kindness.

I thank Matthias Wacker and Thomas Knobloch of Institute of Pharmaceutical Technology, Goethe-Universität, (Frankfurt, Germany), who provided me HSA and PLGA nanoparticles, respectively. And of course, I also appreciate Prof. Dr. Langer, Institute of Pharmaceutical Technology and Biopharmacy, Westfälische Wilhelms-Universität Münster, who gave me useful knowledge of biodegradable nanoparticles.

I should also thank BmBF project “NanoCancer” for financial support.

I appreciate Uncle Yao and his family, who offered me a better life in Berlin. My special appreciation dedicates to Weiming Yao, who always gave me warmhearted helping when I need.

Finally, I am grateful to my parents, who gave me my life and contribute their affection to me.

List of Publications

Journal articles:

[1] **Kuan Chen**, Annegret Preuß, Steffen Hackbarth, Matthias Wacker, Klaus Langer, Beate Röder. Novel photosensitizer-protein nanoparticles for Photodynamic Therapy: Photophysical characterization and *in vitro* investigations. J. Photochem. Photobiol. B: Biology 96 (2009) 66–74.

[2] Matthias Wacker, **Kuan Chen**, Annegret Preuss, Beate Roeder, Klaus Langer. Photosensitizer (mTHPP and mTHPC) loaded albumin nanoparticles: optimization of adsorptive binding and photophysical characterization. Int. J. Pharm. (*submitted*)

[3] **Kuan Chen**, Matthias Wacker, Steffen Hackbarth, Carmen Ludwig, Klaus Langer, Beate Röder. Photophysical evaluation of *m*THPC-loaded HSA nanoparticles as novel PDT delivery systems. J. Photochem. Photobiol. B: Biology (*submitted*)

[4] Annegret Preuß, **Kuan Chen**, Steffen Hackbarth, Matthias Wacker, Klaus Langer, Beate Röder. Photosensitizer (mTHPC and mTHPP) loaded human serum albumin nanoparticles for Photodynamic Therapy - Part II: *In vitro* investigations on Jurkat cells. Int. J. Pharm. (*submitted*)

Posters:

[1] **Kuan Chen**, Annegret Preuß, Klaus Langer, Matthias Wacker, Beate Röder. FLIM images of Pheo-Loaded HSA-nanoparticles in Jurkat cells. The 6th International Workshop on "Scanning Probe Microscopy in Life Sciences", October 9 2007, Berlin, Germany

[2] **Kuan Chen**, Annegret Preuß, Thomas Knobloch, Matthias Wacker, Klaus Langer, Beate Röder. Comprehensive investigations on biodegradable photosensitizer-loaded nanoparticles as drug delivery devices Part I: Photophysical research. 7th International Symposium on Photodynamic Therapy and Photodiagnosis in Clinical Practice, October 7-11, 2008, Bressanone, Italy

[3] Annegret Preuß, **Kuan Chen**, Thomas Knobloch, Matthias Wacker, Klaus Langer,

Beate Röder. Comprehensive investigations on biodegradable photosensitizer-nanoparticle delivery systems Part II: *In vitro* studies of photosensitizer-loaded nanoparticles in Jurkat cells. 7th International Symposium on Photodynamic Therapy and Photodiagnosis in Clinical Practice, October 7-11, 2008, Bressanone, Italy

Contributions on conferences:

[1] **Kuan Chen**, Annegret Preuß, Beate Röder. Photophysical and *in vitro* studies on photosensitizer-protein nanoparticles (Part I). BMBF-Project Annual Meeting, “Development of cell type specific drug carrier systems for cancer therapy (NanoCancer)” June. 29.2007, St. Ingbert, Germany

[2] **Kuan Chen**, Annegret Preuß, Beate Röder. Investigations on Photosensitizer-HSA nanoparticles using in PDT. BMBF-Project Annual Meeting, “Development of cell type specific drug carrier systems for cancer therapy (NanoCancer)” November. 09.2007, Berlin, Germany

[3] **Kuan Chen**, Annegret Preuß, Beate Röder. Photophysical characterization to photosensitizer-nanoparticle carrier system. BMBF-Project Annual Meeting, “Development of cell type specific drug carrier systems for cancer therapy (NanoCancer)” April 25. 2008, Frankfurt, Germany

[4] **Kuan Chen**, Annegret Preuß, Beate Röder. Photophysical characterization to photosensitizer-nanoparticle carrier system. BMBF-Project Annual Meeting, “Development of cell type specific drug carrier systems for cancer therapy (NanoCancer)” January 20. 2009, Hamburg, Germany

[5] **Kuan Chen**, Annegret Preuß, Beate Röder. Photophysical characterization of photosensitizer-nanoparticle carrier systems. BMBF-Project Annual Meeting, “Development of cell type specific drug carrier systems for cancer therapy (NanoCancer)” October 16. 2009, Saarbrücken, Germany

[6] Beate Röder, Martin Regehly, **Kuan Chen**, Annegret Preuss, Anno Wiehe, Thomas Knobloch, Matthias Wacker, Klaus Langer. Nanoparticles as carriers for PDT agents. 7th International Symposium on Photodynamic Therapy and Photodiagnosis in Clinical Practice, October 10, 2008, Bressanone, Italy

[7] Beate Röder, Martin Regehly, Annegret Preuss, **Kuan Chen**, Thomas Knobloch, Matthias Wacker, Klaus Langer. International Photodynamic Association World Congress 2009, SPIE. Biodegradable nanoparticles as carriers for PDT agents. Paper 7380-151. June 15. 2009, Seattle, USA

Selbständigkeitserklärung

Ich versichere, meine Dissertation selbständig erarbeitet und verfasst zu haben und alle gemäß § 6 Absatz (3) verwendeten Hilfen und Hilfsmittel angegeben zu haben.

Beijing 14.03.10

Kuan Chen